Rendezvous and Formation Flying Related to the TECSAS Mission

by

Mathieu Alfred Landry

Department of Mechanical Engineering
McGill University, Montréal

October 2005

A thesis submitted to McGill University in partial fulfilment of the requirements of the degree of Master of Engineering

Your file Votre référence
ISBN: 978-0-494-22652-0
Our file Notre référence
ISBN: 978-0-494-22652-0

"Why do we do research?
Because, as human beings, we are inherently curious, we want to understand. We are uncomfortable with mystery.
Space, if I may say, is the perfect stage for human curiosity and ingenuity."

- Marc Garneau[1]
President, Canadian Space Agency
Carleton Celebrates 25 Years of
NSERC-Funded Research
Ottawa, Ontario
26 February 2004.

[1] Carleton University : Carleton University Website, www.carleton.ca (current June 2005).

ACKNOWLEDGEMENTS

First and foremost, I would like to thank my research supervisor Professor Arun K. Misra for his advice and guidance. Without his help, this thesis would not have been possible.

I would also like to give thanks to my research co-supervisor at the Canadian Space Agency, Dr. Alfred Ng. His support was essential to the completion of this work. Furthermore, many thanks to Frederic Pelletier of the Jet Propulsion Laboratory, and to Johanne Heald of the Canadian Space Agency for their help and their ideas during the progression of this work.

To my fiancée Chantal Cormier, thank you for your understanding, your patience and your love. Finally, to my family, Reginald, Pauline and Nathalie Landry, for always believing in me in all my endeavour, many thanks.

I acknowledge the funding of this project to the National Science and Engineering Research Council of Canada, the Canadian Space Agency and McGill University.

ABSTRACT

In this thesis, spacecraft rendezvous and spacecraft formation flying were examined in context of the TECSAS mission. Three terminal rendezvous trajectories, one V-bar approach and two R-bar approaches, are compared in terms of ΔV fuel usage and time of flight (TOF). Results showed that the lidar-based V-bar approach trajectory with a 90 m straight-line approach distance is the optimal scenario for the given TECSAS mission guidelines. Four formation flying scenarios are examined: two projected circular formations and two in-track formations. The effects of the J_2 and atmospheric drag perturbations on these formations are studied for several time spans. Results showed that the projected circular formations are disrupted by the J_2 perturbations after a short time span, and that atmospheric drag perturbations caused significant in-track and radial drifts for formations where the two spacecraft are not identical. Finally, control force requirements are much higher for both formations when the two spacecraft are not identical.

RÉSUMÉ

Ce mémoire présente une analyse de rendez-vous et de vol en formation d'engins spatiaux appliquée à la mission TECSAS. Trois trajectoires terminales de rendez-vous (une approche suivant l'axe de vitesse orbitale et deux approches suivant l'axe radial) ont été étudiées en terme de quantité de carburant et de temps de vol nécessaires. De plus, quatre scénarios de vol en formation ont été analysés dont deux de type "projected circular" et deux de type "in-track". Les effets associés aux perturbations venant de la non-sphéricité de la Terre (effet J_2 terrestre) et de la force de traînée atmosphérique ont été examinés pour chacune des formations et pour différents temps de vols. Les résultats démontrent qu'après une courte durée d'une journée, l'effet du J_2 terrestre détériore les formations de type "projected circular" tandis que la force de traînée atmosphérique cause des dérives importantes dans le cas des formations de deux engins spatiaux non identiques.

NOMENCLATURE

A	spacecraft's cross-sectional area
$\mathbf{A}$	state space matrix
$\mathbf{a}_{Drag}$	atmospheric drag acceleration acting on target spacecraft
$\mathbf{a}_{J2}$	J_2 acceleration acting on target or chief spacecraft
$\mathbf{B}$	control matrix
$\mathbf{C}$	vector in equation (4.51)
C_D	spacecraft's drag coefficient
C_E	distance of the surface of the Earth from its centre at a given geodetic latitude defined by equation (B.5)
c	constant defined by equation (4.7)
d	formation diameter for projected circular formation
$\mathbf{e}$	state error
e_E	eccentricity of the Earth
f	target spacecraft's true anomaly
$\mathbf{f}_{chaser}$	atmospheric drag acceleration acting on chaser spacecraft (rendezvous formulation)
$\mathbf{f}_{Drag}$	atmospheric drag acceleration (formation flying formulation)
$\mathbf{f}_{target}$	atmospheric drag acceleration acting on target spacecraft (rendezvous formulation)
H	scale height used in equation (2.21)
h	reference altitude used in equation (2.21)
h_{ellp}	altitude above ellipsoid
i	inclination of the orbit of the target or chief spacecraft
i_{sat}	inclination of the orbit of the spacecraft (formation flying formulation)
i_0	reference orbit initial inclination
J	cost function for control system
J_2	second spherical harmonic of the Earth's gravitational potential
$\mathbf{K}$	control gain matrix

k	constant defined by equation (4.8)
l	constant defined by equation (4.13)
m	spacecraft's mass
n	mean motion constant defined by equation (4.5)
$\mathbf{Q}$	control matrix defined by equation (4.60)
q	constant defined by equation (4.12)
$\mathbf{R}$	control matrix defined by equation (4.61)
$\mathbf{R}_t$	rotation matrix defined by equation (B.9)
R_E	radius of the Earth
$\mathbf{r}_c$	position vector of the chaser spacecraft from the centre of the Earth expressed in the Hill frame (rendezvous formulation)
$\mathbf{r}_{ref}$	position vector of the reference orbit in the ECI reference frame (formation flying formulation)
$\mathbf{r}_{rel}$	position vector of a spacecraft in the Hill reference frame
$\mathbf{r}_t$	position vector of the target spacecraft from the centre of the Earth expressed in the Hill frame (rendezvous formulation)
$\mathbf{r}_{target}$	position vector of the target spacecraft in the ECI reference frame (rendezvous formulation)
r_0	reference orbit's radial distance from the centre of the Earth
$\mathbf{r}_{\delta sat}$	equatorial projection of the spacecraft's position vector
s	constant defined by equation (4.6)
t	time
$\mathbf{u}$	control force acceleration vector
$\mathbf{v}_{chaser}$	chaser spacecraft's velocity
$\mathbf{v}_{spacecraft\ rel}$	spacecraft's velocity relative to the Earth's atmosphere in the Hill reference frame
$\mathbf{v}_{target}$	target spacecraft's velocity
$\mathbf{v}_{target\ ECI}$	target spacecraft's velocity relative to the Earth's atmosphere in the ECI reference frame
w	control weight
$\Delta\mathbf{d}_{Drag}$	differential atmospheric drag acceleration estimates

$\Delta\mathbf{f}_{J2}$	differential J_2 acceleration acting on chaser spacecraft
$\Delta\mathbf{f}_{Drag}$	differential atmospheric drag acceleration acting on chaser spacecraft
ΔV	impulse thrust magnitude
$\Delta\Omega_0$	difference in longitudes of ascending nodes of the deputy and chaser spacecraft
α	initial spacecraft phase angle
γ	continuous force per unit mass (rendezvous formulation)
γ	constant defined by equation (formation flying formulation)
μ	Earth's gravitational parameter
ρ	atmospheric density
ρ_0	reference atmospheric density
θ	target spacecraft's argument of latitude
Φ_0	constant defined by equation (4.16) (formation flying formulation)
Ω	target's right ascension of ascending node
ϕ_{gd}	geodetic latitude
$\dot{\Omega}_{ref}$	constant defined by equation (4.11)
$\dot{\Omega}_{sat}$	constant defined by equation (4.10)
ω	target spacecraft's argument of perigee
ω_E	Earth's angular velocity

Note: A dot indicates differentiation with respect to time

TABLE OF CONTENTS

LIST OF FIGURES

LIST OF TABLES

CHAPTER 1 - INTRODUCTION

Spacecraft rendezvous and satellite formation flying are the two subjects treated in this thesis. The study concerning spacecraft rendezvous is done in partnership with the Canadian Space Agency (CSA) with regards to the TECSAS mission, which is a technology demonstration mission in collaboration with the German Aerospace Center (DLR). The section of the thesis pertaining to satellite formation flying is also done in partnership with CSA, however not with regards to the TECSAS mission, but instead with their interest in Earth observation missions.

1.1 PAST AND FUTURE MISSIONS

From a historical standpoint, spacecraft rendezvous and formation flying have been necessary for many past missions ranging from the Gemini and Apollo programs to the current International Space Station (ISS) program. The first manned spacecraft rendezvous missions were Gemini 6 and 7, which demonstrated close rendezvous techniques along with station keeping techniques. The following mission, Gemini 8 showed that a "contact" rendezvous between two spacecraft could be done when astronaut Neil Armstrong, who would later become the first man to walk on the Moon, guided Gemini 8 to a hard docking with an Agena target vehicle. From then on, manned spacecraft rendezvous were utilized as part of the Apollo program both in Earth and lunar orbits, the later in order to bring the crew back to the Earth. These missions have allowed us to accumulate significant rendezvous experience, albeit only under human control. Even today, human controllers oversee many current ISS rendezvous activities.

Having said this, autonomous spacecraft rendezvous opens many possibilities especially in the area of on-orbit servicing (OOS) missions, and is a crucial part of any Mars Sample Return (MSR) mission. Japan's ETS-7 mission in 1998-1999 was the first successful autonomous spacecraft rendezvous and formation flying mission. Over the past years, many on-orbit servicing missions have been discussed; however, many problems associated with OOS have yet to be solved, for example: autonomous docking/de-docking, autonomous berthing/de-berthing, autonomous capture/release, flying around re-fuelling, ORU operations, and capture of non-cooperative satellites.

Some of the problems associated with on-orbit servicing will be addressed in upcoming missions such as NASA's DART (Demonstration of Autonomous Rendezvous Technology) mission and DLR-CSA's TECSAS (TEChnology SAtellite for demonstration and verification of Space systems) mission. The DART mission (see Figure 1.1) was NASA's first autonomous rendezvous mission and was launched in April 2005.

Figure 1.1: DART Rendezvous [NASA DART Homepage].

DART successfully demonstrated key technologies in the areas of autonomous rendezvous for future use in the development of NASA's Space Plane, which will be designed to bring and rescue astronauts to and from the ISS. The entire mission was predicted to last 24 hours during which the spacecraft was first placed in a circular polar orbit and then would perform several autonomous rendezvous and proximity operations, collision avoidance manoeuvres and finally, would fly away from the target satellite. However, the mission was ended early due to an on orbit anomaly, which resulted in fuel consumption problems. Details related to the other mission, TECSAS, are given in section 1.2.

Satellite formation flying has also been the object of growing interest during the past few years. Many applications, ranging from astronomical space-based interferometry like the planned DARWIN mission (see Figure 1.2) to multiple spacecraft for improved resolution for Earth sensing missions, are envisioned in the following decades. In this thesis, spacecraft formations related to Earth observations will be studied within the current guidelines of the TECSAS mission and of current CSA interest.

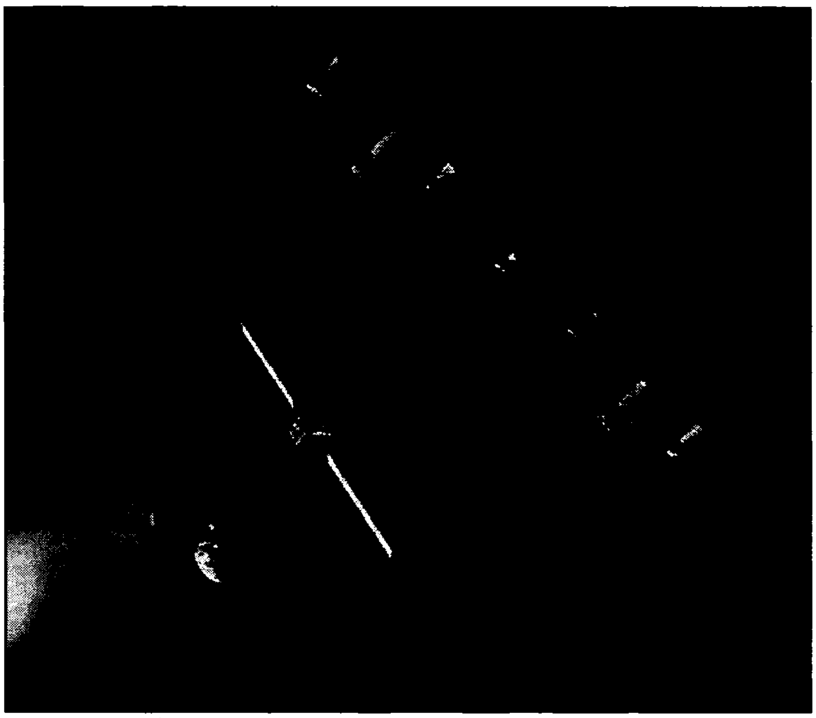

Figure 1.2: DARWIN mission [ESA Science & Tech.: DARWIN Website].

1.2 TECSAS MISSION

As stated earlier, the TECSAS mission is a technology demonstration mission, which will validate hardware and software solutions in order to accomplish on-orbit satellite servicing. Scheduled for launch in 2009, it is a joint endeavour between CSA Space Technologies and the German Space Center (DLR) in partnership with the Russian Babakin Space Center.

The mission will consist of two small spacecraft, each with an approximate mass of 175 kg or less. Figure 1.3 shows the servicer (or chaser) spacecraft, which is being provided by the Babakin Space Center. The chaser spacecraft is fitted with a robotic arm that has a three-fingered end-effector based on the Canadian built SARAH (Self-Adaptive Robotic Auxiliary Hand) hand. The serviced (or target) spacecraft will be provided by CSA under its microsatellite program.

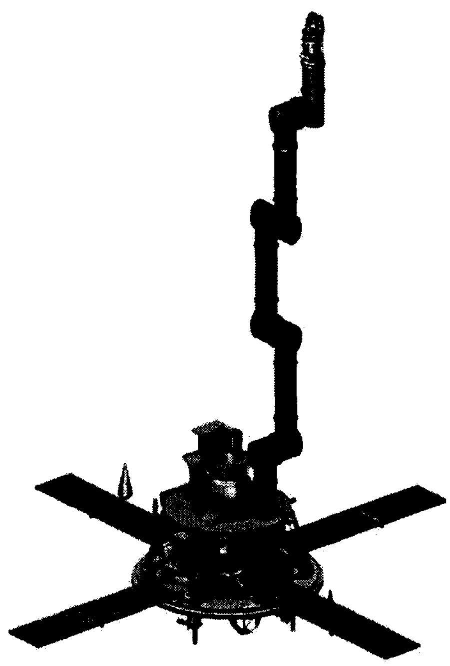

Figure 1.3: TECSAS chaser spacecraft [On-Orbit Servicing Website].

During the mission, a series of orbital rendezvous and docking tests will be performed in which the chaser spacecraft using the robotic arm will grasp the target spacecraft while in close proximity (see Figure 1.4). The two spacecraft will also remain in a formation flight mode for certain period maintaining a short distance between the two. The TECSAS mission will thus demonstrate the capability of rescuing a scientific micro-satellite whose control system has failed, thereby prolonging its operational life. The main objectives of the mission are to demonstrate orbit and altitude control of a composite spacecraft for servicing operations and to undertake on-orbit servicing from different ground control varying from telepresence to autonomous operations.

Compared to other OOS missions, the TECSAS mission has unique features and challenges such as the rendezvous and capture of two spacecraft separately launched two years apart, and a target satellite that will be tumbling during the capture phase. Finally, unlike other robotic capture missions flown so far, the servicer satellite will use a three-fingered robotic end-effector based on the SARAH hand. This last challenge, if successful, opens up possibilities of servicing any general spacecraft without the need of a special docking port. In the case of the TECSAS mission, a standard handle will serve as grapple fixture on the target spacecraft.

Figure 1.4: TECSAS rendezvous [On-Orbit Servicing Website].

The TECSAS orbit will be used within this thesis and its characteristics are given in Table 1.1. In addition, unless otherwise stated, both spacecraft will be assumed to be identical and to have the characteristics found in Table 1.2.

Table 1.1: TECSAS Orbit Characteristics

Parameter	Mission orbit
Semi-major axis	6876.8 km
Eccentricity	0.00368
Inclination	78.1°
Argument of the perigee	112.9°
Longitude of the ascending node	320.0°

Table 1.2. TECSAS Spacecraft Characteristics

Parameter	TECSAS servicer and target spacecraft
Mass	175 kg
Cross-sectional area	2.22 m^2
Drag coefficient	2.3

1.3 SPACECRAFT RELATIVE MOTION DYNAMICS

In this section, a literature review of the dynamics associated with relative motion of spacecraft is presented. Generally, there are two main methods used for describing relative motion of spacecraft. The first method uses Cartesian-form relative motion equations of motion, and are typically known as the Clohessy-Wiltshire (C-W) equations or the Hill's equations. The second method uses differences between the orbital elements of the chaser (or deputy) and target (or chief) spacecraft in order to model the relative motion. In addition, there exist other analytical methods that are used to describe relative motion between spacecraft derived from dynamical principles. In the subsequent sections existing literature for each of these methods is briefly described.

1.3.1 C-W Equations-Based Dynamics

The equations of motion used for the majority of rendezvous analysis come from Clohessy and Wiltshire (1960) and are therefore known as the C-W equations. These equations, which describe the relative motion of one spacecraft with respect to another, are mainly used for short-term rendezvous because they do not take into account any perturbations like J_2 and atmospheric drag. Also, the C-W equations in their original form were developed for the case when the target orbit is circular, so they are of limited use for this study.

A similar set of equations was derived by Hill (1878) to study lunar motion. He gave the analytical solutions to the C-W equations, and in their original form, they were developed to describe orbital perturbations with respect to a reference orbit. Hill's equations, as they are known, are often used to design formations for spacecraft formation flying because of their simplicity. However, while these equations are valid for a short-time span, they are not very useful in correctly describing relative motion between spacecraft for formation flying because the errors due to the neglected orbital perturbations grow over time. Finally, we note that some of the characteristics of the motion are lost because of the neglected perturbation terms in the Hill's equations.

For high precision rendezvous studies in a rotating local vertical local horizontal (LVLH), or Hill, reference frame attached to the target spacecraft, Kechichian (1998a) derived a set of second order non-linear differential equations of motion. These equations take into account the J_2 perturbations from the Earth's oblateness by using an unaveraged form for the J_2 acceleration acting on the spacecraft. Also, atmospheric drag perturbations are included in the equations of motion, which are valid for any elliptic orbit. In a second paper, Kechichian (1998b) presented the algorithm necessary to solve a two-impulse fixed-time noncoplanar rendezvous for any elliptic orbit. The author used an iterative scheme in order to determine the correct magnitude and orientation of the initiating impulse.

A brief literature review and classification regarding linearized rendezvous was done by Carter (1998). In this paper, the author also developed a general state transition matrix that can be used for any arbitrary Keplerian orbit and is valid for any central force field. The author derived this solution by modifying the Tschauner-Hempel equations, which were originally developed for spacecraft rendezvous in an elliptic orbit.

Sedwick et al. (1999) quantified the perturbations due to J_2, atmospheric drag, solar radiation pressure, and magnetic field interactions, first through dimensional analysis for the bulk motion of a cluster, and second, with regards to spacecraft relative motion. The study was done in context with the TechSat21 formation flying mission, which requires a projected circular type formation (Sabol, et al., 2001). Results show that for passive formation flying, a control thrust of 0.5 cm/sec/orbit is needed to counteract perturbations on the bulk motion, and that over the 7 years life span; active formation flying requires substantial ΔV fuel consumption in the order of 250 m/s per spacecraft.

Various relative motion orbits between two satellites were studied using Hill's equations by Vadali et al. (2000). By using mean orbital elements (Chobotov, 2002), the effects of the J_2 perturbations were included in the study; however, atmospheric drag perturbations were neglected. Also, the authors developed a modified set of Hill's equations that include the J_2 perturbations. These modified equations are propagated along with a reference orbit that uses a mean drift rate for the right ascension of ascending nodes (Ω) to account for the J_2 perturbations.

Melton (2000) developed a new time dependant state transition matrix for relative motion in an elliptical reference orbit, which is valid for eccentricities of 0 to 0.3. The state transition matrix is expanded for powers of eccentricity and is accurate to second order of eccentricity. The author also notes that the solution is valid for non-coplanar elliptical orbits.

Sabol et al. (2001) used Hill's equations to study several spacecraft formation designs: in-plane, in-track, circular, and projected circular formations. The mathematical developments and physical descriptions for all four cases were given. Assuming realistic perturbations, the formations were propagated using the Draper Semianalytic Satellite Theory (DSST). The test cases consisted of an 800 km altitude circular polar orbit, and the spacing between spacecraft was set at 1 km. The authors showed through simulations how each formation is affected differently by orbital perturbations, which included: full geopotential model, atmospheric drag, lunar and solar third-body point-mass, and solar radiation pressure. Results for the in-plane formation showed that the formation is stable even in the presence of orbital perturbations, thus this type of formation does not require any formation keeping manoeuvres except in the cases where short-cycle repeat ground-track orbits are used. For those cases, the authors showed that low cost manoeuvres need to be applied infrequently in the along-track direction. Compared to the in-plane, the in-track formation is less stable and requires small along-track manoeuvres in order to compensate for the atmospheric drag perturbations. The authors found that as the separation distance between spacecraft increases, the differential drag perturbations get larger, and as a result of this, the formation keeping manoeuvres are more costly in terms of ΔV, or fuel consumption. Finally, for the cases of circular formations and the projected circular formations, the J_2 perturbations cause these formations to be unstable over time. Differential precession of the orbital planes, which is a function of the inclination differences in the spacecraft formation, and rotation of the orbital line of apside, which affects all spacecraft equally, are the two perturbative effects due to J_2 perturbations. The authors noted that for these formations, daily corrective manoeuvres are to be made for station keeping purposes and that the other perturbations, like atmospheric drag, are negligible compared to the J_2 perturbations.

A set of linearized constant-coefficient differential equations of motion that include the perturbations of the J_2 gravity potential were derived by Schweighart and Sedwick (2002). These equations are used to accurately describe the relative motion between spacecraft and are very similar to the Hill's equations. The authors validated the newly developed equations of motion using an orbit propagator, which included the J_2 perturbations. Simulations showed that these new equations have a maximum modeling error of 0.4% for all cases of orbits and cluster configurations. Using these new equations of motion, spacecraft formations can be designed to minimize the differential nodal effects that produce separation between satellites in the cross-track direction. The authors also noted an effect they called tumbling where the satellite cluster appears to tumble around the z-axis of the reference orbit. This is caused by the difference between the cross-track and in-plane periods, which are coupled, and has a longer period than either of them. Finally, this tumbling effect needs to be addressed by mission designers if the mission demands strict requirements for the groundtrack projection of the formation.

Following the work of Carter (1998), Yamanaka and Andersen (2002) derived a state transition matrix that is simpler and is valid for any elliptical orbits ($0 \leq e < 1$). The only inputs needed in order to determine the relative positions and velocities of the chaser spacecraft are its initial relative position and velocity and the true anomaly of the target spacecraft. Finally, the authors showed that the results are in good agreement with numerical results.

Following the work of Melton (2000), Vaddi et al. (2003) showed how to correct the initial conditions for bounded relative motion involving an elliptical reference orbit. This was done by combining the solutions of the elliptical non-linear and elliptical linearized systems, and relating these to the period matching requirements for bounded relative motion. Finally, the authors corrected the bias term in the in-track direction by adjusting the initial condition for the radial velocity.

Recently, a multiple-impulse manoeuvre algorithm for transfer between any two relative motion states derived from C-W equations was presented by Lovell and Tragesser (2004). In this formulation, relative orbital element differences are used to initialize the solution.

1.3.2 Relative Orbital Element Differences

The second method of representing the dynamics associated relative motion between two spacecraft is to use differences between the orbital elements of the deputy with respect to the chief spacecraft. This method is also known as the geometric method. Brief descriptions of research papers concerning this method are presented in this section.

Alfriend et al. (2000) developed an algorithm using a state transition matrix that includes the reference orbit eccentricity and the gravitational J_2 perturbations, in order to determine the relative positions between two spacecraft. The state transition matrix was determined using a method, which the authors call the geometric method, where the relationships between the relative states and differential orbital elements are used instead of solving the relative motion differential equations. Also, a curvilinear coordinate system is used instead of the local vertical local horizontal (LVLH) Cartesian-based reference frame. Finally, the authors noted that the resulting errors in estimating the relative motion are much less than those when using Hill's equations.

Furthermore, Schaub and Alfriend (2001) presented analytical methods using mean orbital element differences in order to establish J_2 invariant relative orbits, which means that two neighbouring orbits are chosen as so as they drift at equal angular rates on the average. This is done by assuring that the secular drift of the longitude of ascending node and the sum of the argument of perigee and mean anomaly are set equal between two neighbouring orbits.

Schaub (2002) presented a method to estimate the linearized relative orbit motion through relative orbit element differences valid for circular and elliptical reference orbits. However, in this formulation, true anomaly is used as the independent variable instead of time. Following this work, Schaub (2003) extended the orbit element differences description of his earlier work to include secular drift due to J_2 and atmospheric drag perturbations. The resulting solutions are analytical in the case of J_2 perturbations, but are not when atmospheric drag perturbations are taken to account.

In addition, Gim and Alfriend (2003) developed closed form state transition matrices in order to determine relative motion that includes eccentricity and J_2 perturbations. These state transition matrices, derived by using the geometric method, were both determined for osculating and mean orbital elements. Finally, the authors compared their methods with numerical solutions obtained by integrating each spacecraft's equation of motion in the Earth-centered-inertial reference frame (ECI) with a gravity field incorporating gravitational terms. They showed that the estimation errors are small and are most likely from the neglected up to J_5 higher-order gravitational terms.

Another solution using relative orbital element differences was presented by Broucke (2003). The resulting solution is explicit in time instead of on the reference spacecraft's true anomaly. Broucke's method consisted of taking the partial derivatives with respect to the orbital elements of the two-body solution in polar coordinates. After removing the singularities associated with zero eccentricity, a 4x4 solution matrix is obtained which can be reduced to the Clossehy-Wiltshire solution matrix when the eccentricity is set to zero.

Recently, Meyssignac, and Fourcade (2005) derived a relative motion model from relative geometry. The model uses the orbital elements of the reference satellite and orbital element differences between the chaser and the reference satellite. The resulting equations, valid for any chief eccentricity, can be developed in any reference frame and can be used with osculating orbital elements in order to model orbital perturbations.

1.3.3 Other Work

In this section, other work pertaining to dynamics of spacecraft relative motion is presented.

A procedure for locating orbits such that the relative positions of spacecraft within a triangular formation remain constant with very little dispersion over many years, even without applying any formation keeping control thrust was developed by Koon et al. (2001). The method uses Routh reduction and Poincaré section techniques appropriate for the J_2 dynamics.

Furthermore, Wiesel (2002) developed a new relative motion solution, which includes all zonal harmonics of the Earth's gravitational field. The method is based on nearly circular reference periodic orbits and Floquet theory for the relative motion. Comparisons with numerical orbit propagators and the Clohessy-Wiltshire equations show that this new solution is at least three orders of magnitude more accurate than the later.

Balaji and Tatnall (2003) derived equations of relative motion for spacecraft formation flying by a series of transformations and translations from the Earth-centered inertial frame to the spacecraft-centered rotating LHLV frame. These equations hold for elliptic orbits of the chief and orbital perturbations can be included by use of Gauss' equations.

The use of Hamiltonian dynamics to model relative motion between spacecraft was recently demonstrated by Guidbout and Scheeres (2004). Spacecraft formations were derived from the two-point boundary value problem using this method. Also, fuel optimal formation reconfiguration manoeuvres were investigated.

A scenario for a two-satellite along-track interferometry synthetic aperture radar (SAR) mission in the L and K-bands was studied by Gill and Runge (2004). The formation baseline was determined from interferometric principles in order to satisfy sensor constraints. Also, differential drag perturbations for this type of mission and a fuel budget for control requirements were presented.

Finally, Sabatini et al. (2005) proposed using generic algorithms (GA) in order to find initial conditions for close relative orbits.

1.4 SPACECRAFT RENDEZVOUS ANALYSIS

The majority of current information concerning spacecraft rendezvous analysis is found in research articles related to the design of upcoming or planned missions. In an addition, Fehse (2003) has recently published a book that examines most aspects associated with this topic. In this section, some brief information concerning Fehse's book is presented followed by a literature review of mission design research papers.

1.4.1 Review of Automated Rendezvous and Docking of Spacecraft

All of the major elements of spacecraft rendezvous are addressed in Fehse (2003). These include: rendezvous mission phases, orbital dynamics and trajectory elements, safety and collision avoidance, approach strategies, guidance, navigation and control systems as well as sensors, mating systems, and finally space and ground systems. In the areas of rendezvous trajectories, three approach strategies are given: an approach to a docking port on the –V-bar, an approach to a berthing box on the R-bar, and finally, an approach to a docking port on the +V-bar. In these examples, sensor accuracy and safety elements are examined, but no fuel budgets are given.

1.4.2 Mission Design Research Papers

Since spacecraft rendezvous is a vital component to any Mars Sample Return (MSR) mission, several research articles related to the rendezvous and mission design aspects of MSR have been recently published. Lee et al. (1999) provided an overview of the preliminary mission design aspect of a NASA-planned MSR mission. In the baseline scenarios for this MSR mission, the rendezvous strategy is subdivided into three phases: (i) preliminary rendezvous where the chaser spacecraft locates the target spacecraft (in this case, the Mars sample canister), (ii) intermediate rendezvous where the chaser spacecraft matches the target's orbit and uses natural drift to approach the target spacecraft, and (iii) terminal rendezvous where the chaser spacecraft captures the target spacecraft using an autonomous onboard system. In addition, the authors give brief descriptions for each rendezvous phase as well as their corresponding time scales.

Focus on the intermediate phase of rendezvous for this NASA-planned MSR mission was presented by D'Amario et al. (1999). In their paper, the authors explained how nodal phasing orbits would be used in order to reduce fuel consumption when matching the chaser's orbit to the target's orbit. Also, the authors noted that in order to establish a 99% probability of capture level of both sample canisters, a series of 8 to 10 rendezvous manoeuvres would be required in the intermediate phase for a total ΔV fuel budget of 478m/s.

Finally, the terminal rendezvous phase for this NASA-planned MSR mission was analyzed by Kachmar et al. (1999) in which two rendezvous approaches were compared. The first approach considered consisted of a V-bar rendezvous approach along with some station keeping at selected points. The second approach considered is a co-elliptic rendezvous approach with a final transfer 80 m ahead of the sample canister. The chaser would then approach the target along the V-bar in order to capture it using LIDAR sensor measurements. Because the second approach requires less ΔV and provides natural abort capability, the authors concluded that it represents a more desirable strategy than the first approach strategy. In the end, the total ΔV fuel budget for the terminal phase using the second approach strategy is estimated to be approximately 5.7 m/s.

Additional rendezvous analysis pertaining to future planned missions are also found in literature. Settelmeyer et al. (1998) described a mission scenario in order to service a geostationary satellite. For this mission, the initial aiming-point of the rendezvous approach is set at approximately 24 km behind the target and a couple of kilometres below the V-bar. A series of 3 orbital transfers and drift orbits, followed by 3 single closing manoeuvres are used to bring the servicer spacecraft to an inspection point at 100 m behind the target spacecraft on the V-bar. From then on, the servicer would perform in-plane and out-of-plane fly-around inspections of the target. The authors then described how a robotic manipulator could be used for spacecraft capture in such a mission.

Results of the terminal rendezvous phase from the ETS-7 mission were analysed by Mokuno et al. (1999). For this mission, the desired rendezvous trajectory consisted of an injection at a hold point at –1100 m on the V-bar followed by a C-W control manoeuvre to a hold point at 150 m behind the target. However, because of manoeuvre inaccuracy, the C-W manoeuvre ended at around 200 m such that a second manoeuvre was used to bring the chaser to the desired –150 m V-bar hold point. A final V-bar approach completed the trajectory. Accuracy of various sensors is also given by the authors, however, details regarding the fuel budget or rendezvous time scale were not given.

Further details regarding rendezvous sensor performances along with preliminary details on ESA's Automated Transfer Vehicle (ATV) are given by Cislaghi et al. (1999). The ATV is designed to perform autonomous rendezvous with the International Space Station (ISS) for re-boost / re-fuelling and payload supply / removal missions. The authors examined both long-range and short-range rendezvous using Relative-GPS techniques for the long-range segment, and a laser Rendez-Vous Sensor (RVS) for the short-range segment. Details relating to the ATV's navigation and control systems are also presented.

A terminal rendezvous mission profile for the H-II Transfer Vehicle (HTV) is presented by D'Souza et al. (1999). In the terminal approach phase, the chaser is scheduled to first perform a Hohmann transfer in order to position itself at approximately -5 km on the target V-bar. This is followed by two tangential manoeuvres and a hold point at -17 km on the V-bar. Finally, a transfer to a lower orbit, followed by a R-bar approach manoeuvre finishes the approach profile.

Another terminal rendezvous trajectory is shown in Roe and Howard (2003) with regards to the upcoming NASA DART mission. The rendezvous approach considered consist of a controlled drift, followed by a transfer to +3 km on V-bar, then 2 radial hopping manoeuvres up to +300m on the V-bar, which are then followed by a straight-line approach up to +10 m. The authors also note on proximity operations and on the GN&C software that will be demonstrated by this mission.

Recently, Pelletier et al. (2004) evaluated two terminal rendezvous trajectories related to the European Space Agency's (ESA) proposed Mars Sample Return (MSR) mission: first, the co-circular approach as described by Kachmar et al. (1999) and second, a new V-bar hopping approach. The new V-bar hopping approach starts with a Hohmann transfer, followed by a series of V-bar hopping manoeuvres in order to keep the chaser within a given field of view (FOV) (20° centered on V-bar) in order for the LIDAR instrument to track it. The rendezvous approach ends with a straight-line V-bar approach from approximately 500 m behind the target on the V-bar. However, no mention of ΔV fuel budgets and time of flight (TOF) were given for both of these trajectories. Finally, the authors commented on the development of a MATLAB/SIMULINK based autonomous rendezvous simulator that incorporates guidance, navigation and control functions.

A mission scenario for the upcoming DLR-led TECSAS mission is presented by Dupuis et al. (2004). Long-range rendezvous, short-range rendezvous, station keeping, and capture phases of the mission are described briefly. However, no rendezvous trajectory is presented along with any specific details on fuel consumption and TOF.

Finally, in Endemaño et al. (2005), a rendezvous trajectory is shown which is similar to Pelletier et al (2004). However, only one radial impulse hopping manoeuvre is used, which is followed by a straight-line V-bar approach from approximately 1 km behind the target spacecraft. The authors note that ESA is considering this type of trajectory for a planned MSR mission.

1.5 FORMATION FLYING CONTROL SCHEMES

Environmental perturbations will generally cause spacecraft formations to disperse over time. Therefore, in order for spacecraft formation flying missions to succeed, control systems are needed to maintain inter-spacecraft positions at their desired values. In this section, a literature review of various methods useful for controlling spacecraft formations are presented.

1.5.1 Linear Quadratic Regulator Feedback Control of Hill Coordinates

One type of feedback control scheme that numerous researchers have used is the linear quadratic regulator, commonly called the LQR controller. Ulybyshev (1998) developed an LQR controller for feedback control of satellites placed in an in-plane formation in order to counteract geopotential and atmospheric drag perturbations. The goal was to minimize the in-track relative displacements between spacecraft and the orbital period displacements relative to the reference orbit. Stability and robustness of the control law were also presented.

Additionally, Sparks (2000) presented a linear feedback control scheme using a optimal linear quadratic regulator (LQR) in order to minimize the fuel cost. The controller applied both radial and in-track impulses to counteract the J_2 perturbations on spacecraft placed in a projected circular formation. In addition, expressions were derived from Gauss's equations in order to estimate the amount of ΔV required to overcome drift in the argument of perigee.

Several linear quadratic regulators (LQR) were explored and compared by Starin et al. (2001) while simulating formation reconfiguration manoeuvres for spacecraft in the projected circular formation. LQR designs were not optimized, but rather based on likely mission performance measures. Manoeuvre simulations were carried out with and without radial thrusts and results show that manoeuvres without radial thrusts are generally more fuel-efficient than the former.

Furthermore, Caramagno et al. (2003) investigated several controllers including a single input single output (SISO) proportional derivative (PD) controller and several LQR controllers for navigation during the two phases of a typical Mars Sample Return (MSR) rendezvous trajectory: a close station keeping point and a circumnavigation fly-by with low thrust manoeuvre. Basic C-W equations were used for relative state propagation. Results show that only one of the five LQR controllers should be retained for further study along with the SISO PD controller.

Finally, three different control schemes for satellite formation flying were analysed by Vaddi and Vadali (2003). These control schemes included various LQR controllers, a Lyapunov stabilized controller, and a period matching controller. The control schemes were used in order to minimize errors between the non-linear and linear dynamic models, and they were tested on two projected circular formations of 10 km and 100 km radius, respectively with a chief semi-major axis of 7100 km. Results show that the Lyapunov controller consumed the largest amount of fuel, while the period matching controller consumed the least. However, the authors noted that the Lyapunov controller offers global stability, which results in an exact projected circular formation. On the other hand, the LQR controller offers no zero steady state error. Having said this, one has to keep in mind that the steady state errors were very small and the fuel consumption was much smaller than in the case of the Lyapunov method. Finally, the period matching controller required the minimum amount of fuel and gave zero steady state error; however, in order for it to work properly, the initial conditions need to be close, within 5%, to the ideal unperturbed case.

1.5.2 Relative Orbit Elements Feedback Control

Another method used for formation flying control is to feedback relative orbit elements between the target and chaser spacecraft. Vadali et al. (1999) developed a mean element optimal control based on Gauss's equations, relative orbital elements, and on constraints for bounded relative motion.

Schaub et al. (2000) presented two non-linear feedback control laws in order to control a spacecraft formation using a J_2-invariant reference orbit. The first control law feeds back errors in terms of mean orbit elements, while the second feeds back Cartesian-based position and velocity tracking errors. The two approaches were compared numerically. Following that work, Schaub and Alfriend (2002) developed a hybrid continuous feedback control law in terms of both the local Cartesian-based relative orbit coordinates, or Hill coordinates, and the desired orbital element differences. A direct linear mapping between the Hill coordinates and the corresponding orbital element differences was used for the construction of the control law. The accuracy of the control law was investigated with respect to the use of the full non-linear mapping.

1.5.3 Other Control Methods

Spacecraft formation flying control can also be accomplished by other methods such as optimization algorithms. Tillerson and How (2001) presented fuel and time optimal algorithms for formation station keeping in the presence of J_2, atmospheric drag, and solar radiation pressure perturbations. Fuel consumption (ΔV) was estimated to be in the range of 5 to 15 mm/s per orbit for reference orbit eccentricities of 0 to 0.5.

Mishne (2002) developed a method to compensate for the secular combined effects of first-order gravitational perturbations (J_2) and atmospheric drag perturbations using an optimality condition in order to minimize fuel consumption. Moreover, with this method, the correction of planar parameters (semi-major axis, eccentricity) and out-of-plane parameters (inclination) are executed at different times.

An impulse control scheme that uses only tangential and out-of-plane thrusters is presented by Alfriend et al. (2003). The scheme incorporates first order eccentricity terms and results show that the errors are approximately $1/8^{th}$ of those when eccentricity is neglected. The control scheme uses Gauss' variation equations (non-singular orbital elements) in order to compute the necessary impulses.

Lovell et al. (2003) used a parametric model derived from the modified C-W equations developed by Schweighart and Sedwick (2002), and presented an impulsive burn algorithm designed for transfers between any two relative states. The burn sequence begins at either perigee or apogee and the waiting time between burns is user specified as an integral number of half-periods of the chief satellite. However, the algorithm is only valid for in-plane motion. Given certain assumptions, the algorithm can be used to determine minimum fuel reconfigurations. The algorithm is useful for on-board flight software because of its degree of autonomy and robustness.

Duan and Bainum (2003) showed how to eliminate or control relative drift (the longitude of ascending node, the argument of perigee, and mean anomaly) caused primarily due to J_2 perturbations by use of an algorithm that uses mean orbital elements. Following their previous work, Duan and Bainum (2004) investigated control methods that can adapt to different thrust levels without compromising the system performance and mission tasks. An optimal control law was presented for the out-of-plane motion, while a linear control law was presented for the in-plane motion.

In addition to the various control schemes employed so far, Fourcade (2005) showed that differential drag due to differential solar panel attitude can be used for station keeping when considering the CNES interferometric wheel formation. Also, an autonomous orbit controller was developed. He found that final control accuracies are within a few meters for a 1 km wheel array.

Finally, Garcìa, and Masdemont (2005) used finite element method to reconfigure spacecraft formations in an optimal fashion. Results were obtained for the Terrestrial Planet Finder (TPF) formation.

More information concerning formation flying guidance and control can be found in Hadaegh et al. (2002), and in Scharf et al. (2002). In the first article, the authors present a comprehensive overview of key technology needs in the area of formation guidance and control for currently under development and future formation flying missions, while in the second article, a survey regarding spacecraft formation flying guidance is presented.

1.6 OBJECTIVE OF THE THESIS

The purpose of this thesis is to develop and validate analytical and numerical tools for different rendezvous and formation flying scenarios for the TECSAS mission, as well as a pair of SIMULINK simulator models for use by the Canadian Space Agency to study future satellite servicing and satellite formation flying missions.

Unlike the majority of past rendezvous analyses, this study takes into account both differential J_2 and differential atmospheric drag perturbations. These perturbations are also included in the formation flying analysis. Adding these perturbations to the C-W models, which are often used in rendezvous and formation flying analyses, improves their accuracy in order to better reflect realistic relative motion behaviour between spacecraft.

1.7 ORGANIZATION OF THE THESIS

Spacecraft rendezvous related to the TECSAS mission will be discussed in chapters 2 and 3. The equations of motion used for spacecraft rendezvous are developed in chapter 2. This is followed by the analysis of three different rendezvous trajectories in terms of fuel consumption, time of flight (TOF), and in terms of the TECSAS mission guidelines, presented in chapter 3.

Formation flying analysis is carried out in chapters 4 and 5. First, the equations of motion used for formation flying, as well as the inclusion of a linear feedback controller in order to maintain the formation, are presented in chapter 4. Then chapter 5 contains analysis of various formation flying scenarios.

Finally, in the last chapter of this thesis, concluding remarks as well as recommendations for future work are presented.

In conclusion, as shown in this chapter, spacecraft formation flying and spacecraft rendezvous are areas of great scientific interest because of their usefulness in both space exploration, and in general scientific endeavours. Analytical developments related to spacecraft rendezvous shall be the topic of the following chapter.

CHAPTER 2 - SPACECRAFT RENDEZVOUS

Spacecraft rendezvous is the topic of this chapter. More precisely, the equations of motion used for spacecraft rendezvous analysis are presented. The chapter begins with the formulation of relative motion between two spacecraft, which is then followed by two subsections devoted to the equations of motion describing relative motion and reference orbit propagation. Finally, several rendezvous manoeuvres are discussed in the last section of this chapter. Most of the information is this chapter is readily available through the literature. However, modifications were made to suit the particular needs of the TECSAS mission. The goal of this chapter is to present the equations that were used to build a MATLAB/SIMULINK simulator suitable for spacecraft rendezvous analyses.

2.1 COORDINATE FRAMES

In order to have a successful rendezvous attempt, the chaser spacecraft must dock with the target spacecraft at a docking port or at a berthing box located on the latter spacecraft. In this section, the equations of motion used to describe relative motion between two spacecraft and reference orbit propagation are presented.

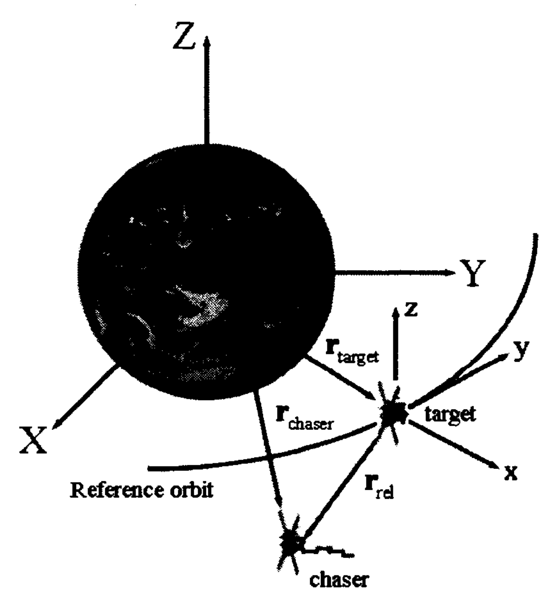

Figure 2.1: Coordinate Systems for Relative Motion Analysis.

Figure 2.1 depicts the geometry of the target and chaser spacecraft. It may be noted that two reference frames are used in this formulation. The first reference frame used is the Earth-Centered Inertial (ECI) reference frame designated by the *XYZ* axes. The origin of the ECI reference frame is the centre of the Earth and the Earth's equator defines the fundamental plane. In addition, the *X*-axis points towards the vernal equinox, the *Y*-axis is 90° to the east in the equatorial plane, and finally, the *Z*-axis extends through the North Pole. The position of the target spacecraft in the ECI reference frame is defined by

$$\mathbf{r}_{target} = \begin{bmatrix} X & Y & Z \end{bmatrix}^T \tag{2.1}$$

The second reference frame used in the problem formulation is the relative motion reference frame, otherwise known as the Hill frame, and is designated in Figure 2.1 by the letters *xyz*. The origin of the Hill frame coincides with the target spacecraft's centre of mass, and thus moves on the reference orbit as the target spacecraft orbits around the Earth. As a result of this, the Hill frame rotates at the same rate as the target's orbital rate, $\dot{\theta}$, and its origin is located relative to the centre of the Earth by the target's non-circular radial distance given by r_{target}.

Furthermore, the Hill frame is described as follows: the *x*-axis points in the radial direction; the *z*-axis is perpendicular to the reference orbit plane, and is called the cross-track direction; finally, the *y*-axis completes the right-handed orthogonal set, and is called appropriately the in-track direction. The position of the chaser in the relative reference frame, which is of interest for rendezvous analyses, is thus given by

$$\mathbf{r}_{rel} = \begin{bmatrix} x & y & z \end{bmatrix}^T \tag{2.2}$$

where x, y, z are called Hill coordinates.

2.1.1 Relative Motion Equations

As mentioned in the literature review, the majority of rendezvous analyses use the Clohessy-Wiltshire (C-W) equations in order to describe the motion of the chaser with respect to the target spacecraft. However, these equations are valid for circular orbits only; because of the small eccentricity of the TECSAS's orbit, the equations of motion used for this study will be the linearized C-W equations of motion for an elliptical reference orbit as given by Schaub and Junkins (2003). These equations are given below:

$$\ddot{x} - x\left(\dot{\theta}^2 + 2\frac{\mu}{r_{target}^3}\right) - y\ddot{\theta} - 2\dot{y}\dot{\theta} = \Delta f_{J2x} + \Delta f_{Drag\,x} \tag{2.3}$$

$$\ddot{y} + x\ddot{\theta} + 2\dot{x}\dot{\theta} - y\left(\dot{\theta}^2 - \frac{\mu}{r_{target}^3}\right) = \Delta f_{J2y} + \Delta f_{Drag\,y} \tag{2.4}$$

$$\ddot{z} + \frac{\mu}{r_{target}^3} z = \Delta f_{J2z} + \Delta f_{Drag\,z} \tag{2.5}$$

In these equations, x y z are the chaser's position in the Hill frame. In addition, μ represents the gravitational parameter (universal gravitational constant multiplied by the mass of the Earth), and θ is the target's argument of latitude angle, which is defined by the sum of the target's argument of perigee, ω, and its true anomaly, f. Furthermore, Δf_{J2x}, Δf_{J2y}, Δf_{J2z} and $\Delta f_{Drag\,x}$, $\Delta f_{Drag\,y}$, and $\Delta f_{Drag\,z}$ are the differential J_2 and differential atmospheric drag perturbations, respectively, acting on the chaser with respect to the target spacecraft. In this study, these differential orbital perturbations are added to the linearized C-W equations in order to accurately describe relative motion between the two spacecraft.

The added differential J_2 perturbations, expressed in Hill frame coordinates, are modeled as the gradient of the J_2 gravity potential and are taken from Schweighart and Sedwick (2002) as given by the following equations:

$$\Delta f_{J2x} = \frac{6\mu J_2 R_E^2}{r_{target}^5}\left\{\left(1-3\sin^2 i\sin^2\theta\right)x+\left(\sin^2 i\sin 2\theta\right)y+\left(\sin 2i\sin\theta\right)z\right\} \quad (2.6)$$

$$\Delta f_{J2y} = \frac{6\mu J_2 R_E^2}{r_{target}^5}\left\{\begin{matrix}\left(\sin^2 i\sin 2\theta\right)x \\ +\left[-1/4-\sin^2 i\left(1/2-(7/4)\sin^2\theta\right)\right]y+\left(-\sin 2i\cos\theta/4\right)z\end{matrix}\right\} \quad (2.7)$$

$$\Delta f_{J2z} = \frac{6\mu J_2 R_E^2}{r_{target}^5}\left\{\begin{matrix}\left(\sin 2i\sin\theta\right)x \\ +\left(-\sin 2i\cos\theta/4\right)y+\left[-3/4+\sin^2 i\left(1/2+(5/4)\sin^2\theta\right)\right]z\end{matrix}\right\} \quad (2.8)$$

where J_2 is the gravitational perturbation term, R_E is the Earth's radius, and i is the target orbit's inclination.

For this study, differential atmospheric drag perturbations are obtained from the atmospheric drag acting on each spacecraft individually:

$$\Delta\mathbf{f}_{Drag} = \mathbf{f}_{chaser} - \mathbf{f}_{target} \quad (2.9)$$

where $\mathbf{f}_{chaser}$ and $\mathbf{f}_{target}$ are the atmospheric drag perturbations acting on the chaser and on the target, respectively. Moreover, each individual component is determined by the atmospheric drag equation given in Vallado (2003):

$$\mathbf{f}_{Drag} = -\frac{1}{2}\frac{C_D A}{m}\rho v_{spacecraft_{rel}}\mathbf{v}_{spacecraft_{rel}} \quad (2.10)$$

In equation (2.10), C_D is the corresponding spacecraft's drag coefficient, A is its cross-sectional area, m is its mass, ρ is the atmospheric density at the given altitude and $\mathbf{v}_{spacecraft_{rel}}$ is the spacecraft's velocity relative to the Earth's atmosphere expressed in the relative motion reference frame. Since the attitude of the spacecraft is controlled, C_D and A are considered constant with respect to the oncoming flow.

The following equation is used in order to determine the velocity of the target spacecraft with respect to the rotating atmosphere:

$$\mathbf{v}_{target_{rel}} = \mathbf{v}_{target} - \boldsymbol{\omega}_E \times \mathbf{r}_t \tag{2.11}$$

where $\mathbf{v}_{target}$ is the target's velocity expressed in the Hill frame as

$$\mathbf{v}_{target} = \begin{bmatrix} \dot{r}_{target} & r_{target}\dot{\theta} & 0 \end{bmatrix}^T \tag{2.12}$$

$\mathbf{r}_t$ is the target's position vector from the centre of the Earth expressed in the Hill frame as

$$\mathbf{r}_t = \begin{bmatrix} r_{target} & 0 & 0 \end{bmatrix}^T \tag{2.13}$$

and the Earth's angular velocity vector, $\boldsymbol{\omega}_E$, is given by

$$\boldsymbol{\omega}_E = \begin{bmatrix} \omega_E \sin i & 0 & \omega_E \cos i \end{bmatrix}^T \tag{2.14}$$

where ω_E is the Earth's angular velocity.

The velocity of the target with respect to the rotating atmosphere expressed in the Hill frame is thus given by

$$\mathbf{v}_{target_{rel}} = \begin{bmatrix} \dot{r}_{target} & r_{target}\dot{\theta} - r_{target}\omega_E \cos i & 0 \end{bmatrix}^T \tag{2.15}$$

The velocity of the chaser spacecraft with respect to the rotating atmosphere is determined from the following equation:

$$\mathbf{v}_{chaser_{rel}} = \mathbf{v}_{chaser} - \boldsymbol{\omega}_E \times \mathbf{r}_c \tag{2.16}$$

where $\mathbf{r}_c$ is the chaser's position from the centre of the Earth expressed in the Hill frame as follows

$$\mathbf{r}_c = \begin{bmatrix} r_{target} + x & y & z \end{bmatrix}^T \tag{2.17}$$

The chaser's velocity, $\mathbf{v}_{chaser}$, expressed in the Hill frame is given by

$$\mathbf{v}_{chaser} = \mathbf{v}_{target} + \dot{\mathbf{r}}_{rel} + \dot{\boldsymbol{\theta}} \times \mathbf{r}_{rel} \tag{2.18}$$

where $\mathbf{r}_{rel}$ is the position of the chaser in Hill frame coordinates and $\dot{\boldsymbol{\theta}}$ is the target's orbital rate vector given by

$$\dot{\boldsymbol{\theta}} = \begin{bmatrix} 0 & 0 & \dot{\theta} \end{bmatrix}^T \tag{2.19}$$

After developing the cross products and substituting all the corresponding terms in equation (2.16), the velocity of the chaser spacecraft with respect to the rotating atmosphere is given by

$$\mathbf{v}_{chaser_{rel}} = \begin{bmatrix} \dot{x} - y\dot{\theta} + \dot{r}_{target} + y\omega_E \cos i \\ \dot{y} + x\dot{\theta} + r_{target}\dot{\theta} - \left(r_{target} + x\right)\omega_E \cos i + z\omega_E \sin i \\ \dot{z} + y\omega_E \sin i \end{bmatrix} \tag{2.20}$$

The atmospheric density, ρ, is evaluated from an exponential model as described in Vallado (2002), where the density varies exponentially according to the following equation:

$$\rho = \rho_0 \exp\left[-\frac{h_{ellp} - h_0}{H}\right] \tag{2.21}$$

The exponential model uses a reference density, ρ_0, a reference altitude, h_0, a scaled height, H, and the actual altitude above the ellipsoid (Earth's surface), h_{ellp}. Table A-1 in Appendix A gives the necessary values for these variables with respect to the altitude of the spacecraft above the ellipsoid. The spacecraft's altitude above the ellipsoid is computed with the use of the algorithm shown in Appendix B.

2.1.2 Reference Orbit Propagation

For this study, a perturbed elliptical reference orbit, which includes J_2 and atmospheric drag perturbations, was chosen instead of an unperturbed circular reference orbit in order to increase modeling accuracy. The reference orbit propagation is done in the Earth-Centered Inertial (ECI) Cartesian coordinates reference frame. The position and velocity of the target spacecraft are then transformed to give the necessary data used in the C-W equations (equations (2.3)-(2.5)).

The motion of the target spacecraft with respect to the ECI reference frame is described by the two-body equation of motion given below:

$$\ddot{\mathbf{r}}_{target} = -\frac{\mu}{r_{target}}\mathbf{r}_{target} + \mathbf{a}_{J2} + \mathbf{a}_{Drag} \tag{2.22}$$

where $\mathbf{a}_{J2}$ and $\mathbf{a}_{Drag}$ are the J_2 and atmospheric drag perturbations, respectively.

The J_2 perturbations acting on the target spacecraft in terms of ECI Cartesian coordinates are given by the following (Vallado (2002)):

$$a_{J2_I} = -\frac{3J_2\mu R_E^2 X}{2r_{target}^5}\left(1 - \frac{5Z^2}{r_{target}^2}\right) \tag{2.23}$$

$$a_{J2_J} = -\frac{3J_2\mu R_E^2 Y}{2r_{target}^5}\left(1 - \frac{5Z^2}{r_{target}^2}\right) \tag{2.24}$$

$$a_{J2_K} = -\frac{3J_2\mu R_E^2 Z}{2r_{target}^5}\left(3 - \frac{5Z^2}{r_{target}^2}\right) \tag{2.25}$$

while the atmospheric drag perturbations are given by

$$\mathbf{a}_{Drag} = -\frac{1}{2}\frac{C_{D\,target}\,A_{target}}{m_{target}}\rho\, v_{target}\mathbf{v}_{target} \tag{2.26}$$

where $C_{D\ target}$ is the target spacecraft's drag coefficient, A_{target} is the target's cross-sectional area, m_{target} is the spacecraft's mass, ρ is the atmospheric density at the spacecraft's altitude and $\mathbf{v}_{target_{ECI}}$ is the target's velocity relative to the Earth's atmosphere expressed in the ECI reference frame. The atmospheric density is computed in similar fashion as described in the section 2.1.1.

Finally, the velocity of the target satellite with respect to the rotating atmosphere is

$$\mathbf{v}_{target_{ECI}} = \begin{bmatrix} \dot{X} + \omega_E Y & \dot{Y} - \omega_E X & \dot{Z} \end{bmatrix}^T \tag{2.27}$$

Now, in order to use the equations developed in section 2.1.1, some orbital parameters and orbital elements from the target's reference orbit are needed. The necessary orbital elements are calculated using the procedure given in Chobotov (2002). The additional orbital parameters needed are as follows: the target's orbit radius, r_{target}, the target's radial rate, $\dot{r}_{target}$, the target's argument of latitude rate of change, or orbital rate, $\dot{\theta}$, and the target's argument of latitude angular acceleration, $\ddot{\theta}$. Each of these orbital parameters is determined from the target's Cartesian ECI Coordinates.

The radial distance is determined from

$$r_{target} = \sqrt{X^2 + Y^2 + Z^2} \tag{2.28}$$

By taking the time derivative of equation (2.28), the target's range rate is obtained as

$$\dot{r}_{target} = \frac{1}{r_{target}}\left(X\dot{X} + Y\dot{Y} + Z\dot{Z}\right) \tag{2.29}$$

Furthermore, the target's velocity is defined as

$$v_{target} = \sqrt{\dot{X}^2 + \dot{Y}^2 + \dot{Z}^2} = \sqrt{\dot{r}_{target}^2 + r_{target}^2\dot{\theta}^2} \tag{2.30}$$

from which, the argument of latitude rate of change can be determined to be

$$\dot{\theta} = \left[\frac{1}{r_{target}^2}\left(v_{target}^2 - \dot{r}_{target}^2\right)\right]^{\frac{1}{2}} \tag{2.31}$$

The target's argument of latitude angular acceleration is found by differentiating squares of the two sides in equation (2.31) with respect to time, which gives

$$\ddot{\theta} = \frac{1}{\dot{\theta}}\left\{-\frac{\dot{r}_{target}}{r_{target}^3}\left(v_{target}^2 - \dot{r}_{target}^2\right) + \frac{1}{r_{target}^2}\left(\dot{X}\ddot{X} + \dot{Y}\ddot{Y} + \dot{Z}\ddot{Z} - \dot{r}_{target}\ddot{r}_{target}\right)\right\} \tag{2.32}$$

where $\ddot{r}_{target}$ is found by taking the second time derivative of equation (2.28), thus giving

$$\ddot{r}_{target} = \frac{1}{r_{target}}\left(v_{target}^2 + X\ddot{X} + Y\ddot{Y} + Z\ddot{Z} - \dot{r}_{target}^2\right) \tag{2.33}$$

The necessary orbital parameters for use with the relative motion equations (2.3)-(2.5) of section 2.1.1 are given by equations (2.28) to (2.33).

The next section focuses on the equations describing the various rendezvous manoeuvres used in this study.

2.2 RENDEZVOUS MANOEUVRES

In this section, impulse rendezvous manoeuvres are discussed. For each manoeuvre, the required ΔV fuel consumption and duration will be indicated. Because manoeuvre descriptions are only applicable within the validity of the C-W equations, in this study, the manoeuvres were assumed to be valid and were applied as described in this section. However, orbital perturbations caused the resulting manoeuvre trajectories to differ slightly from their original desired paths, such that a perturbation-type approach was taken for trajectory design. This means that subsequent manoeuvres were calculated from the resulting end states of the previous manoeuvre instead of using a pre-defined trajectory layout. In addition, for most manoeuvres, final impulses were computed in order to stop relative motion instead of relying on analytical relations.

The rendezvous manoeuvres presented in this section are: the Hohmann transfer, the tangential impulse fly-around manoeuvre, the radial impulse manoeuvre, the straight-line V-bar approach manoeuvre, and the straight-line R-bar approach manoeuvre. The advantages and disadvantages for each of these manoeuvres will become clear in chapter 3.

2.2.1 Rendezvous Reference Frame

Before introducing the various rendezvous manoeuvres used in this study, it is necessary to specify a new notation for the Hill reference frame. For most rendezvous analysis, the Hill frame is commonly known under the name Local Vertical/Local Horizontal (LVLH) frame. Under the LVLH notation, the x-axis is known as the R-bar direction, the y-axis is known as the V-bar direction, and finally, the z-axis is known as the H-bar direction. This nomenclature is used in this section when describing the rendezvous manoeuvres.

2.2.2 Hohmann Transfer

Many rendezvous trajectories use a Hohmann transfer as the first trajectory element because it is used in order to transfer a spacecraft from one orbit to another one of different altitude. The major advantage of this manoeuvre is that it uses minimal fuel compared to other approaches. Figure 2.2 shows the manoeuvre sequence. In order to execute the Hohmann transfer, an initial impulse, ΔV_{y1}, is applied when the spacecraft is at the perigee of the parking orbit. This impulse places the spacecraft in a transfer orbit, which has the same perigee as the parking orbit and the same apogee as the desired final orbit. When the spacecraft reaches the apogee of the transfer orbit, half an orbital period later, a second impulse, ΔV_{y2}, of same size and same direction as the initial impulse is fired, placing the spacecraft in the desired final orbit. This only holds true within the validity of the C-W equations; for large differences in altitude, both impulses will not be of same size.

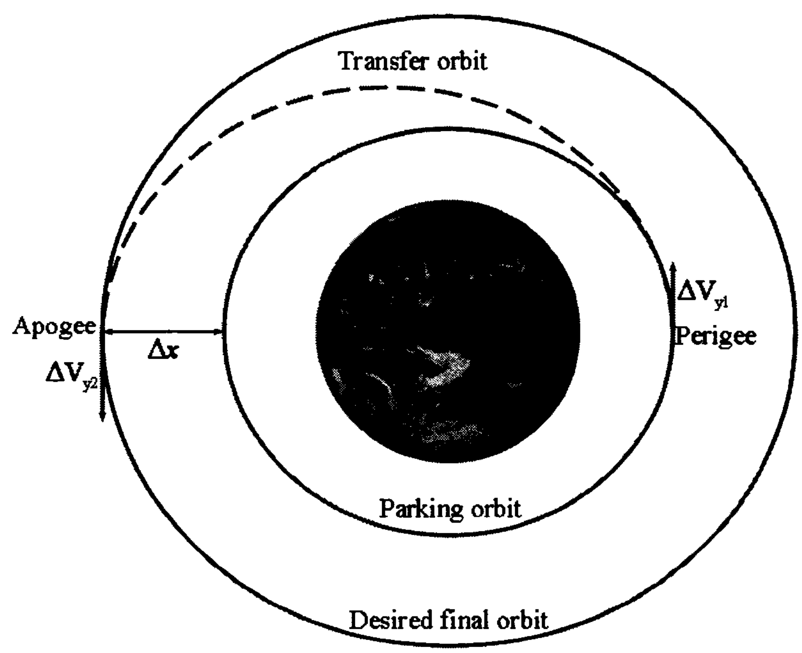

Figure 2.2: Hohmann Transfer Manoeuvre.

The following figure shows the Hohmann transfer manoeuvre sequence in the Hill reference frame. In the Hill frame, the desired final circular orbit is represented by the y-axis, and the altitude difference between the parking orbit and the desired final orbit is given by Δx.

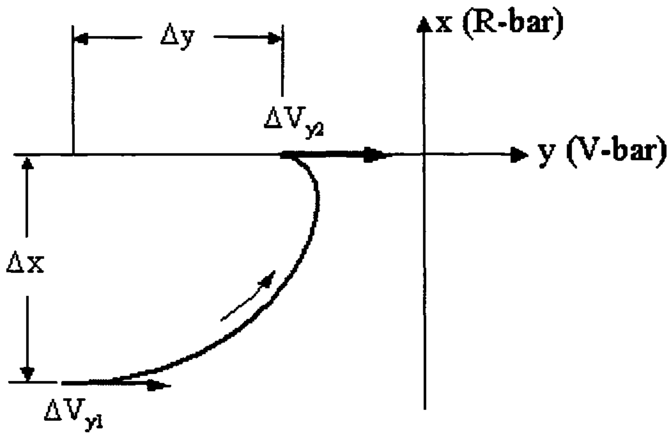

Figure 2.3: Hohmann Transfer Manoeuvre in Hill Reference Frame [Fehse (2003)].

The magnitude of the initial impulse and thus the final impulse is related to the desired altitude difference, Δx, between the parking orbit and the desired final orbit by the following equations, as given by Fehse (2003):

$$\Delta y = \frac{3\pi}{4}\Delta x \tag{2.34}$$

$$\Delta V_{y1} = \Delta V_{y2} = \frac{\dot{\theta}}{4}\Delta x \tag{2.35}$$

Thus, the total ΔV fuel requirement for the Hohmann transfer manoeuvre is

$$\Delta V_{total} = \frac{\dot{\theta}}{2}\Delta x \tag{2.36}$$

2.2.3 Tangential Impulse Fly-Around Manoeuvre

The tangential impulse fly-around manoeuvre, shown in Figure 2.4, is often used as a precursor to a R-bar approach manoeuvre. The tangential impulse fly-around manoeuvre is similar to the Hohmann manoeuvre from an operational point of view: both manoeuvres require half an orbital period to complete and the magnitude of the initial impulse, ΔV_{y1}, is of same value for both manoeuvres (see equation (2.35)). However, for the tangential impulse fly-around manoeuvre, the second impulse, ΔV_{y2}, must reduce the relative velocity between the chaser and target to zero, and therefore, it must take into account the orbital velocity difference between both spacecraft.

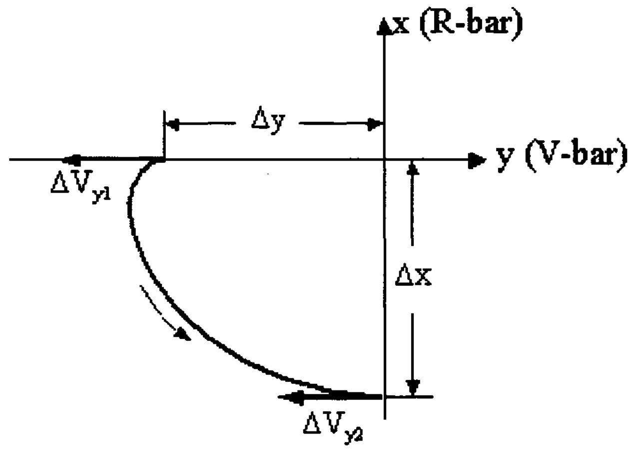

Figure 2.4: Tangential Impulse Fly-Around Manoeuvre [Fehse 2003].

The orbital velocity difference, $\delta \dot{y}_{rel}$, at a position Δx on the R-bar, with $\Delta y = 0$, is given by Fehse (2003) as:

$$\delta \dot{y}_{rel} = \frac{3\dot{\theta}}{2} \Delta x \tag{2.37}$$

such that the magnitude of the second impulse, ΔV_{y2}, after adding the ΔV given in equation (2.35), becomes

$$\Delta V_{y2} = \frac{7\dot{\theta}}{4} \Delta x \tag{2.38}$$

and the total ΔV fuel usage turns out to be

$$\Delta V_{total} = 2\dot{\theta}\,\Delta x \tag{2.39}$$

An R-bar approach manoeuvre or a station-keeping manoeuvre needs to be applied together with, or directly after the second impulse; if not, the chaser will drift with respect to the target because of the orbital altitude difference between both spacecraft. Finally, in the case of a first impulse misfire, the chaser will be placed in a different orbit than the target, and thus, a possible collision may occur depending on the misfire. Tangential impulse manoeuvres are rarely used for transfers along the V-bar axis for such reasons, and radial impulse manoeuvres are preferred instead.

2.2.4 Radial Impulse Manoeuvre

Instead of a transfer along the V-bar by impulses in the orbit direction, a radial impulse manoeuvre is often used since it is a safer alternative (see Fehse, 2003 for more details concerning these manoeuvres). Radial impulse manoeuvres do not cause drift with respect to the target spacecraft, as they only affect the eccentricity, not the orbital period of the chaser spacecraft. Their widespread use can also be attributed to the fact that these manoeuvres are generally more fuel-efficient than straight-line V-bar approach manoeuvres. Figure 2.5 shows the manoeuvre sequence for these manoeuvres, which take half an orbital period to complete.

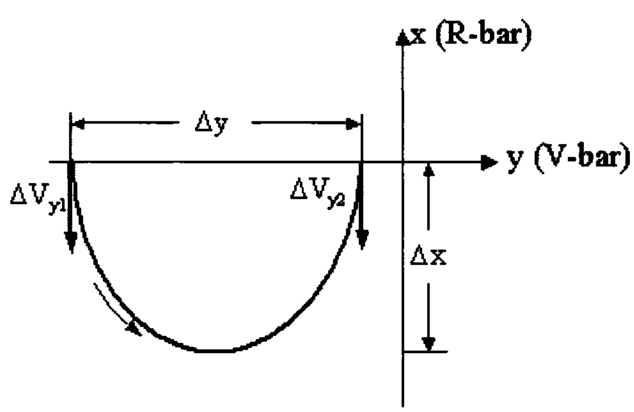

Figure 2.5: Radial Impulse Manoeuvre [Fehse 2003].

The magnitudes of the initial impulse, ΔV_{x1}, and the final impulse, ΔV_{x2}, are equal. More importantly, in order to keep the target spacecraft in the rendezvous sensor's field of view (FOV), both are limited to the maximum allowable altitude difference, Δx, at a specific chaser position.

The initial and final impulse magnitudes are given by Fehse (2003) and are expressed as

$$\Delta V_{x1} = \Delta V_{x2} = \frac{\dot{\theta}}{4}\Delta x \tag{2.40}$$

Therefore, the total ΔV fuel requirement for this type of manoeuvre at the chaser's current position is given by

$$\Delta V_{total} = \frac{\dot{\theta}}{2}\Delta x \tag{2.41}$$

Even though this type of manoeuvre is more costly by a factor of $3\pi/2$ compared to the tangential impulse manoeuvres for a same V-bar displacement, they are mostly used in practice because of safety considerations.

2.2.5 Straight-line V-bar Approach Manoeuvre

Following a series of radial impulse manoeuvres, a straight-line V-bar approach manoeuvre is often used for the final approach to a docking port or a berthing box located on the chaser spacecraft. With this type of trajectory, lateral position deviations can be easily controlled with the use of rendezvous sensors or a human operator. In practice, because of orbital perturbations, these trajectories are always closed loop controlled.

The manoeuvre sequence is shown in Figure 2.6. If a constant approach velocity is assumed, a user specified initial impulse, ΔV_{y1}, produces velocity in the y-direction, V_y. For the duration (Δt) of the manoeuvre, the initial impulse is followed by the application of a continuous force, γ_x, in order to counteract orbital forces. In order to stop the relative motion, the manoeuvre sequence ends with the application of a final impulse, ΔV_{y2}, of equal magnitude as the initial impulse, but in the opposite direction.

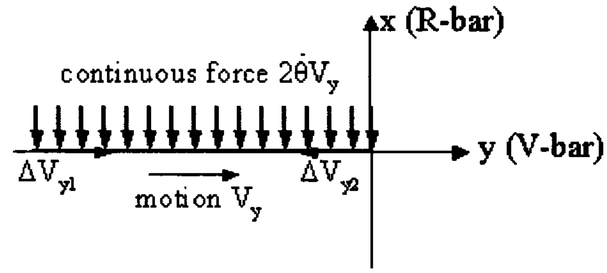

Figure 2.6: Straight-line V-bar Approach Manoeuvre [Fehse 2003].

Thus, the magnitudes of the first and final impulses are given as

$$\Delta V_{y1} = \Delta V_{y2} \tag{2.42}$$

As given by Fehse (2003), the continuous force per unit mass, γ_x, which needs to be applied in order to keep the chaser on the V-bar axis, is

$$\gamma_x = 2\dot{\theta}V_y \tag{2.43}$$

Finally, the total ΔV fuel requirement for this manoeuvre is

$$\Delta V_{total} = |\Delta V_{y1}| + |\gamma_x \Delta t| + |\Delta V_{y2}| \tag{2.44}$$

2.2.6 Straight-line R-bar Approach Manoeuvre

The final type of manoeuvre used in this study is the straight-line R-bar approach manoeuvre. Along with the straight-line V-bar approach, this type of manoeuvre is used for final approach to a docking port or berthing box located on the target spacecraft. In cases where a final approach is not possible via the V-bar axis, the R-bar manoeuvre is preferred. If a constant approach velocity is assumed, the resulting manoeuvre sequence is shown in Figure 2.7. An initial impulse is used to start motion resulting in a constant velocity, V_x. Unlike the straight-line V-bar approach manoeuvre, two additional forces, γ_x and γ_y, are needed in order to counteract orbital forces and to keep the chaser on the R-bar axis. At the conclusion of the manoeuvre sequence, a final impulse of same magnitude but opposite in direction of the initial impulse is fired to stop the relative motion.

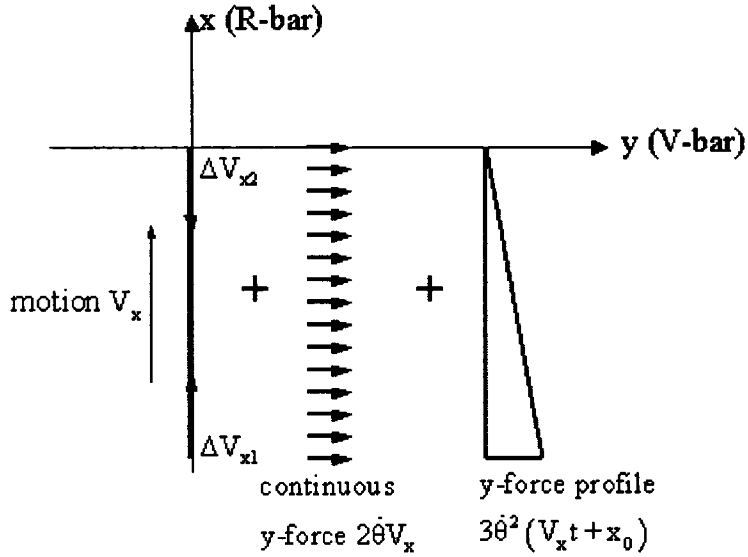

Figure 2.7: Straight-line R-bar Approach Manoeuvre [Fehse 2003].

Hence, the magnitudes of the first and final impulses are given as

$$\Delta V_{x1} = \Delta V_{x2} \tag{2.45}$$

The continuous forces per unit mass, γ_x and γ_y, needed in order to keep the chaser on the R-bar axis for the duration (Δt) of the manoeuvre, are expressed as the following equations, taken from Fehse (2003):

$$\gamma_x = 3\dot{\theta}^2 (V_x t + x_0) \tag{2.46}$$

$$\gamma_y = 2\dot{\theta} V_x \tag{2.47}$$

The total ΔV fuel requirement for the straight-line R-bar approach manoeuvre is

$$\Delta V_{total} = \left|\Delta V_{x1}\right| + \left|\sqrt{\left(\gamma_x \Delta t\right)^2 + \left(\gamma_y \Delta t\right)^2}\right| + \left|\Delta V_{x2}\right| \tag{2.48}$$

2.3 RENDEZVOUS SIMULINK SIMULATOR

In this section, a short description of the numerical implementation regarding the rendezvous SIMULINK simulator is presented. In the rendezvous SIMULINK simulator, there are 12 first order differential equations that are being integrated, hence those in section 2.1, while those in section 2.2 are only integrated when they are needed. The integration in SIMULINK was done using the fourth-order Runge Kutta method. The time step was fixed at half a second and each simulation usually took approximately ten minutes to complete on a desktop computer, such that the simulations are not relatively numerically intense. The simulator was validated by comparing results for the reference orbit propagation with those obtained from AGI's Satellite Tool Kit (STK) software.

In conclusion, the analytical expressions related to spacecraft rendezvous were presented in this chapter. In the next chapter, various rendezvous trajectories are presented and analysed with respect to ΔV fuel consumption, time of flight (TOF) and operational constraints related to the TECSAS mission.

CHAPTER 3 - TECSAS RENDEZVOUS ANALYSIS

The terminal rendezvous analysis related to the TECSAS mission is presented in this chapter. Three terminal rendezvous trajectories are evaluated in terms of ΔV fuel consumption and time of flight (TOF) within the TECSAS mission guidelines. The chapter is divided into three sections. In the first section, each terminal rendezvous trajectory is presented along with some of its advantages, disadvantages, and safety considerations. This is followed by simulation results for each case and finally, a general discussion is presented in the last section.

3.1 TERMINAL RENDEZVOUS TRAJECTORIES

As mentioned above, only the terminal phases of various rendezvous trajectories are analysed in this study. Therefore, it is assumed that both orbit phasing and far range rendezvous operations are completed and are successful, such that close range rendezvous, or terminal rendezvous, operations can be initiated. It is also supposed that all inclination errors have been dealt with during orbit phasing operations; both spacecraft are assumed to be orbiting in the target's orbital plane. Thus, the initial conditions of the chaser spacecraft in the relative motion reference frame are taken to be approximately 3 km behind and 250 m below the target spacecraft. Finally, both the chaser and target spacecraft are assumed to be identical and therefore, have the same characteristics as specified in Table 1.2 of section 1.2. Both spacecraft are expected to maintain a constant attitude such that their orientation dynamics are neglected. All terminal rendezvous trajectory scenarios analysed in this chapter are constrained by these initial conditions.

Three terminal rendezvous trajectories are considered in this study: one V-bar approach and two R-bar approaches. Since the TECSAS mission is still in the preliminary planning phase, the choice of which approach axis to use during the final terminal approach has not been determined. For this reason, both a V-bar and a R-bar approach are considered and are compared in this study.

3.1.1 Lidar-based V-bar Approach Trajectory

The first terminal rendezvous trajectory considered, shown in Figure 3.1, is the ***lidar-based V-bar approach trajectory***. This trajectory is similar to one mentioned in Pelletier et al. (2003) and is composed of 4 phases (the boundaries between phases are shown by bullets in Figure 3.1), which are the following:

I - *Drift orbit*: used until specified point from which the second phase is implemented.

II - *Hohmann transfer*: used in order to position the chaser spacecraft at a hold point on the target V-bar axis at approximately 1.3 km behind the target spacecraft. At this point in the trajectory, the chaser's lidar instrument can begin tracking the target.

III - *Radial impulse manoeuvres*: computed to maintain the target within the field of view (FOV) of the chaser's lidar instrument (10°, half cone angle).

IV - *Straight-line V-bar approach manoeuvre*: initiated from approximately 100 m behind the target spacecraft until capture in order to complete the rendezvous trajectory.

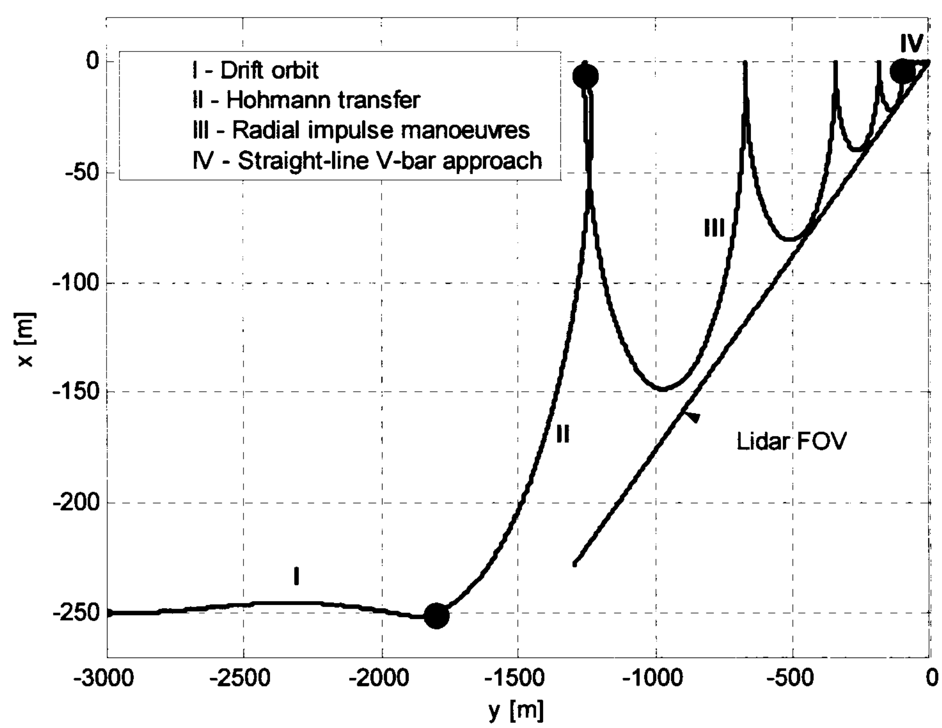

Figure 3.1: Lidar-based V-bar Approach Trajectory.

Besides being a relatively simple terminal rendezvous trajectory from an operational viewpoint, each individual phase of this trajectory has some advantages and safety considerations, which are presented here along with some of their disadvantages (Fehse, 2003, and Pelletier et al., 2003).

I – The drift orbit has the following characteristics:

i. Low propellant consumption.
ii. Low complexity.
iii. Inherently safe and provides a safe flyby in case of a mission failure.
iv. Natural closing orbit while ground-based orbit determination proceeds.

II – The Hohmann transfer has the following characteristics:

i. Minimum fuel manoeuvre.
ii. Low complexity.
iii. Manoeuvre ends with hold point on target V-bar axis, which permits systems checkouts before proceeding.
iv. Resulting trajectory is safe with respect to collision even in the case of a first impulse misfire. However, a collision avoidance manoeuvre (CAM) might be needed in the case of a second impulse misfire.

III – The radial impulse manoeuvres have the following characteristics:

i. Radial hops can be reduced as range decreases to accommodate lidar field of view (FOV) constraint.
ii. Inherently safe.
iii. No plume impingement of target.

IV – The straight-line V-bar approach manoeuvre has the following characteristics:

i. Natural progression from radial impulse manoeuvres.
ii. Safety depends on the chaser's relative velocity during the approach phase. In the case of a failed trajectory control system, a collision avoidance manoeuvre (CAM) is needed.

In section 3.2.1, the effects, both on overall ΔV and on total time of flight (TOF), of trading radial impulse manoeuvres for longer V-bar approaches are examined.

3.1.2 R-bar Approach Trajectory with V-bar Station Keeping

The second terminal rendezvous trajectory considered is the ***R-bar approach with V-bar station keeping trajectory*** as shown in Figure 3.2. A similar trajectory is shown in Fehse (2003), however no trade-off analysis between ΔV fuel consumption and time of flight (TOF) pertaining to this trajectory was performed.

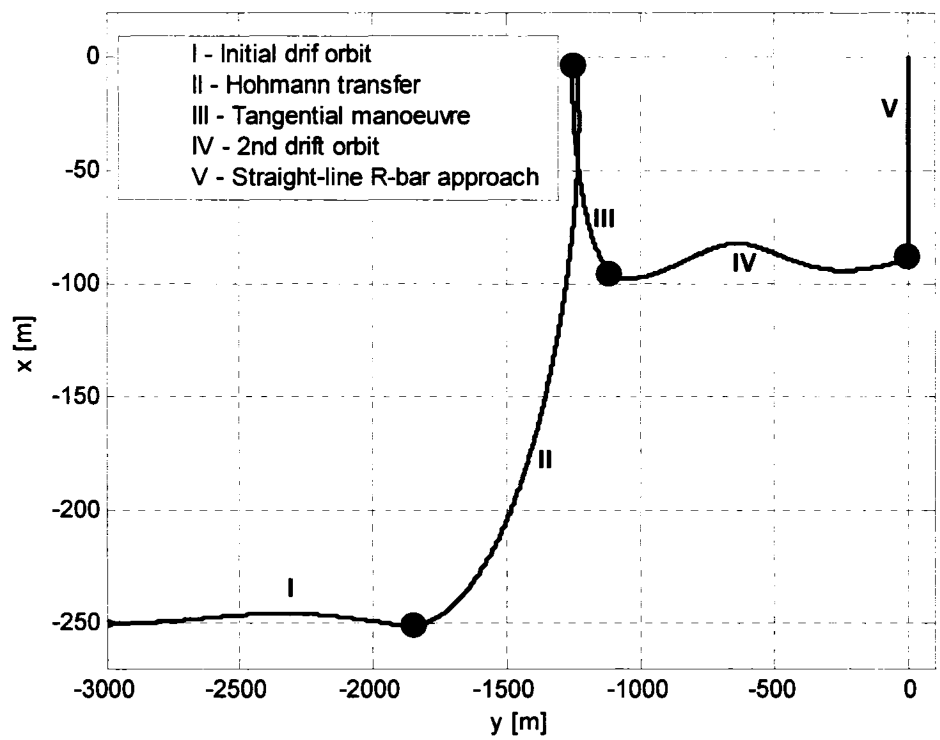

Figure 3.2: R-bar Approach with V-bar Station Keeping Trajectory.

As can be seen from Figure 3.2, the considered trajectory is made up of 5 phases:

I - *Drift orbit*: used until specified point from which the second phase is implemented.

II - *Hohmann transfer*: used in order to position the chaser spacecraft at a hold point on the target V-bar axis at approximately 1.3 km behind the target spacecraft.

However, contrary to the first rendezvous trajectory considered, no lidar-controlled manoeuvres are incorporated in the subsequent phases of this trajectory.

III - *Tangential impulse fly-around manoeuvre*: used in order to place the chaser in a second drift orbit.

IV - *2nd Drift orbit*: used until the chaser is in close proximity to the R-bar axis of the target and the final phase is implemented.

V - *Straight-line R-bar approach manoeuvre*: initiated from approximately 100 m below the target spacecraft until capture. This manoeuvre concludes the rendezvous attempt.

Compared to the first trajectory (see section 3.1.1), phases III and V of this terminal rendezvous trajectory have the following advantages, disadvantages and safety considerations:

III – The tangential manoeuvre has the followings characteristics:

i. Minimum fuel manoeuvre.
ii. Low complexity.
iii. Relatively safe if first thrust firing is complete, if not, a collision avoidance manoeuvre (CAM) might be needed depending on thrust misfire.

V – The straight-line R-bar approach manoeuvre has the following characteristics:

i. Natural progression from drift orbit.
ii. Safety depends on velocity during approach phase. A collision avoidance manoeuvre (CAM) might be needed if guidance and control systems failed.

In order to find a compromise between the overall ΔV fuel budget and time of flight (TOF) spent in the drift orbit, the R-bar approach distance is varied while keeping the chaser's velocity constant during the approach phase. These trajectory variations are studied in section 3.2.2.

3.1.3 Drift Orbit and R-bar Approach Trajectory

Finally, the third terminal rendezvous trajectory considered, shown in Figure 3.3, the ***drift orbit and R-bar approach trajectory***, is a simplified version of the second rendezvous trajectory considered (in section 3.1.2). This third rendezvous trajectory consists of only two phases:

I - *Drift orbit*: used until the chaser spacecraft reaches the target's R-bar axis.

II - *Straight-line R-bar approach manoeuvre*: initiated from approximately 230 m below the target spacecraft until capture.

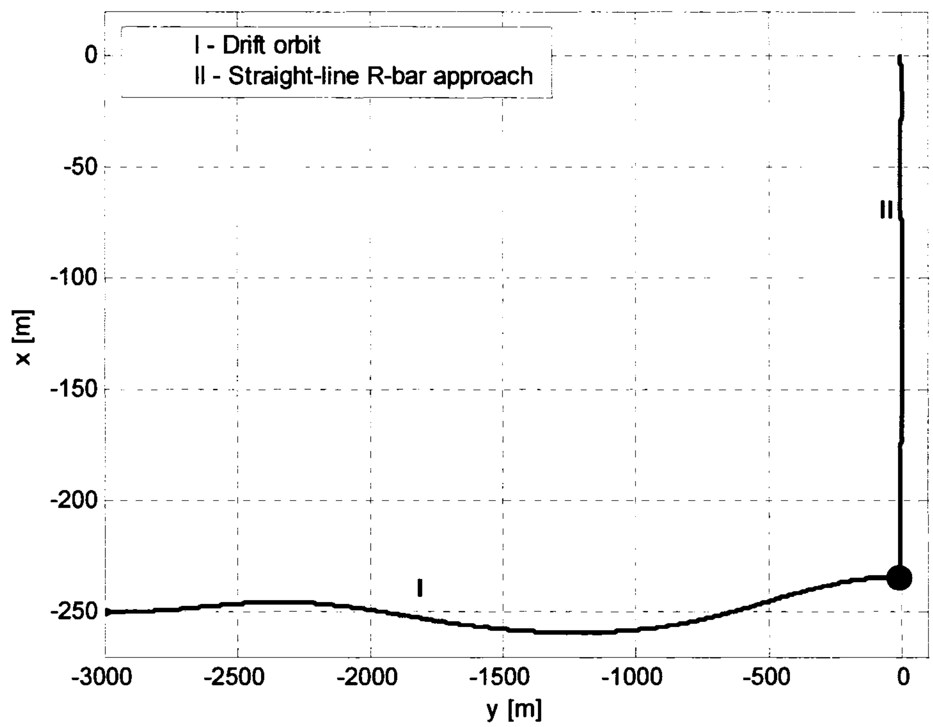

Figure 3.3: Drift Orbit and R-bar Approach Trajectory.

The advantages of this trajectory are the low complexity in terms of trajectory elements, the safety and low propellant consumption associated with the drift orbit, and finally, the relative safety of the straight-line R-bar approach as mentioned in section 3.1.2. In section 3.2.3, the R-bar approach velocity profile is varied in order to study its effects on overall ΔV fuel consumption and time of flight (TOF).

3.2 SIMULATION RESULTS

In this section, simulation results for all three terminal rendezvous trajectories are presented. For the first terminal rendezvous trajectory, the *lidar-based V-bar approach trajectory*, three variations of this trajectory are studied. Four variations, of the second terminal rendezvous trajectory, the *R-bar approach with V-bar station keeping trajectory*, are examined. Finally, five variations of the *drift orbit and R-bar approach trajectory* are analysed.

3.2.1 Lidar-based V-bar Approach Trajectory

In the case of the *lidar-based V-bar approach trajectory*, the V-bar approach distance (phase IV distance) has been increased from the original value of 95 m to 180 m, and subsequently to 345 m, while reducing the number of radial impulse manoeuvres. Thus, as shown in Figure 3.4, the trajectories are almost identical except for phases III and IV (described in section 3.1.1). For these three trajectory variations, the in-track velocity during the V-bar approach phase is maintained constant at 0.01 m/s and a control system is used in order to keep the chaser spacecraft to within ±1 m of the target's V-bar axis. In addition, a second control system is employed (for all trajectories in this study) in order to maintain the chaser spacecraft to within ±5 m of the target's z-axis (cross-track direction).

Table 3.1 gives the results for the V-bar approach variations associated with the *lidar-based V-bar approach trajectory*. It can be seen that as the approach distance gets greater, both the total ΔV fuel budget and total time of flight (TOF) increase. The increase in ΔV fuel consumption and time of flight is due to the fact that less radial impulse manoeuvres are needed as the approach distance is increased and that radial impulse manoeuvres are more efficient manoeuvres in terms of ΔV fuel consumption than the straight-line V-bar manoeuvre.

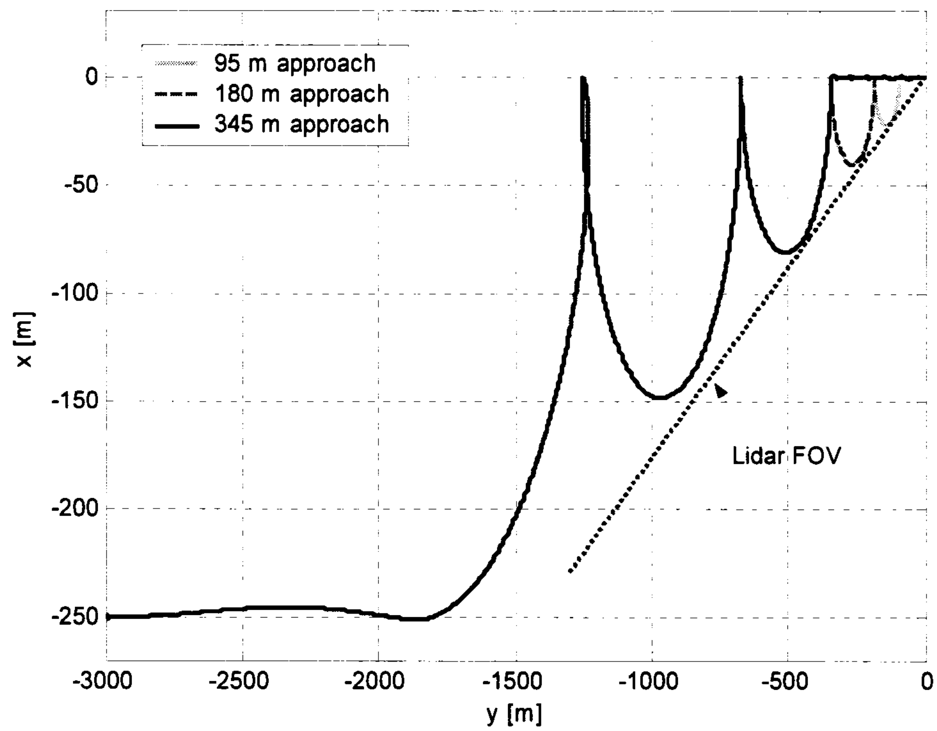

Figure 3.4: Lidar-based V-bar Approach Trajectory: Approach Distance Variations.

Comparing the 95 m V-bar approach to the 180 m V-bar approach shows that when the V-bar distance is double, there is an increase of 15% in total ΔV fuel consumption (from 1.26 m/s to 1.45 m/s) and an increase of 20% in total time of flight (TOF) (from 432 min to 518 min). However, comparing the 180 m V-bar approach to the 345 m V-bar approach shows an increase of 48% in overall ΔV fuel consumption (from 1.45 m/s to 2.15 m/s), along with an increase of 40% in total time of flight (TOF) (from 518 min to 724 min). From this, it can be reasoned that the 345 m V-bar approach is the least desirable choice between the three trajectory variations.

In addition, by comparing only the V-bar approach manoeuvres, it can be seen that the relationships between the corresponding approach distances, ΔV fuel consumption, and time of flight (TOF) are almost linear. In the case of the 95 m and 180 m approach distance, an increase of 89% in approach distance (from 95 m to 180 m) results in an increase of 80% for ΔV fuel consumption (from 0.35 m/s to 0.63 m/s) and 89% for time of flight (TOF) (from 149 min to 282 min). These same relationships hold when comparing the other two approaches. The linearity of these relationships is due to the fact that a constant approach velocity, or in-track velocity, is assumed in these simulations.

Table 3.1: Lidar-Based V-bar Approach Trajectory Manoeuvre Characteristics

Manoeuvres \ Approach distance	95 m	180 m	345 m
I – Drift orbit			
TOF	46 min	46 min	46 min
II – Hohmann transfer			
TOF	48 min	48 min	48 min
$\lvert\Delta V\rvert$	0.14 m/s	0.14 m/s	0.14 m/s
III – Radial impulse manoeuvres			
TOF	189 min	142 min	95 min
$\lvert\Delta V\rvert$	0.69 m/s	0.60m/s	0.51 m/s
IV – Straight-line V-bar approach			
TOF	149 min	282 min	535 min
$\lvert\Delta V\rvert$	0.35 m/s	0.63 m/s	1.40 m/s
Control system for z - axis $\lvert\Delta V\rvert$	0.08 m/s	0.08 m/s	0.10 m/s
Total TOF	432 min	518 min	724 min
Total $\lvert\Delta V\rvert$	1.26 m/s	1.45 m/s	2.15 m/s

Furthermore, as the approach distance is increased, more control thrusts are needed in order to keep the chaser spacecraft near the target's V-bar axis during the final approach. By increasing the approach distance, the chaser spacecraft is affected by the orbital perturbations during a longer period and the control system must counteract their effects during a longer period. However, for the first two trajectory variations, the control thrust ΔV fuel consumption differences are small and are only perceived when comparing these cases to the 345 m V-bar approach.

In conclusion, if a minimum approach distance is not an operational constraint, the 95 m V-bar approach is the optimal terminal rendezvous trajectory for the *lidar-based V-*

bar approach trajectory because the overall ΔV fuel consumption and time of flight (TOF) values are minimum compared to the other trajectory variations. However, if mission constraints do not permit such a close approach, then the 180 m V-bar approach is the optimal choice.

3.2.2 R-bar Approach Trajectory with V-bar Station Keeping

In this study, four variations of the *R-bar approach with V-bar station keeping trajectory* are analysed in which the R-bar approach distance (phase V distance) is varied from an initial value of 90 m, to 117 m, 139 m, and finally to a final value of 161 m. The resulting trajectories are shown in Figure 3.5. In all four cases, the radial velocity during the final R-bar approach phase varies from an initial value of 0 m/s up to a maximum value of 0.026 m/s and finally, is 0.01 m/s at capture. Also, in order to counteract orbital perturbations and to keep the chaser spacecraft to within ±1 m of the target's R-bar axis, a control system is employed.

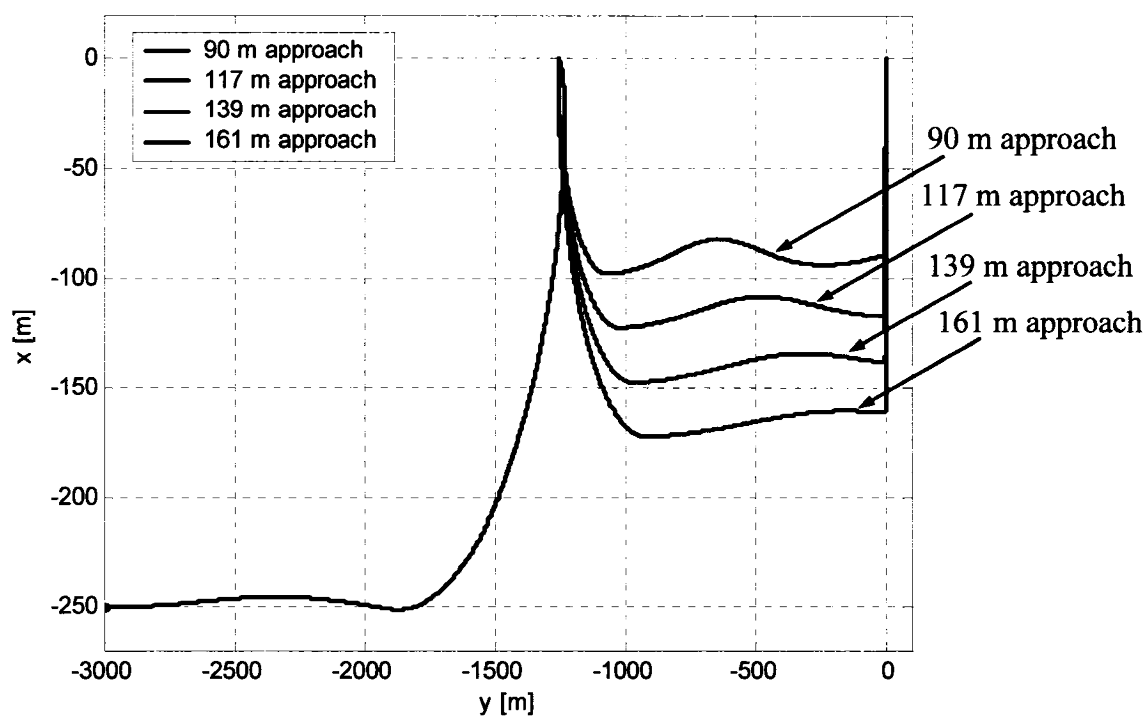

Figure 3.5: R-bar Approach Trajectory with V-bar Station Keeping: Approach Distance Variations.

From Table 3.2, it can be seen that as the R-bar approach distance increases, so does the overall ΔV fuel budget (from an initial value of 1.70 m/s up to 3.56 m/s). However, the total time of flight (TOF) diminishes (from an initial value of 359 min down to 327 min) because of time gained during the second drift orbit.

Table 3.2: R-bar Approach Trajectory with V-bar Station Keeping Manoeuvre Characteristics

Manoeuvres \ Approach distance	**90 m**	**117 m**	**139 m**	**161 m**
I – Drift orbit				
TOF	46 min	46 min	46 min	46 min
II – Hohmann transfer				
TOF	48 min	48 min	48 min	48 min
$\lvert\Delta V\rvert$	0.14 m/s	0.14 m/s	0.14 m/s	0.14 m/s
III – Tangential impulse manoeuvre				
TOF	23 min	23 min	23 min	23 min
$\lvert\Delta V\rvert$	0.17 m/s	0.21 m/s	0.25 m/s	0.29 m/s
IV – 2nd Drift orbit				
TOF	120 min	90 min	71 min	57 min
V – Straight-line R-bar approach				
TOF	122 min	124 min	144 min	153 min
$\lvert\Delta V\rvert$	1.33 m/s	1.88 m/s	2.60 m/s	3.07 m/s
Control system for z - axis $\lvert\Delta V\rvert$	0.06 m/s	0.06 m/s	0.06 m/s	0.06 m/s
Total TOF	359 min	331 min	332 min	327 min
Total $\lvert\Delta V\rvert$	1.70 m/s	2.29 m/s	3.05 m/s	3.56 m/s

Also, from Figure 3.6, it can be seen that the relationship between the time spent in the drift orbit and the straight-line R-bar approach manoeuvre ΔV fuel consumption is a quadratic relationship, such that fuel consumption can increase rapidly when comparing various trajectory variations.

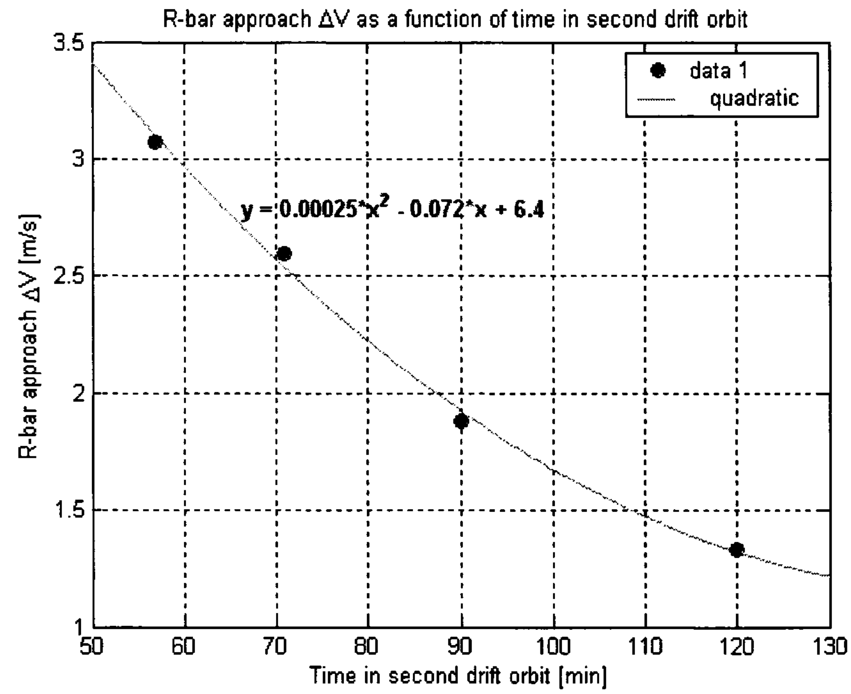

Figure 3.6: R-bar Approach ΔV as a Function of Time in Second Drift Orbit.

By comparing the 90 m R-bar approach to the 117 m R-bar approach, it can be seen that for an increase of 30% in approach distance (from 90 m to 117 m), the time spent in the drift orbit is decreased by 25% (from 120 min to 90 min). Also, the overall ΔV fuel budget is increased by 35% (from 1.70 m/s to 2.29 m/s) and the total time of flight (TOF) is decreased by 8% (from 359 min to 331 min). At the other extreme, comparing the 90 m R-bar approach to the 161 m R-bar approach, which is a 79% increase in approach distance, one can note that the decrease in overall time of flight is of 9% (from 359 min to 327 min), while the increase in total ΔV fuel budget is of 110% (from 1.70 m/s to 3.56 m/s). Therefore, it can be reasoned that the gain in time of flight is negligible compared to increase cost in ΔV fuel consumption, such that an optimal trajectory must be selected by ΔV fuel consumption and/or approach distance constraints. In the case where a minimum approach distance is not an operational constraint, the 90 m R-bar approach is the optimal terminal rendezvous trajectory for the *R-bar approach with V-bar station keeping trajectory* because the overall ΔV fuel consumption is at minimum compared to the other trajectory variations. However, if mission constraints do not permit such a close R-bar approach, then the closest allowable approach distance is the best choice.

3.2.3 Drift Orbit and R-bar Approach Trajectory

For the last trajectory studied, the *drift orbit and R-bar approach trajectory*, (see Figure 3.3), the corresponding radial velocity profiles were varied during the R-bar approach manoeuvre and are shown in Figure 3.7. For all five cases, the maximum radial velocity was approximately 0.05 m/s, while the radial velocity at capture was varied from 0.002 m/s up to 0.02 m/s, as can be seen in Figure 3.7. Again, a control system is employed in order to counteract orbital perturbations and to keep the chaser spacecraft to within ±1 m of the target's R-bar axis.

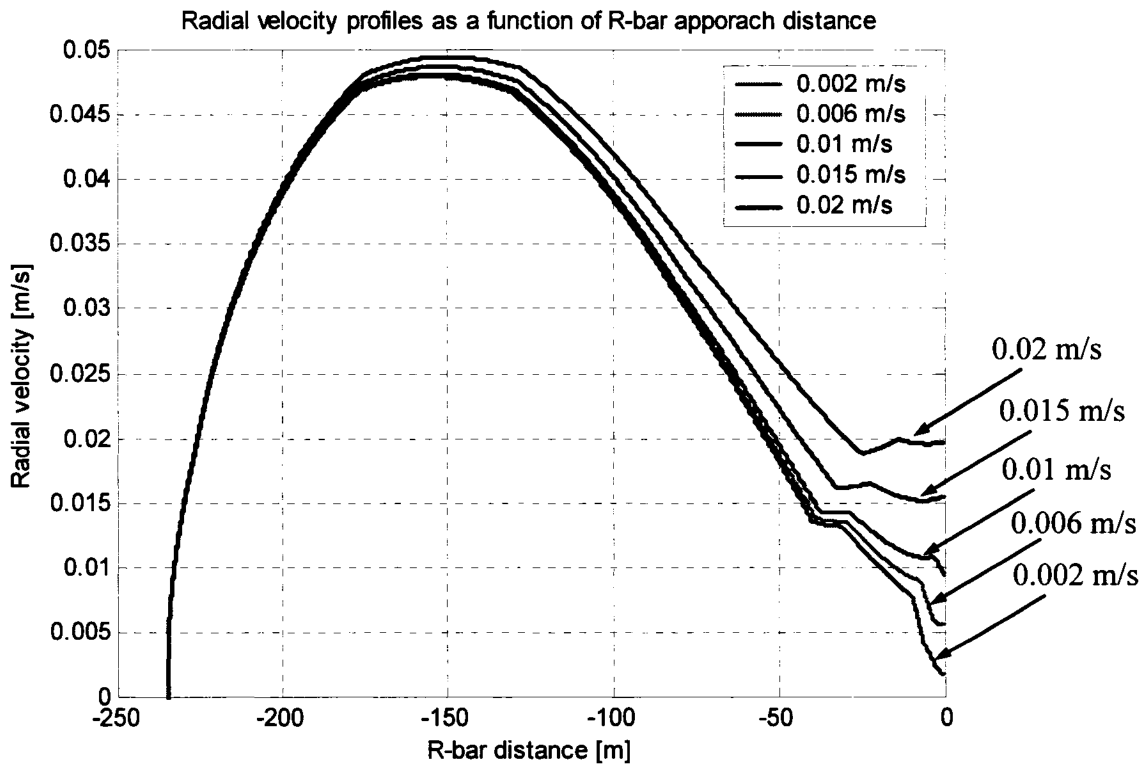

Figure 3.7: Drift Orbit and R-bar Approach Trajectory: Radial Velocity Profile Variations.

Table 3.3 shows the impact of varying the radial velocity profile during the course of the R-bar approach manoeuvre. Furthermore, Figure 3.8 shows that there exists a quadratic relation between the R-bar approach manoeuvre ΔV fuel consumption and the desired radial end velocity, such that ΔV fuel consumption decreases significantly if a faster radial end velocity is allowed before capture.

Table 3.3: Drift Orbit and R-bar Approach Trajectory Manoeuvres Characteristics

R-bar approach end velocity / Manoeuvres	**0.002 m/s**	**0.006 m/s**	**0.01 m/s**	**0.015 m/s**	**0.02 m/s**
I – Drift orbit					
TOF	121 min	121 min	121 min	121 min	121 min
II – Straight-line R-bar approach					
TOF	203 min	169 min	157 min	140 min	128 min
$\lvert\Delta V\rvert$	3.41 m/s	3.37 m/s	3.33 m/s	3.23 m/s	3.12 m/s
Control system for z - axis $\lvert\Delta V\rvert$	0.06 m/s	0.06 m/s	0.06 m/s	0.06 m/s	0.06 m/s
Total TOF	324 min	290 min	278 min	261 min	249 min
Total $\lvert\Delta V\rvert$	3.47 m/s	3.43 m/s	3.39 m/s	3.29 m/s	3.18 m/s

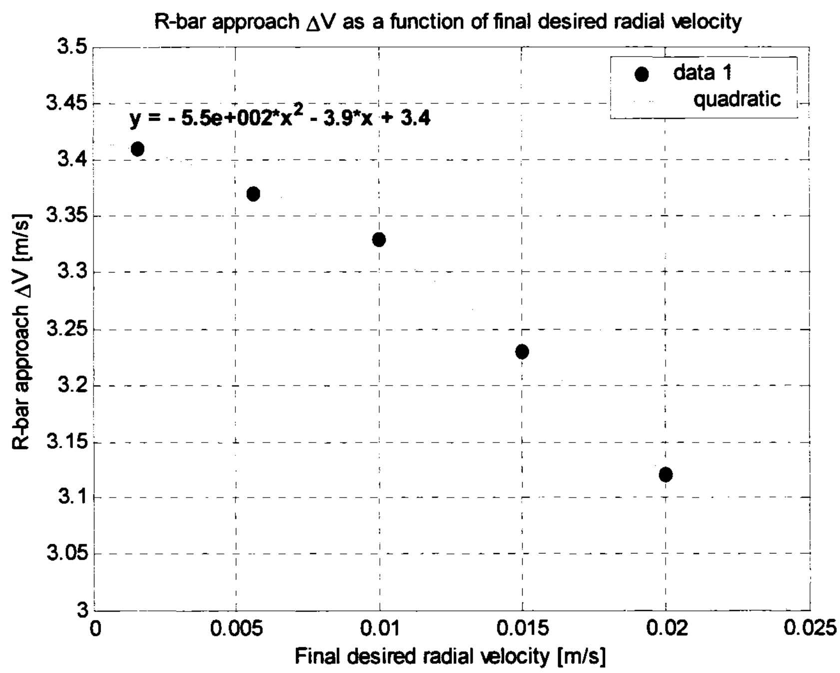

Figure 3.8: R-bar Approach ΔV as a Function of Desired Final Radial Velocity.

Comparing the case of a 0.002 m/s radial end velocity to the 0.01 m/s radial end velocity case shows that the overall ΔV fuel consumption decreases by only 2% (from 3.47 m/s to 3.39 m/s) and that the total time of flight (TOF) decreases by 14% (from 324 min to 278 min). These savings might be negligible, however greater savings can be made if mission constraints allow for a faster chaser radial velocity at capture. For an example, comparing the 0.015 m/s end velocity to the 0.002 m/s end velocity shows that the total ΔV fuel consumption decreases by 5% (from 3.47 m/s to 3.29 m/s), while the overall time of flight (TOF) is decreased by 19% (from 324 min to 261 min).

In conclusion, it is difficult to choose an optimal solution in the case of the *drift orbit and R-bar approach trajectory* because the overall ΔV fuel savings are small when the radial end velocity is increased slightly. However, depending on actual mission constraints, such savings could be vital to mission and/or spacecraft design and thus to the realisation of the mission itself.

3.3 DISCUSSION

In this section, three terminal rendezvous trajectories are compared with a goal of determining the best trajectory. Since the TECSAS mission is still in the preliminary planning phase and the target spacecraft has not yet been specified, it is not possible to reject either the V-bar approach or the R-bar approach on target spacecraft constraints alone. Therefore, the optimal trajectory must be chosen with regards to overall ΔV fuel consumption, time of flight (TOF) values and safety considerations.

First, it is obvious that the third rendezvous trajectory, the *drift orbit and R-bar approach trajectory*, is not an optimal terminal rendezvous trajectory because of its excessive ΔV fuel budget values compared to the other two trajectories. For this reasons, the *drift orbit and R-bar approach trajectory* is eliminated as a possible choice.

Comparing the *lidar-based V-bar approach trajectory* to the *R-bar approach with V-bar station keeping trajectory* shows that the former requires less total ΔV fuel budget by 35% than the latter (from 1.26 m/s to 1.70 m/s). However, the overall time of flight (TOF) is significantly less, by 20%, for the *R-bar approach with V-bar station keeping trajectory* with respect to the *lidar-based V-bar approach trajectory* (from 359 min to 432 min respectively). Having said this, the *R-bar approach with V-bar station keeping trajectory* is more complex from an operational point of view because it has more trajectory phases. Furthermore, the R-bar approach manoeuvre itself is not as simple to perform as the straight-line V-bar approach because of the thrusts involved. Also, because both spacecraft are situated in the same orbit, the V-bar approach manoeuvre is a relatively safer alternative than the R-bar approach manoeuvre.

For all of these reasons, it can be argued that the lidar-based V-bar approach trajectory with a 95 m approach distance is the best terminal rendezvous trajectory presented in this study and if the constraints of the TECSAS mission permit a V-bar approach and capture, such a trajectory should be considered by the mission design team. In the next chapter, the equations of motion related to spacecraft formation flying are developed.

CHAPTER 4 - SPACECRAFT FORMATION FLYING

In this chapter, the equations of motion used to describe spacecraft formation flying are presented. The chapter outline is similar to the second chapter: a section describing the geometry and coordinate system associated with spacecraft relative motion are first presented, which is then followed by two sections devoted to the equations of motion describing relative motion and reference orbit propagation. Subsequently, the necessary initial conditions pertaining to specific spacecraft formations are presented and in the last section of this chapter, the implementation of a linear quadratic regulator (LQR) controller is discussed.

4.1 COORDINATE FRAMES

Spacecraft rendezvous and formation flying both describe the relative motion of one spacecraft, the deputy or chaser, to another, the chief or target. The equations of motion used to describe relative motion for formation flying analyses and reference orbit propagation are presented in this section. Figure 4.1 (similar to Figure 2.1), shows the geometry of the chief and deputy spacecraft with respect to the reference orbit.

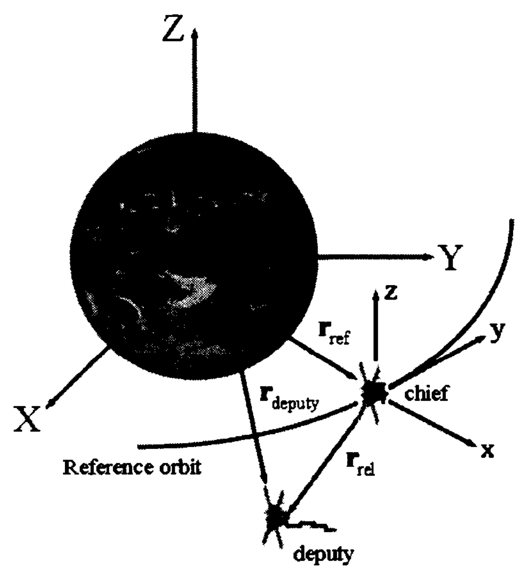

Figure 4.1: Coordinate Systems for Relative Motion Analysis.

As was the case for the spacecraft rendezvous formulation, two reference frames are used in this formulation: the Earth-Centered Inertial (ECI) reference frame (designated by the *XYZ* axes) and the Hill frame, or relative motion reference frame (designated by the *xyz* axes). The descriptions of these reference frames are the same as those of section 2.1 and shall not be repeated here. However, there exist two differences between the two formulations. The first difference is that in the case of the formation flying formulation, the Hill frame is attached to the centre of mass of an imaginary spacecraft orbiting in the reference orbit instead of being attached to the target spacecraft in chapter 2. However, by adjusting the chief's initial conditions, it can behave exactly like the imaginary spacecraft and thus, the reference orbit becomes the chief's orbit, as was the case in chapter 2.

The second difference between the formation flying and rendezvous formulation is that two sets of equations of motion are used in the formation flying formulation instead of one set as was the case for the rendezvous formulation. The first set of equations describes the relative motion of the chief spacecraft with respect to the reference orbit, while the second set describes the relative motion of the deputy spacecraft with respect to the reference orbit. The resulting Hill positions and velocities are then subtracted from each other in order to get the relative motion of the deputy with respect to the chief spacecraft in the Hill frame.

Thus, the position of a spacecraft, either the deputy or the chief, with respect to the reference orbit in the relative reference frame is given by

$$\mathbf{r}_{rel} = \begin{bmatrix} x & y & z \end{bmatrix}^T \tag{4.1}$$

where x, y, and z are the Hill coordinates of the particular spacecraft considered.

4.1.1 Relative Motion Equations

To analyze the problem of TECSAS formation flying, when the total duration is much longer than in the case of spacecraft rendezvous, the basic C-W equations are inadequate because they neglect orbital perturbations. Over time, the neglected orbital perturbations render the solution invalid. Thus, a set of equations that is more complete is needed. For this study, the formation flying equations of motion are based on the ones given by Schweighart and Sedwick (2002). They represent a set of linearized constant-coefficient differential equations of motion, similar to the C-W equations, but include the effect of the J_2 potential. Thus, they accurately describe the relative motion between a particular spacecraft with respect to an unperturbed reference circular orbit. These are given below:

$$\begin{aligned}&\ddot{x}-(nc)\dot{y}-\left(5c^2-2\right)n^2x=\\&-\left(3n^2J_2R_E^2/r_0\right)\left\{1/2-\left[3\sin^2 i_0\sin^2(kt)/2\right]-\left[5\left(1+3\cos 2i_0\right)/4\right]\right\}+f_{Drag\,x}+u_x\end{aligned} \tag{4.2}$$

$$\ddot{y}+2(nc)\dot{x}=-\left(3n^2J_2R_E^2/r_0\right)\sin^2 i_0\sin(kt)\cos(kt)+f_{Drag\,y}+u_y \tag{4.3}$$

$$\ddot{z}+q^2z=2lq\cos(qt+\phi)+f_{Drag\,z}+u_z \tag{4.4}$$

In these equations, x y z are the corresponding spacecraft's coordinates in the Hill frame, J_2 is the second spherical harmonic in the gravitational potential, R_E is the Earth's radius, r_0 is the reference orbit's radial distance, and i_0 is the reference orbit's initial inclination. The distance r_0 for the circular reference orbit is constant, but the radial vector rotates because of the effects of J_2. Additionally, atmospheric drag perturbations, given by $f_{Drag\,x}$, $f_{Drag\,y}$, and $f_{Drag\,z}$ are added in order to increase modeling accuracy. Constants q and l are defined later. Finally, control thrusts, given by u_x, u_y, and u_z which signal the implementation of a control system to maintain formation geometry as will be discussed later are also added to the equations of motion.

In equations (4.2) to (4.4), a number of constants and initial conditions, namely n, s, k, q, and l, are used as explained next. First, the rotation rate of the relative motion coordinate system attached to the reference orbit is given by

$$n = \sqrt{\mu / r_0^3} \tag{4.5}$$

where μ is the gravitational parameter.

Secondly, the following constants are used to correct the period of the reference orbit and to correct the reference orbit for nodal drift (Schweighart and Sedwick (2002)):

$$s = \frac{3J_2 R_E^2}{8r_0^2}(1 + 3\cos 2i_0) \tag{4.6}$$

$$c = \sqrt{1+s} \tag{4.7}$$

$$k = nc + \frac{3nJ_2 R_E^2}{2r_0^2}\cos^2 i_0 \tag{4.8}$$

Furthermore, in order to correctly model the secular motion present in the cross-track direction, the following constants are used to correct the cross-track motion (Schweighart and Sedwick (2002)):

$$i_{sat} = \dot{z}_0 / k\, r_0 + i_0 \tag{4.9}$$

$$\dot{\Omega}_{sat} = -\left(3nJ_2 R_E^2 / 2r_0^2\right)\cos i_{sat} \tag{4.10}$$

$$\dot{\Omega}_{ref} = -\left(3nJ_2 R_E^2 / 2r_0^2\right)\cos i_0 \tag{4.11}$$

$$q = nc - \left(\cos\gamma_0 \sin\gamma_0 \cot\Delta\Omega_0 - \sin^2\gamma_0 \cos i_{sat}\right)\left(\dot{\Omega}_{sat} - \dot{\Omega}_{ref}\right) - \dot{\Omega}_{sat}\cos i_{sat} \tag{4.12}$$

$$l = -r_0\left(\sin i_{sat} \sin i_0 \sin\Delta\Omega_0 / \sin\Phi_0\right)\left(\dot{\Omega}_{sat} - \dot{\Omega}_{ref}\right) \tag{4.13}$$

In addition, the following initial conditions are also used to correctly model the cross-track motion:

$$\Delta\Omega_0 = z_0/(r_0 \sin i_0) \tag{4.14}$$

$$\gamma_0 = \cot^{-1}\left(\cot i_0 \sin i_{sat} - \cos i_{sat} \cos\Delta\Omega_0/\sin\Delta\Omega_0\right) \tag{4.15}$$

$$\Phi_0 = \cos^{-1}\left(\cos i_{sat} \cos i_0 + \sin i_{sat} \sin i_0 \cos\Delta\Omega_0\right) \tag{4.16}$$

In the preceding equations (4.5) to (4.13), the orbital parameters that use the subscripts *ref* correspond to the reference orbit, which in this study is the TECSAS' orbit. Furthermore, the orbital parameters that use the subscripts *sat* correspond to the particular spacecraft chosen, i.e. either the deputy or the chief spacecraft.

Finally, the initial conditions $\dot{x}_0$ and $\dot{y}_0$ are specified in order to remove secular motion or constant offset terms, which give rise to the following equations:

$$\dot{x}_0 = y_0 n(1 - s/2c) \tag{4.17}$$

$$\dot{y}_0 = -2x_0 nc + \left(3J_2 R_E^2 n^2/4kr_0\right)\sin^2 i_0 \tag{4.18}$$

The major advantages of using equations (4.2) to (4.4) over the basic C-W equations are two fold: first, the J_2 perturbations are included in these equations and second, they are time averaged over an orbit. The fact that the J_2 perturbations are time averaged allows for faster numerical computation of these equations compared to other forms, so that longer simulations can be carried out. For further details pertaining to equations (4.2) to (4.18), the reader is referred to Schweighart and Sedwick (2002).

Additionally, in order to more accurately describe the relative motion between the two spacecraft, atmospheric drag perturbations are added to the equations of motion (4.2) to (4.4). For the formation flying formulation, the atmospheric drag perturbations acting on each spacecraft individually with respect to the unperturbed reference orbit are added to each set of equations of motion of the deputy and chief spacecraft. As was the case for the rendezvous formulation, each individual component is determined by the atmospheric drag equation as shown in Vallado (2001):

$$\mathbf{f}_{Drag} = -\frac{1}{2}\frac{C_D A}{m}\rho v_{spacecraft_{rel}} \mathbf{v}_{spacecraft_{rel}} \tag{4.19}$$

where C_D is the corresponding spacecraft's drag coefficient, A is the spacecraft's cross-sectional area, m is the spacecraft's mass, ρ is the atmospheric density at the given altitude and $\mathbf{v}_{spacecraft_{rel}}$ is the spacecraft's velocity relative to the Earth's atmosphere expressed in the Hill frame.

By using the same approach taken in section 2.1.1, the velocities of the deputy and chief spacecraft with respect to the rotating atmosphere expressed in the Hill frame, are given by the following

$$\mathbf{v}_{rel} = \begin{bmatrix} \dot{x} - ync + y\omega_E \cos i \\ \dot{y} + xnc + r_0 nc - (r_0 + x)\omega_E \cos i + z\omega_E \sin i \\ \dot{z} + y\omega_E \sin i \end{bmatrix} \tag{4.20}$$

where ω_E is the Earth's angular velocity, n is the mean motion as described by equation (4.5), c is the constant described by equation (4.7), and i is the reference orbit's inclination as described in the next section.

Finally, the atmospheric density, ρ, is evaluated from the same exponential model as was used for the spacecraft rendezvous formulation mentioned in section 2.1.1.

4.1.2 Reference Orbit Propagation

In conjunction with the exponential atmospheric model, a perturbed circular reference orbit is used in order to determine the position of the Hill reference frame in the Earth-Centered Inertial (ECI) Cartesian coordinate reference frame. This reference orbit takes into account the effect of the J2 perturbations and it is obtained from the circular nominal orbit by

$$\mathbf{r}_{ref} = r_0 \begin{bmatrix} \cos\Omega(t)\cos\theta(t) - \sin\Omega(t)\sin\theta(t)\cos i(t) \\ \sin\Omega(t)\cos\theta(t) + \cos\Omega(t)\sin\theta(t)\cos i(t) \\ \sin\theta(t)\sin i(t) \end{bmatrix} \tag{4.21}$$

where $\Omega(t)$ is the reference orbit's longitude of the ascending node, $\theta(t)$ is its argument of latitude, and $i(t)$ is the reference orbit's non-constant inclination. Because of the time averaged J_2 perturbations added to the C-W equations, these orbital elements need to be adjusted, such that the reference orbit is corrected for nodal drift as mentioned in Schweighart and Sedwick (2002). The resulting expressions are as follows:

$$i(t) = i_0 - \left(3\sqrt{\mu}J_2 R_E^2 \Big/ 2kr_0^{\frac{7}{2}}\right)\cos i_0 \sin i_0 \sin^2(kt) \tag{4.22}$$

$$\Omega(t) = \Omega_0 - \left(3\sqrt{\mu}J_2 R_E^2 \Big/ 2kr_0^{\frac{7}{2}}\right)\cos i_0 t \tag{4.23}$$

$$\theta(t) = kt \tag{4.24}$$

where the corresponding orbital constants and initial conditions are determined as mentioned earlier in section 4.1.1.

4.2 INITIAL CONDITIONS FOR SPACECRAFT FORMATIONS

In this section, the initial conditions necessary for specific spacecraft formations are presented. Because of the nature of the TECSAS mission and the interest of the Canadian Space Agency (CSA), the types of formations studied in this thesis are restricted to formations of two spacecraft useful for Earth sensing missions: the projected circular and in-track formations. In the next sections, details pertaining to each of these two formations are given.

4.2.1 Projected Circular Formation

Spacecraft placed in a projected circular formation maintain a fixed distance in the along-track/cross-track (y/z) plane. Therefore, the resulting motion in the y/z plane is a circle given by

$$y^2 + z^2 = d^2 \tag{4.25}$$

where d is the desired formation diameter. This type of formation is useful for Earth sensing missions because the distance between the two spacecraft is maintained constant when orbital perturbations are not taken into account or are compensated for with the use of control thrusts. Since both spacecraft are separated by a constant distance, effective interferometry is possible, which permits greater measurement resolution than in the case of a single spacecraft mission. The initial conditions for the projected circular formation given in terms of formation geometry are found in Sabol et al. (2001) and are given by

$$\Delta x_0 = (d/2)\cos\alpha \tag{4.26}$$

$$\Delta y_0 = d\sin\alpha \tag{4.27}$$

$$\Delta z_0 = d\sin\alpha \tag{4.28}$$

$$\Delta\dot{z} = 2\Delta\dot{x}_0 \tag{4.29}$$

where $\Delta\dot{x}_0$ and $\Delta\dot{y}_0$ are determined from equations (4.17) and (4.18), and α is the initial spacecraft phase angle in the along-track/cross-track (y/z) plane.

For control purposes, an unperturbed reference formation is needed in order to determine formation position and velocity errors over time. In the case of the projected circular formation, the reference formation is described as follows (taken from Vaddi and Vadali (2003)):

$$\Delta x_r = (d/2)\sin(nct+\alpha) \tag{4.30}$$

$$\Delta y_r = d\cos(nct+\alpha) \tag{4.31}$$

$$\Delta z_r = d\sin(nct+\alpha) \tag{4.32}$$

$$\Delta \dot{x}_r = (dnc/2)\cos(nct+\alpha) \tag{4.33}$$

$$\Delta \dot{y}_r = -dnc\sin(nct+\alpha) \tag{4.34}$$

$$\Delta \dot{z}_r = dnc\cos(nct+\alpha) \tag{4.35}$$

where n and c are the constants described by the equations (4.5) and (4.7).

4.2.2 In-track Formation

In the case of the in-track formation, both spacecraft share the same groundtrack by slightly different orbital planes separated by right ascension of the ascending node, which accounts for the Earth's rotation. The repeated groundtrack permits temporal measurements to be made faster than in the case of a single spacecraft mission. The initial conditions for this type of formation are given by Sabol et al. (2001) and are presented here:

$$\Delta x_0 = 0 \tag{4.36}$$

$$\Delta y_0 \tag{4.37}$$

$$\Delta z_0 = -(\omega_E/nc)\Delta y_0 \sin i_0 \tag{4.38}$$

$$\Delta \dot{z}_0 = 0 \tag{4.39}$$

where the desired separation between the two spacecraft in the in-track direction, Δy_0, is determined from operational constraints. In addition, equation (4.18) specifies the initial condition for $\Delta \dot{y}_0$. However, the initial condition for $\Delta \dot{x}_0$ is set to zero in order to maintain a constant offset in-track position between the two spacecraft.

The reference unperturbed formation is described by the following equations, which are taken from Sabol et al. (2001):

$$\Delta x_r = 0 \tag{4.40}$$

$$\Delta y_r = \Delta y_0 \tag{4.41}$$

$$\Delta z_r = -\left(\omega_E / nc\right) \Delta y_0 \sin i_0 \cos\left(nct\right) \tag{4.42}$$

$$\Delta \dot{x}_r = 0 \tag{4.43}$$

$$\Delta \dot{y}_r = 0 \tag{4.44}$$

$$\Delta \dot{z}_r = \omega_E \Delta y_0 \sin i_0 \sin\left(nct\right) \tag{4.45}$$

Again, the constants n and c are determined by equations (4.5) and (4.7).

4.3 CONTROL SYSTEM

In this section, a linear quadratic regulator (LQR) feedback control system is developed in order to counteract the orbital perturbations and maintain formation geometry. The approach taken is similar to Vaddi and Vadali (2003); however, in this study, estimates of differential atmospheric drag perturbations acting on the deputy spacecraft are included in the controller in order to compensate for them. The relative motion between the two spacecraft can be derived by using the relation

$$\Delta \mathbf{r} = \mathbf{r}_{rel_{chaser}} - \mathbf{r}_{rel_{target}} \tag{4.46}$$

Furthermore, by using equations (4.2) to (4.4), the resulting equations of motion expressed in the Hill frame describing spacecraft relative motion are

$$\Delta \ddot{x} - \left(nc\right)\Delta \dot{y} - \left(5c^2 - 2\right) n^2 \Delta x = \Delta f_{Drag\,x} + u_x \tag{4.47}$$

$$\Delta \ddot{y} + 2\left(nc\right)\Delta \dot{x} = \Delta f_{Drag\,y} + u_y \tag{4.48}$$

$$\Delta\ddot{z} + q^2\Delta z = 2lq\cos\left(qt + \phi\right) + \Delta f_{Drag\,z} + u_z \tag{4.49}$$

Now, let us define

$$\Delta\mathbf{x} = \begin{bmatrix}\Delta x & \Delta y & \Delta z & \Delta\dot{x} & \Delta\dot{y} & \Delta\dot{z}\end{bmatrix}^T \tag{4.50}$$

such that the state space form of equations (4.47) to (4.49) becomes

$$\Delta\dot{\mathbf{x}} = \mathbf{A}\Delta\mathbf{x} + \mathbf{C} + \mathbf{B}\mathbf{u} \tag{4.51}$$

where matrix **C** represents the periodic and differential drag terms found on the right hand side of equations (4.47) to (4.49). In the present case, **B** is a 3x3 identity matrix.

The control thrusts, **u**, are given by

$$\mathbf{u} = \begin{bmatrix}u_x & u_y & u_z\end{bmatrix}^T \tag{4.52}$$

and are determined by the relation

$$\mathbf{u} = \mathbf{K}\mathbf{e} - \Delta\mathbf{d}_{Drag} \tag{4.53}$$

where **K** is a control gain matrix, $\Delta\mathbf{d}_{Drag}$ are the estimates of the differential atmospheric drag perturbations acting on the deputy spacecraft, and the state error, **e**, is defined as

$$\mathbf{e} = \Delta\mathbf{x} - \Delta\mathbf{x}_r \tag{4.54}$$

In equation (4.54), $\Delta\mathbf{x}_r$ are the states corresponding to the formation's reference unperturbed trajectory as explained in section 4.2. Also, the estimates of the differential atmospheric drag perturbations are modeled from the same equations presented in section

4.1.1 but are differentiated as follows in order to cancel out those of equations (4.47) to (4.49):

$$\Delta \mathbf{d}_{Drag} = \mathbf{d}_{Drag_{chaser}} - \mathbf{d}_{Drag_{target}} \tag{4.55}$$

Replacing the corresponding terms of equations (4.47) to (4.49) in equation (4.51) gives the following matrices:

$$\mathbf{A} = \begin{bmatrix} 0 & 0 & 0 & 1 & 0 & 0 \\ 0 & 0 & 0 & 0 & 1 & 0 \\ 0 & 0 & 0 & 0 & 0 & 1 \\ \left(5c^2 - 2\right)n^2 & 0 & 0 & 0 & nc & 0 \\ 0 & 0 & 0 & -2nc & 0 & 0 \\ 0 & 0 & -q^2 & 0 & 0 & 0 \end{bmatrix} \tag{4.56}$$

$$\mathbf{C} = \begin{bmatrix} 0 \\ 0 \\ 0 \\ \Delta f_{Drag\,x} \\ \Delta f_{Drag\,y} \\ 2lq\cos\left(qt + \phi\right) + \Delta f_{Drag\,z} \end{bmatrix} \tag{4.57}$$

and

$$\mathbf{B} = \begin{bmatrix} 0 & 0 & 0 \\ 0 & 0 & 0 \\ 0 & 0 & 0 \\ 1 & 0 & 0 \\ 0 & 1 & 0 \\ 0 & 0 & 1 \end{bmatrix} \tag{4.58}$$

Now, a linear quadratic regulator (LQR) controller is designed by ignoring the periodic term and differential drag terms, **C**, in equation (4.51). The gain matrix **K** is designed with a positive definite choice of **Q** and **R** similar to those described in Vaddi and Vadali (2003).

The cost function to be minimized is chosen as

$$J = \lim_{t \to \infty} \int_0^t \left(\mathbf{e}^T \mathbf{Q} \mathbf{e} + \mathbf{u}^T \mathbf{R} \mathbf{u} \right) dt \tag{4.59}$$

where the corresponding **Q** and **R** matrices are similar to those from Vaddi and Vadali (2003); however they are modified for the period of the reference orbit used in this study and are given as follows:

$$\mathbf{Q} = \begin{bmatrix} 0.1 & 0 & 0 & 0 & 0 & 0 \\ 0 & 1 & 0 & 0 & 0 & 0 \\ 0 & 0 & 0.1 & 0 & 0 & 0 \\ 0 & 0 & 0 & 1/(nc)^2 & 0 & 0 \\ 0 & 0 & 0 & 0 & 1/(nc)^2 & 0 \\ 0 & 0 & 0 & 0 & 0 & 1/(nc)^2 \end{bmatrix} \tag{4.60}$$

and

$$\mathbf{R} = \begin{bmatrix} \dfrac{w}{(nc)^4} & 0 & 0 \\ 0 & \dfrac{1}{(nc)^4} & 0 \\ 0 & 0 & \dfrac{1}{(nc)^4} \end{bmatrix} \tag{4.61}$$

where w is a specified control weight.

The control gain matrix **K** is determined from MATLAB's *lqr* function and depends on the specified control weight, w. For a control weight of w = 1000, the resulting control gain is

$$\mathbf{K} = \begin{bmatrix} 0 & 0 & 0 & 0.0038 & 0 & 0 \\ 0 & 0 & 0 & 0.0019 & 0.0019 & 0 \\ 0 & 0 & 0 & 0 & 0 & 0.0015 \end{bmatrix} \tag{4.62}$$

With the values of the control gain matrix, **K**, known, a closed loop controller can be implemented into the formation flying SIMULINK simulator. For each of the formation schemes simulated in the next chapter, the control gain matrix, **K**, is specified as shown by equation (4.62); thus, the controller is not tuned for each particular scenario.

4.4 FORMATION FLYING SIMULINK SIMULATOR

In this section, a short description of the numerical implementation regarding the formation flying SIMULINK simulator is presented. In the formation flying SIMULINK simulator, there are 6 first order differential equations that are being integrated, hence those in section 4.1, while those in section 4.3 are only integrated when they are needed (i.e. when the controller is turn on). The integration in SIMULINK was done using the fourth-order Runge Kutta method. The time step was fixed at sixty seconds and each simulation usually took approximately twenty minutes to complete on a desktop computer, such that the simulations are not relatively numerically intense. The simulator was validated by comparing results with those obtained from AGI's Satellite Tool Kit (STK) software for various formation flying scenarios.

To conclude, the formulation for formation flying analyses has been presented in this chapter along with the initial conditions for selected formations and the equations describing the linear quadratic regulator (LQR) control system implemented to maintain formation geometry. The next chapter will present simulation results for various formations schemes.

CHAPTER 5 - TECSAS FORMATION FLYING

Simulation results pertaining to several TECSAS formation flying scenarios are the subject of this chapter. Four formation flying scenarios are studied: the TECSAS-TECSAS projected circular formation, the Quicksat-TECSAS projected circular formation, the TECSAS-TECSAS in-track formation, and the Quicksat-TECSAS in-track formation. The names of the formations are determined as follows: the first name is the chief spacecraft, while the second represents the deputy spacecraft. Thus each spacecraft formation has two variations, one where both spacecraft are identical (TECSAS-TECSAS formations), and the other, where the chief spacecraft is the Canadian Space Agency's (CSA) Quicksat spacecraft, while the deputy spacecraft remains the TECSAS spacecraft (Quicksat-TECSAS formations). As was the case in chapter 3, both spacecraft are expected to maintain a constant attitude while in formation flight mode such that their orientation dynamics are neglected in this study.

The chapter is divided into four main sections. First, simulation results for the TECSAS-TECSAS projected circular formation are presented. This is followed by simulation results for the Quicksat-TECSAS projected circular formation. The third section presents simulation results for the TECSAS-TECSAS in-track formation, while the fourth and final section deals with simulation results for the Quicksat-TECSAS in-track formation. Each of these four sections is divided into subsections where the effects of the J_2 and atmospheric drag perturbations are studied for each formation. Furthermore, an additional subsection is presented for each spacecraft formation where simulation results are presented regarding the implementation of a linear quadratic regulator (LQR) control system in order to maintain formation geometry.

5.1 TECSAS-TECSAS PROJECTED CIRCULAR FORMATION

The first spacecraft formation to be studied in this thesis is the TECSAS-TECSAS projected circular formation. This type of formation is useful for Earth observation missions because the inter-spacecraft distance is maintained constant in the cross-track/in-track plane. In this section, both spacecraft are assumed to be TECSAS-type spacecraft and have the following characteristics as shown in Table 5.1.

Table 5.1: TECSAS Spacecraft Characteristics

Parameter	TECSAS deputy and chief spacecraft
Mass (m)	175 kg
Cross-sectional area (A)	2.22 m^2
Drag coefficient (C_D)	2.3
Ballistic coefficient (m/C_DA)	34.27 kg/m^2

For this study, a formation diameter of 100 m was desired. The corresponding initial conditions are found as discussed in section 4.2.1 and are given in Table 5.2.

Table 5.2: Projected Circular Formation Initial Conditions

Δx_0	Δy_0	Δz_0	$\Delta \dot{x}_0$	$\Delta \dot{y}_0$	$\Delta \dot{z}_0$
35.35 m	70.71 m	70.71 m	0.039 m/s	5.014 m/s	0.078 m/s

5.1.1 TECSAS-TECSAS Projected Circular Formation - Unperturbed

In order to study the effects of the J_2 and the atmospheric drag perturbations on the TECSAS-TECSAS projected circular formation, the unperturbed motion is shown for comparison purposes in Figures 5.1 to 5.4.

Without any orbital perturbations acting on the projected circular formation studied here, the projection of the relative motion in the radial/in-track plane is an ellipse with a 50 m semi-minor axis in the radial direction and a 100 m semi-major axis in the in-track direction as can be seen from Figure 5.2. From Figure 5.3, it can be seen that the projection of the unperturbed relative motion in the cross-track/radial plane is an inclined line. Finally, the projection of the unperturbed relative motion in the cross-track/in-track plane is a 100 m circle as seen from Figure 5.4.

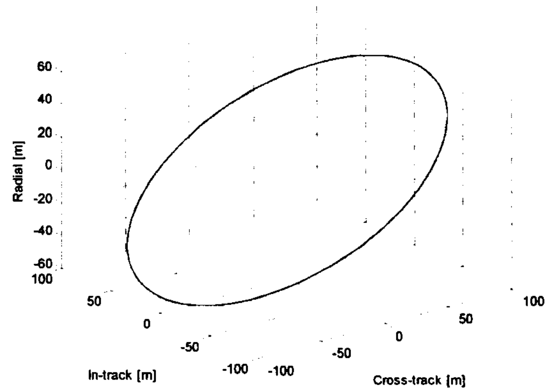

Figure 5.1: TECSAS-TECSAS Projected Circular Formation - Unperturbed.

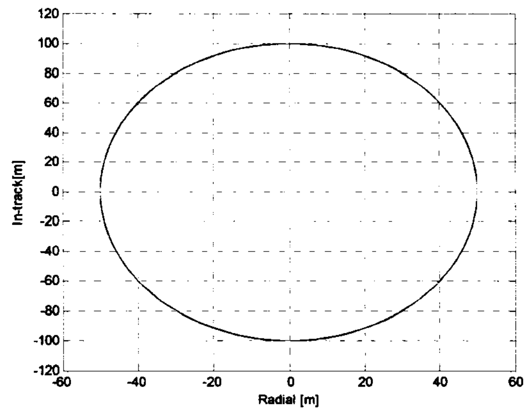

Figure 5.2: TECSAS-TECSAS Projected Circular Formation - Unperturbed - xy Plane Projection.

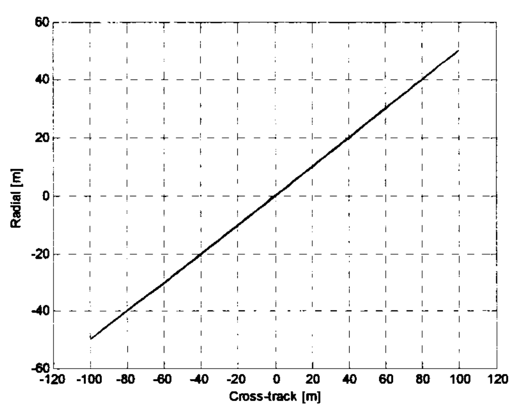

Figure 5.3: TECSAS-TECSAS Projected Circular Formation - Unperturbed - zx Plane Projection.

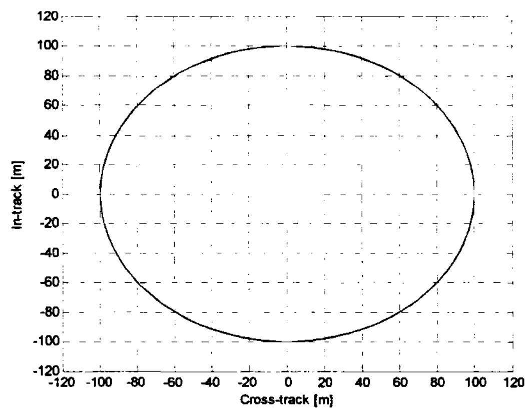

Figure 5.4: TECSAS-TECSAS Projected Circular Formation - Unperturbed - zy Plane Projection.

In the following subsections, the effects of the J_2 and the atmospheric drag perturbations on the TECSAS-TECSAS projected circular formation are determined.

5.1.2 TECSAS-TECSAS Projected Circular Formation - J_2 Perturbations

The following figures show how the TECSAS-TECSAS projected circular formation is affected by the J_2 perturbations over the case of 1 day, 1 week, and 4 weeks of simulation time.

1-Day Simulation

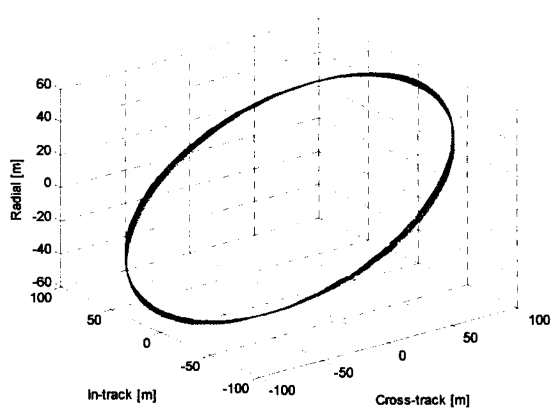

Figure 5.5: TECSAS-TECSAS Projected Circular Formation - J_2 Perturbations - 1 Day Simulation.

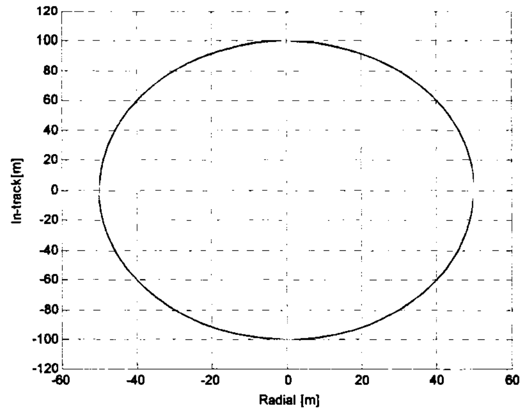

Figure 5.6: TECSAS-TECSAS Projected Circular Formation - J_2 Perturbations - 1 Day Simulation - xy Plane Projection.

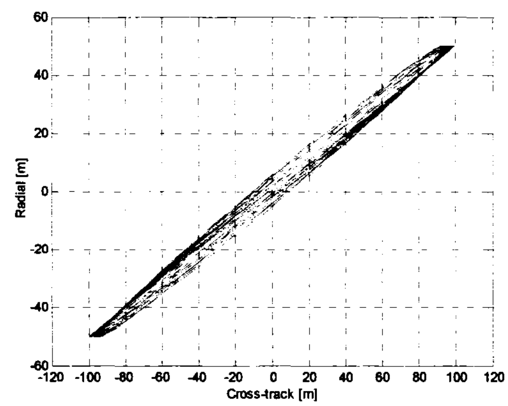

Figure 5.7: TECSAS-TECSAS Projected Circular Formation - J_2 Perturbations - 1 Day Simulation - zx Plane Projection.

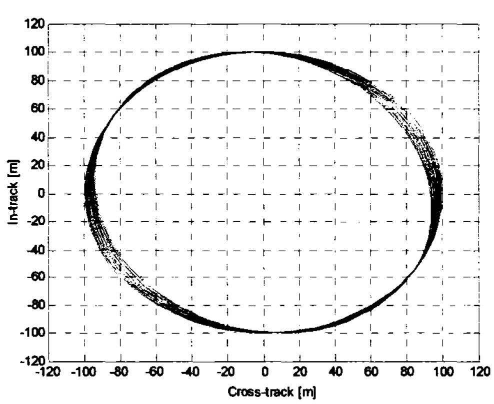

Figure 5.8: TECSAS-TECSAS Projected Circular Formation - J_2 Perturbations - 1 Day Simulation - zy Plane Projection.

Figure 5.5 provides a three dimensional view of the TECSAS-TECSAS projected circular formation after 1 day of simulation time. From Figure 5.6, we can see that the projection of the formation in the radial/in-track plane is an ellipse and that this plane is not noticeably affected by the J_2 perturbations. Some perturbative effects due to the J_2 perturbations can be seen in Figures 5.7 and 5.8, in which the formation geometry starts to degrade from the unperturbed case. In Figure 5.7, it can be seen that a diagonal line, in which the thickening represents the perturbative motion caused by the J_2 perturbations, represents the projected motion into the cross-track/radial plane. Furthermore, from Figure 5.8, it can be seen that even after one day of simulation time, the J_2 perturbations cause the projected motion onto the cross-track/in-track plane, which is nominally represented by a circle, to degrade by approximately 10 m along its edges.

1-Week Simulation

After one week of simulation time, the orbital perturbations cause the TECSAS-TECSAS projected circular formation to degrade significantly as can be seen in Figure 5.9. As was the case for the 1-day simulation, the projected motion in the radial/in-track plane is not affected by the J_2 perturbations, as shown in Figure 5.10. In Figure 5.11, it can be seen that the perturbations cause the cross-track motion to expand significantly (approximately 70 m of deviation) compared to the case of the 1-day simulation (see Figure 5.3). Finally, Figure 5.12 shows the projected motion in the cross-track/in-track plane, in which the J_2 perturbations cause the formation geometry to close upon itself.

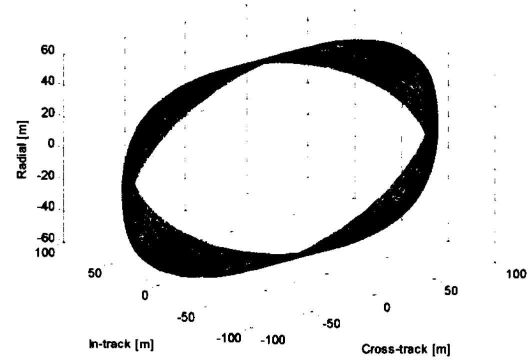

Figure 5.9: TECSAS-TECSAS Projected Circular Formation - J_2 Perturbations - 1 Week Simulation.

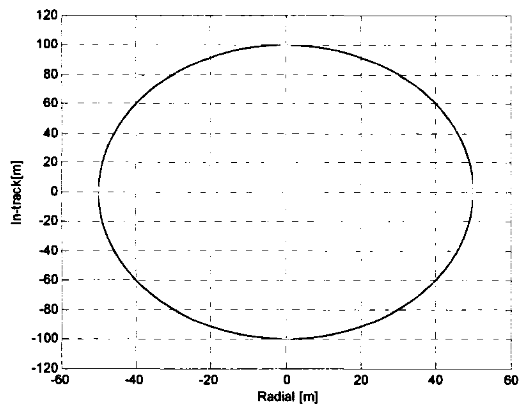

Figure 5.10: TECSAS-TECSAS Projected Circular Formation - J_2 Perturbations - 1 Week Simulation - xy Plane Projection.

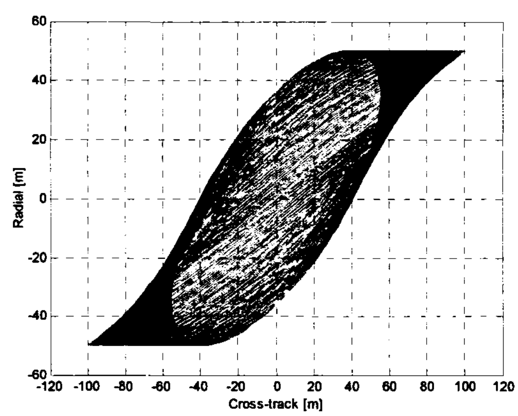

Figure 5.11: TECSAS-TECSAS Projected Circular Formation - J_2 Perturbations - 1 Week Simulation - zx Plane Projection.

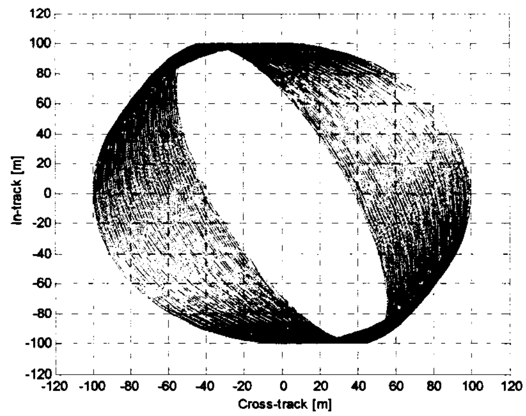

Figure 5.12: TECSAS-TECSAS Projected Circular Formation - J_2 Perturbations - 1 Week Simulation - zy Plane Projection.

4 Weeks Simulation

Figures 5.13 to 5.16 show how the projected circular formation is affected by the J_2 perturbations over 4 weeks. In Figure 5.13, the J_2-induced tumbling effect first noticed by Schweighart and Sedwick (2002) is clearly identified. This tumbling effect acts on the formation as a whole and rotates it around the cross-track axis. Furthermore, the tumbling effect explains the formation degradation as can be seen in Figure 5.16, where the relative motion covers a complete semi-circular area as if the formation of Figure 5.4 is rotated from an imaginary axis, which, in this case, is inclined by approximately 31° from the cross-track axis.

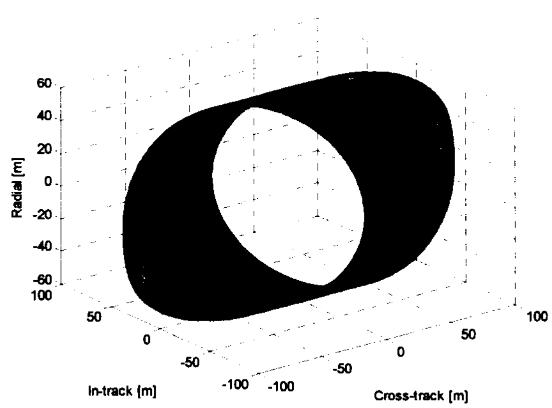

Figure 5.13: TECSAS-TECSAS Projected Circular Formation - J_2 Perturbations - 4 Weeks Simulation.

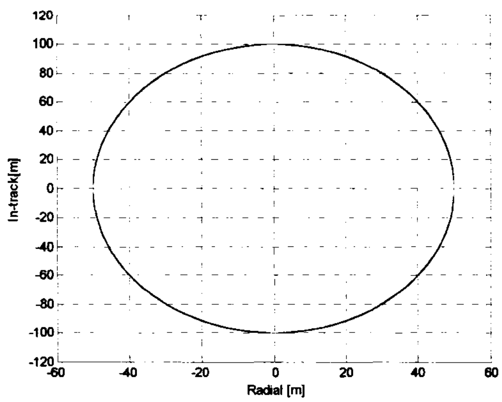

Figure 5.14: TECSAS-TECSAS Projected Circular Formation - J_2 Perturbations - 4 Weeks Simulation - xy Plane Projection.

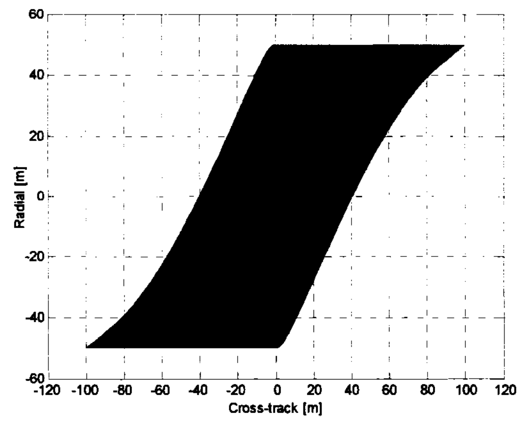

Figure 5.15: TECSAS-TECSAS Projected Circular Formation - J_2 Perturbations - 4 Weeks Simulation - zx Plane Projection.

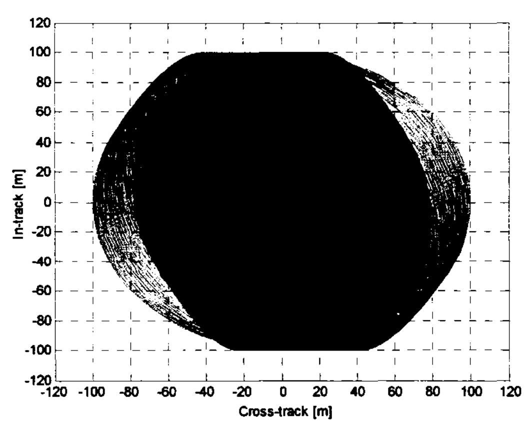

Figure 5.16: TECSAS-TECSAS Projected Circular Formation - J_2 Perturbations - 4 Weeks Simulation - zy Plane Projection.

In conclusion, the J_2 perturbations greatly affect the formation geometry of the TECSAS-TECSAS projected circular formation even, as was demonstrated, over the course of a very short time span. If mission specifications allow less than 10% baseline deviations, then corrective control impulses are needed to maintain formation geometry even after one day of operation. This leads to costly fuel consumptions for such missions and shall be further discussed in section 5.1.4. In the next section, atmospheric drag perturbations are added to study its effects on the formation geometry.

5.1.3 TECSAS-TECSAS Projected Circular Formation - J_2 and Atmospheric Drag Perturbations

The following figures show simulation results for the TECSAS-TECSAS projected circular formation with J_2 and atmospheric drag perturbations acting on the formation over the case of 1 day and 4 weeks of simulation time. The goal of this subsection is to identify the effects on the TECSAS-TECSAS projected circular formation due to differential atmospheric drag perturbations acting on the spacecraft in the formation.

1-Day Simulation

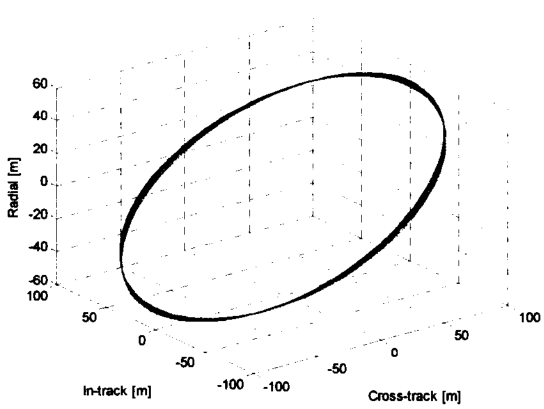

Figure 5.17: TECSAS-TECSAS Projected Circular Formation - J_2 and Atmospheric Drag Perturbations - 1 Day Simulation.

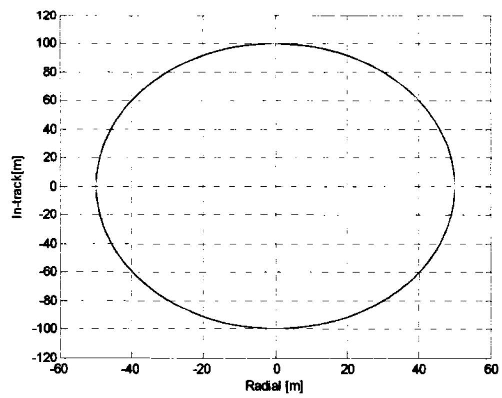

Figure 5.18: TECSAS-TECSAS Projected Circular Formation - J_2 and Atmospheric Drag Perturbations - 1 Day Simulation - xy Plane Projection.

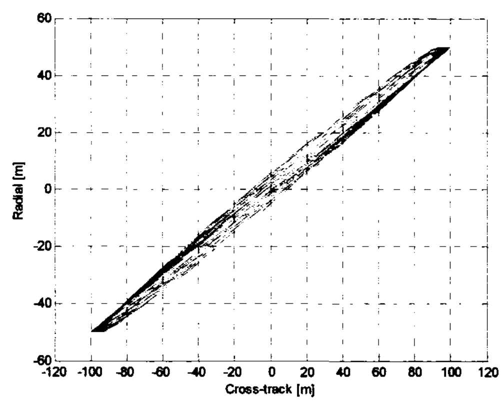

Figure 5.19: TECSAS-TECSAS Projected Circular Formation - J_2 and Atmospheric Drag Perturbations - 1 Day Simulation - xy Plane Projection.

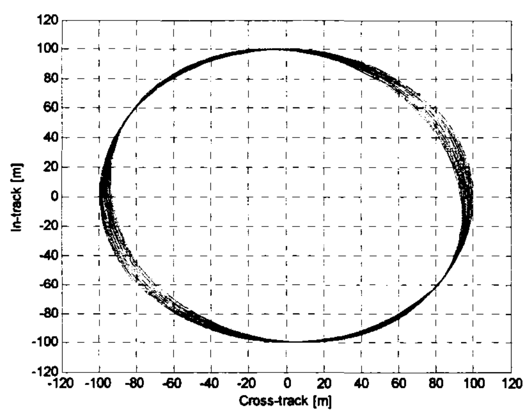

Figure 5.20: TECSAS-TECSAS Projected Circular Formation - J_2 and Atmospheric Drag Perturbations - 1 Day Simulation - zy Plane Projection.

Comparing Figures 5.17, 5.18, 5.19, and 5.20 to those of the TECSAS-TECSAS projected circular formation subjected to only J_2 perturbations (Figures 5.5 to 5.8) shows that over the case of one day, effects of differential atmospheric drag perturbations are negligible when both spacecraft are identical. The fact that the differential atmospheric drag perturbations are negligible over a short time span is related to the fact that these perturbations are smaller in magnitude than the J_2 perturbations at the altitude considered; the latter as we have seen in the previous subsection, alter the formation geometry even after such a short time span.

4 Weeks Simulation

By comparing Figures 5.21, 5.22, 5.23, and 5.24 to those of the section 5.1.2 (Figures 5.13 to 5.16), it is evident that differential atmospheric drag perturbations alter the formation geometry, especially in the in-track direction. Figure 5.22 shows that after 4 weeks, there is a 15 m drift in the in-track direction due to differential atmospheric drag perturbations acting on the deputy with respect to the chief spacecraft, which is not present in Figure 5.14. The same drift causes further geometry deviations as can be seen in Figure 5.24. Because both spacecraft have identical ballistic coefficients, differential atmospheric drag perturbations are caused by the Earth's oblateness, which affects the relative altitude between spacecraft. Thus, each spacecraft sees a different atmospheric density, which induces differential drag perturbations on the deputy with respect to the chief spacecraft.

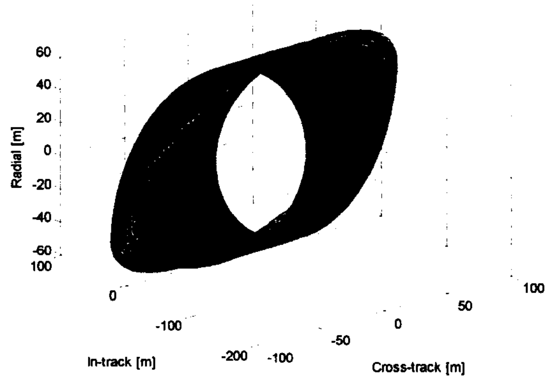

Figure 5.21: TECSAS-TECSAS Projected Circular Formation - J_2 and Atmospheric Drag Perturbations - 4 Weeks Simulation.

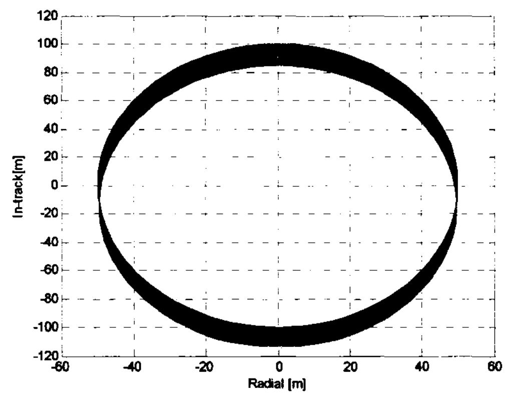

Figure 5.22: TECSAS-TECSAS Projected Circular Formation - J_2 and Atmospheric Drag Perturbations - 4 Weeks Simulation - xy Plane Projection.

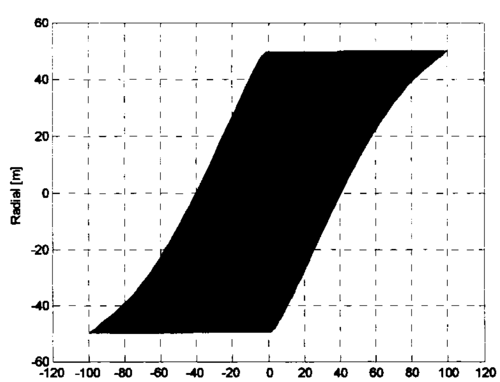

Figure 5.23: TECSAS-TECSAS Projected Circular Formation - J_2 and Atmospheric Drag Perturbations - 4 Weeks Simulation - zx Plane Projection.

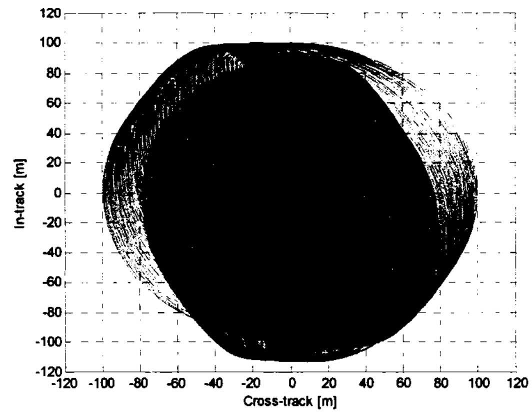

Figure 5.24: TECSAS-TECSAS Projected Circular Formation - J_2 and Atmospheric Drag Perturbations - 4 Weeks Simulation - zy Plane Projection.

As shown in this section, differential atmospheric drag perturbations can occur even when both spacecraft are assumed to be identical. This leads to the next subsection, which deals with simulation results of the TECSAS-TECSAS projected circular formation with the addition of a LQR controller in order to maintain formation geometry.

5.1.4 TECSAS-TECSAS Projected Circular Formation - J_2 and Atmospheric Drag Perturbations and LQR Controller Inputs

In this subsection, a linear quadratic regulator (LQR) controller as described in section 4.3, is added in order to maintain the formation geometry.

The following figures present simulation results in which the TECSAS-TECSAS projected circular formation is subjected to J_2 and atmospheric drag perturbations and formation control forces are used to counteract the orbital perturbations acting on the formation. The control gain matrix, **K**, is specified as shown by equation (4.62) with the associated control weight being $w = 1000$.

1-Day Simulation

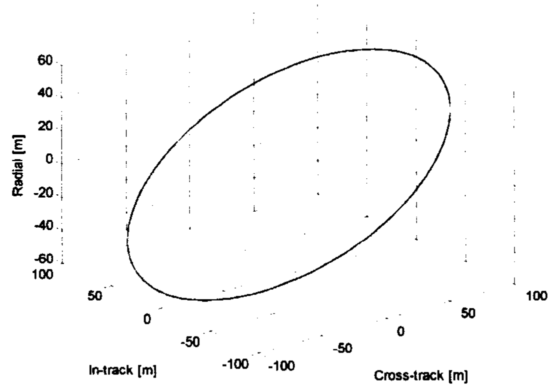

Figure 5.25: TECSAS-TECSAS Projected Circular Formation - J_2 and Atmospheric Drag Perturbations and Control Forces - 1 Day Simulation.

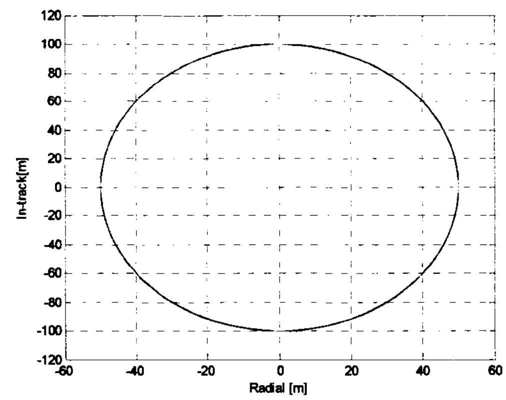

Figure 5.26: TECSAS-TECSAS Projected Circular Formation - J_2 and Atmospheric Drag Perturbations and Control Forces - 1 Day Simulation - xy Plane Projection.

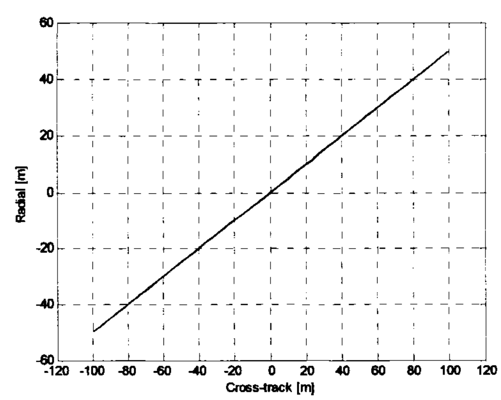

Figure 5.27: TECSAS-TECSAS Projected Circular Formation - J_2 and Atmospheric Drag Perturbations and Control Forces - 1 Day Simulation - zx Plane Projection.

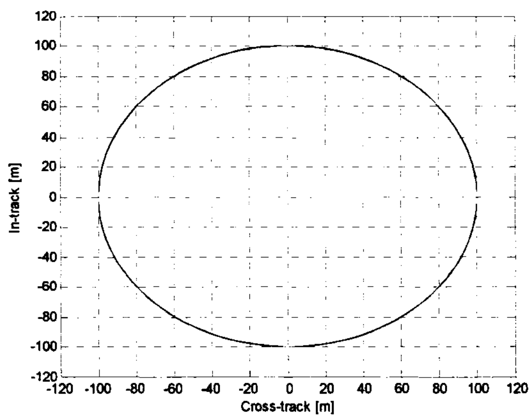

Figure 5.28: TECSAS-TECSAS Projected Circular Formation - J_2 and Atmospheric Drag Perturbations and Control Forces - 1 Day Simulation - zy Plane Projection.

As can be seen from Figures 5.25 to 5.28, the linear quadratic regulator (LQR) controller is successful in maintaining formation geometry over a short time span because the resulting relative motion is identical to the unperturbed case as was described earlier in section 5.1.1. The control forces are thus adequate in counteracting the orbital perturbations acting on the formation. The controller works fine for longer time spans as well, but the results are not shown here for brevity.

The following figures, Figure 5.29 and 5.30, show the control force variations as a function of number of orbits for 1-day and 4-week time spans, respectively. From Figure 5.29, it can be seen that the control forces vary periodically over an orbit. Also, the cross-track control force (u_z) magnitudes are greater than the other three components. The cross-track control force oscillates between ±0.038 mN and they are more than twice the magnitude of the radial control force (u_x), which oscillates between ±0.015 mN. The in-track control force (u_y), which has the lowest magnitudes (±0.004 mN), is approximately four times less than the radial control force. In addition, the in-track and cross-track control inputs seem to be in phase with each other, while the radial control force is phased at half a period, or orbit, later.

1-Day Simulation

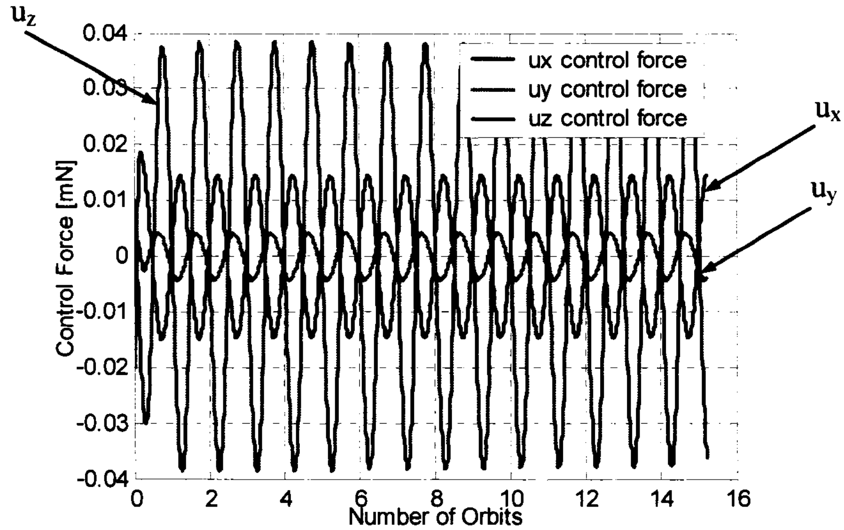

Figure 5.29: TECSAS-TECSAS Projected Circular Formation - J_2 and Atmospheric Drag Perturbations and Control Forces - 1 Day Simulation - Control Forces.

Figure 5.30 shows the variations in control forces over a time span of 4 weeks. It seems that the cross-track control force (u_z) declines over time; however, further simulations show that this is a periodic effect, which coincides with the J_2-induced tumbling effect on the formation. In addition, it is possible to estimate the period of the tumbling effect based on the magnitude of the cross-track control forces. The half period of the tumbling effect corresponds to approximately 410 orbits, when the cross-track control input magnitudes are at their lowest values and start to increase again. Thus, it can be approximated that, for this particular scenario, the tumbling effect has a period of around 820 orbits or approximately 55 days. In contrary to the cross-track control input, the other two control inputs, the radial and in-track control inputs, (u_x) and (u_y), follow their constant periodic behaviour as described previously.

4 Weeks Simulation

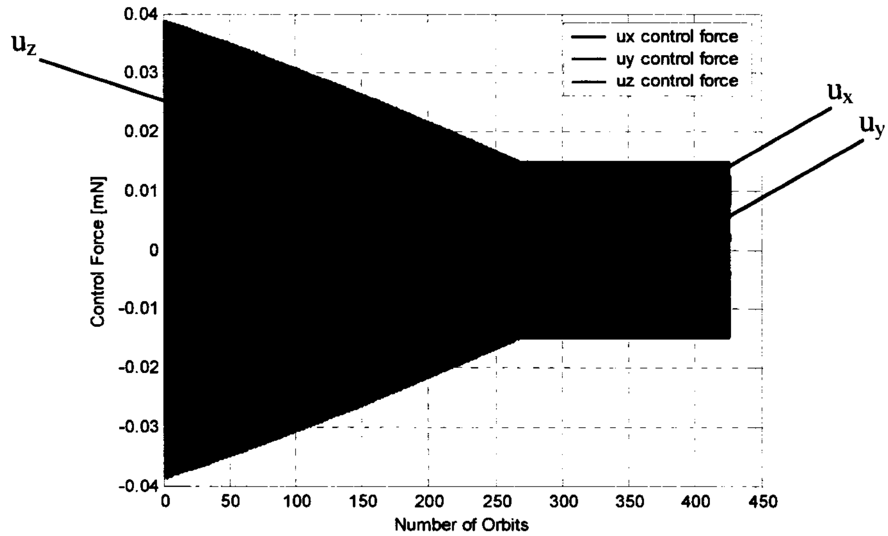

Figure 5.30: TECSAS-TECSAS Projected Circular Formation - J_2 and Atmospheric Drag Perturbations and Control Forces - 4 Weeks Simulation - Control Forces.

Table 5.3: LQR Controller Impulse Requirements for 1-Day and 4-Week Time Spans for TECSAS-TECSAS Projected Circular Formation Flying Scenario

	1 day	4 weeks
Radial control impulse	0.815 Ns	22.693 Ns
In-track control impulse	0.234 Ns	6.441 Ns
Cross-track control impulse	2.077 Ns	30.826 Ns
Total control impulse	**3.126 Ns**	**59.960 Ns**

Table 5.3 gives the total control impulse requirements for each component and for both time spans. The total control impulse requirement for 1 day is 3.126 Ns, while the total control impulse requirement for 4 weeks is 59.960 Ns. Because of the behaviour of the cross-track component, the resulting relationship of total impulse requirements with respect to time is not linear with respect to time as would be initially suspected. Also, the cross-track control impulse requirements are higher than the other two control impulse components. For the 1-day time span, the cross-track control impulse requires 2.077 Ns, while the radial control input demands 0.815 Ns and the in-track control input requires the least amount of impulse at 0.234 Ns. Furthermore, for the 4-week time span, the

cross-track control inputs demands 30.826 Ns of control impulse, while the other two components require 22.693 Ns and 6.441 Ns of control impulse for the radial and in-track components respectively. In the next section, the chief spacecraft is replaced with the Quicksat spacecraft in a similar projected circular formation.

5.2 QUICKSAT-TECSAS PROJECTED CIRCULAR FORMATION

In this section, simulation results are given for the Quicksat-TECSAS projected circular formation scenario. Because of its possible use in the TECSAS mission, the chief spacecraft is thus replaced by the Canadian Space Agency's (CSA) Quicksat spacecraft. The Quicksat spacecraft, shown in Figure 5.31, is a small-sat, which is being developed in-house at the Canadian Space Agency, and should be ready for launch and mission operations by the end of 2005. Currently, there is no specific mission plan for the Quicksat spacecraft; however, it is being considered as a possible candidate for use as the chief spacecraft in the TECSAS mission. The spacecraft's characteristics are given in Table 5.4.

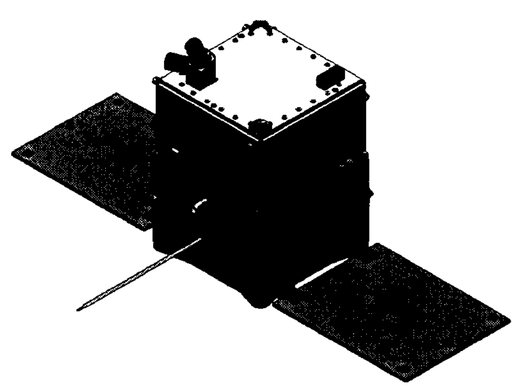

Figure 5.31: Quicksat Chief Spacecraft [Courtesy of the Canadian Space Agency].

Table 5.4: Quicksat Spacecraft Characteristics

Parameter	Quicksat chief spacecraft
Mass (m)	93 kg
Cross-sectional area (A)	0.30 m^2
Drag coefficient (C_D)	2.3
Ballistic coefficient (m/C_DA)	134.0 kg/m^2

In the following subsections, simulations results are shown in order to study the differential atmospheric drag perturbations resulting from the Quicksat-TECSAS projected circular formation scenario. Furthermore, simulation results are given in which a linear quadratic regulator (LQR) controller is used to maintain formation geometry and the variations with regards to the TECSAS-TECSAS projected circular formation case are examined.

5.2.1 Quicksat-TECSAS Projected Circular Formation - J_2 and Atmospheric Drag Perturbations

In this subsection, the Quicksat-TECSAS projected circular formation is subjected to both J_2 and atmospheric drag perturbations in order to study the differential drag effects on the formation. If there were only J_2 perturbations, results would be the same as shown in Figures 5.5 to 5.16. However, atmospheric drag alters the results significantly: simulations are only carried out for a time span of 1 day because significant in-track drift occurs, which breaks up the formation even after such a short time span.

1-Day Simulation

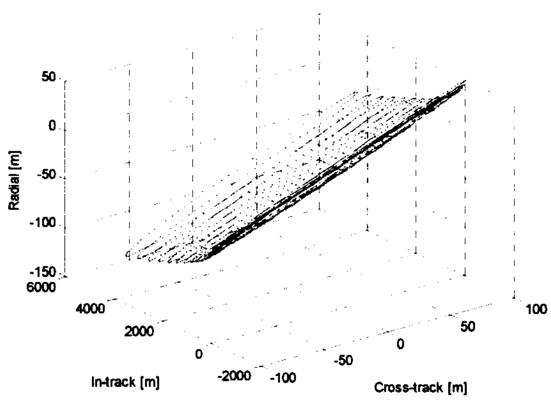

Figure 5.32: Quicksat-TECSAS Projected Circular Formation - J_2 and Atmospheric Drag Perturbations - 1 Day Simulation.

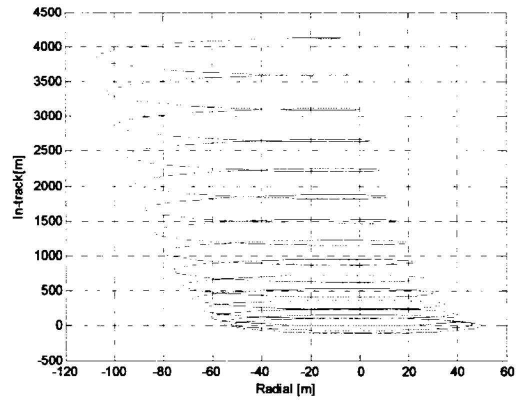

Figure 5.33: Quicksat-TECSAS Projected Circular Formation - J_2 and Atmospheric Drag Perturbations - 1 Day Simulation - xy Plane Projection.

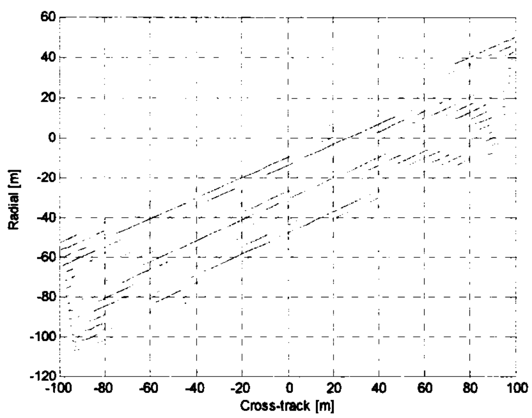

Figure 5.34: Quicksat-TECSAS Projected Circular Formation - J_2 and Atmospheric Drag Perturbations - 1 Day Simulation - zx Plane Projection.

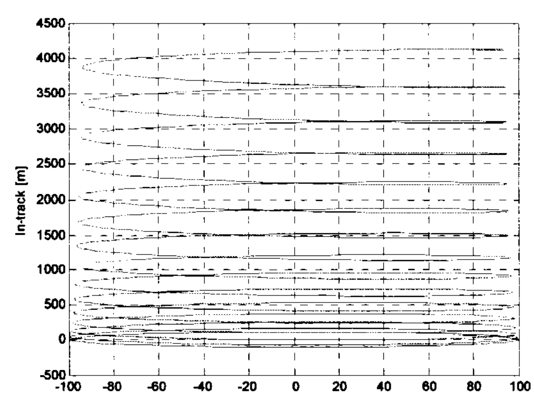

Figure 5.35: Quicksat-TECSAS Projected Circular Formation - J_2 and Atmospheric Drag Perturbations - 1 Day Simulation - zy Plane Projection.

By comparing Figures 5.32, 5.33, 5.34, and 5.35 to those of the TECSAS-TECSAS projected circular scenario of section 5.1.3 (Figures 5.17 to 5.20), it can be seen that there is significant drift in the in-track direction that results from the differential atmospheric drag perturbations acting on the deputy (TECSAS) with respect to the chief (Quicksat) spacecraft. After a 1-day time span, the in-track drift is approximately 4 km, and there is also a 50 m drift occurring in the radial direction. Since the TECSAS spacecraft has a lower ballistic coefficient than the Quicksat spacecraft, the atmospheric drag perturbations acting on the former are stronger than those acting on the chief spacecraft and thus differential atmospheric drag perturbations occur. The results of the differential atmospheric drag perturbations acting on the deputy spacecraft are that its orbit is decaying at a faster rate than the chief's orbit and thus, radial separation between both spacecraft occurs. Finally, since the deputy's orbital altitude is decreasing, its orbital rate increases and thus, relative drift between both spacecraft in the in-track direction occurs.

In the next subsection, a linear quadratic regulator (LQR) controller is used in order to counteract these orbital perturbations and maintain formation geometry.

5.2.2 Quicksat-TECSAS Projected Circular Formation - J_2 and Drag Perturbations and Control Inputs

As mentioned in the previous subsection, orbital drift due to differential atmospheric drag perturbations causes the Quicksat-TECSAS projected circular formation geometry to break up even in a short time span. The need for formation-keeping control forces is apparent from the figures of the previous subsection. In this subsection, simulation results are shown for the case of the Quicksat-TECSAS projected circular formation utilising a LQR controller to generate formation keeping control forces. As was the case in section 5.1.4, the control gain matrix, **K**, is specified as shown by equation (4.62) with the associated control weight being $w = 1000$.

1-Day Simulation

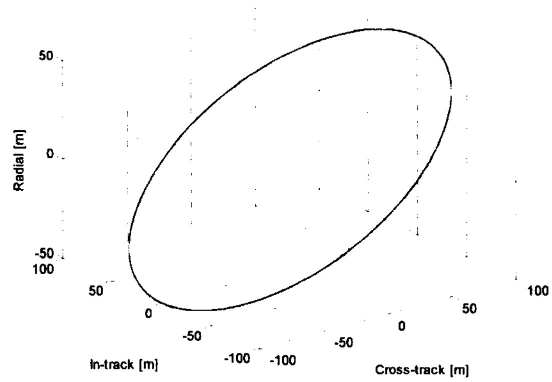

Figure 5.36: Quicksat-TECSAS Projected Circular Formation - J_2 and Drag Perturbations and Control Forces - 1 Day Simulation.

From Figure 5.36, it can be seen that the formation keeping control forces are adequate for the Quicksat-TECSAS projected circular formation scenario because both the orbital in-track drift and the orbital J_2 perturbations do not affect the formation geometry for short time spans. For longer simulation time spans also the results are similar and are not shown here to avoid repetitiveness.

The following figures, Figures 5.37 and 5.38, represent the control forces versus orbit count in order to view the variations in the individual control force components for both time spans of 1 day and 4 weeks.

From Figure 5.37, it can be seen that the in-track control force (u_y) oscillates around a fixed non-zero value of approximately 0.067 mN, which is contrary to the TECSAS-TECSAS projected circular formation scenario. This fixed in-track control force is due to the differential atmospheric drag perturbations acting on the deputy spacecraft as described in the previous subsection. Also, the in-track control input is made up of two periodic components instead of one, as is the case for the other control inputs. However, like the identical spacecraft scenario, in the Quicksat-TECSAS projected circular formation scenario, the cross-track control force (u_z), which oscillates between ±0.039 mN, is more important than the radial control force (u_x), oscillates between ±0.016 mN; this is due to differential J_2 perturbations acting on the deputy with respect to the deputy spacecraft.

1-Day Simulation

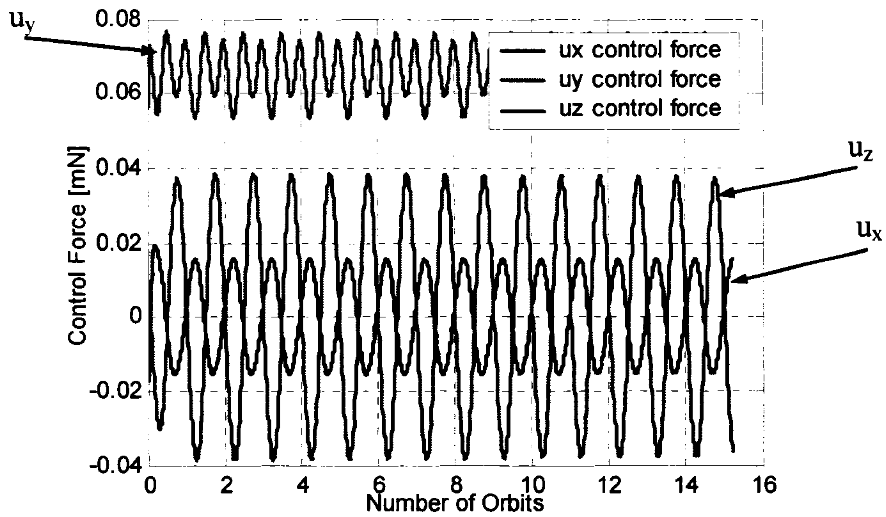

Figure 5.37: Quicksat-TECSAS Projected Circular Formation - J_2 and Atmospheric Drag Perturbations and Control Forces - 1 Day Simulation - Control Forces.

4 Weeks Simulation

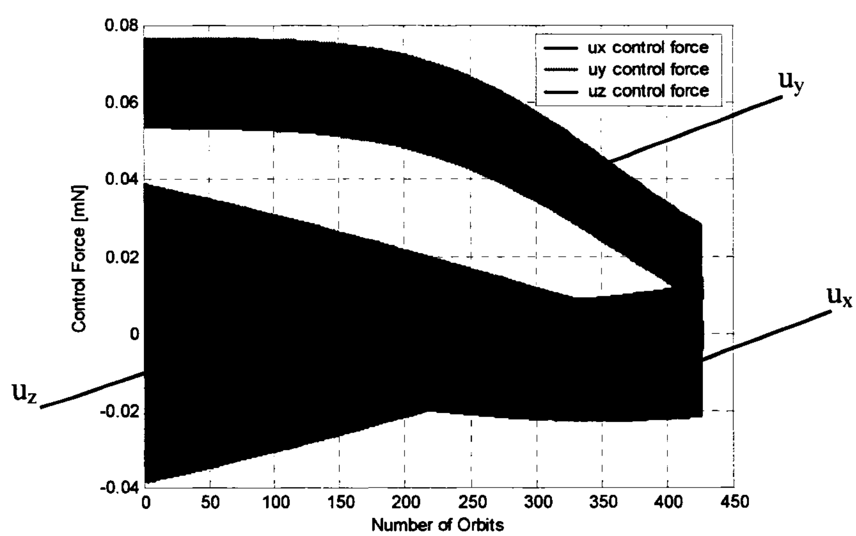

Figure 5.38: Quicksat-TECSAS Projected Circular Formation - J_2 and Atmospheric Drag Perturbations and Control Forces - 4 weeks simulation - Control Forces.

Figure 5.38 shows that over 4 weeks, the magnitude of the in-track control input (u_y) decreases, while the radial control force (u_x) continues to oscillate about the zero value. The cross-track control input (u_z) has the same form as in the TECSAS-TECSAS projected circular formation scenario (see section 5.1.4 for additional comments). A longer simulation time span (Figure 5.39) shows that after the in-track control input begins to oscillate between ±0.008 mN (at approximately 700 orbits or 46 days), it remains constant, while the other two control inputs continue to behave as described earlier in this subsection (not shown for clarity in Figure 5.39).

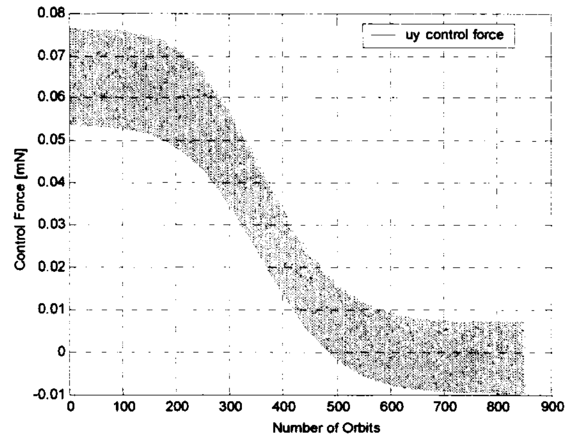

Figure 5.39: Quicksat-TECSAS Projected Circular Formation - J_2 and Atmospheric Drag Perturbations and Control Forces - 8 weeks simulation - In-track Control Force.

Furthermore, Table 5.5 gives the total control impulse requirements for each component and for both time spans for the TECSAS-Quicksat projected circular formation flying scenario. Comparing Table 5.3 to Table 5.5, it can be seen that the TECSAS-Quicksat scenario requires significantly more overall control impulse (8.593 Ns and 184.355 Ns for the 1-day and 4-week time spans respectively) than the TECSAS-TECSAS scenario (3.126 Ns and 59.960 Ns respectively) for both time spans. It is clear that the increase in control impulse requirements in the Quicksat-TECSAS projected circular formation flying scenario is due to stronger differential atmospheric drag perturbations than in the TECSAS-TECSAS formation flying scenario. Furthermore, the in-track control input, which counteracts the orbital drift in the Quicksat-TECSAS scenario, increases significantly from 0.234 Ns and 6.441 Ns in the TECSAS-TECSAS scenario to 5.653 Ns and 128.672 Ns in the Quicksat-TECSAS scenario for time spans of 1 day and 4 weeks respectively. The other two control inputs share similar values for either scenario because atmospheric drag induced orbital drift is not significant in these directions compared to the in-track drift.

Table 5.5: LQR Controller Impulse Requirements for 1 Day and 4 Weeks Time Spans for TECSAS-Quicksat Projected Circular Formation Flying Scenario

	1 day	4 weeks
Radial control impulse	0.863 Ns	24.857 Ns
In-track control impulse	5.653 Ns	128.672 Ns
Cross-track control impulse	2.077 Ns	30.826 Ns
Total control impulse	**8.593 Ns**	**184.355 Ns**

It is clear from this section that the differential atmospheric drag perturbations are greater when both spacecraft do not share the same ballistic coefficient and in comparison to the J_2 perturbations, these perturbations become the major source that disrupts the formation's geometry even after a short time span. Because the results show that significant amounts of control forces are necessary when both spacecraft are not identical, similar-sized spacecraft should strongly be considered depending on mission specifications. In the following section, simulation results from another spacecraft formation, the TECSAS-TECSAS in-track formation, are presented.

5.3 TECSAS-TECSAS IN-TRACK FORMATION

The second spacecraft formation to be studied in this thesis is the TECSAS-TECSAS in-track formation. This type of formation is also useful for Earth observation missions because both spacecraft share the same groundtrack. In this section, both spacecraft are assumed to be identical TECSAS-type spacecraft and have the characteristics as was mentioned in Table 5.1. Furthermore, for this study, an in-track spacing of 100 m was desired between the two spacecraft. The corresponding initial conditions are found as discussed in section 4.2.2 and are given in Table 5.6.

Table 5.6: In-track Formation Initial Conditions

Δx_0	Δy_0	Δz_0	$\Delta \dot{x}_0$	$\Delta \dot{y}_0$	$\Delta \dot{z}_0$
0.0 m	-100.0 m	6.45 m	0.0 m/s	5.093 m/s	0.0001 m/s

In order to study the effects of the J_2 and the atmospheric drag perturbations on the TECSAS-TECSAS in-track formation, the unperturbed motion is shown in the next subsection for comparison purposes.

5.3.1 TECSAS-TECSAS In-track Formation - Unperturbed

For the unperturbed case, the projection of the relative motion onto the radial/in-track plane is a point centered at the origin (Figure 5.41) while in the cross-track/radial plane, it is a straight-line varying from +6 m to -6 m as can be seen in Figure 5.40. Finally, Figure 5.43 shows the projection of relative motion in the cross-track/in-track plane, which is represented by a straight line located at -100 m in the in-track direction.

The in-track formation is stable under J_2 perturbations even over long time spans, because both spacecraft orbit very similar orbits. For this reason, no analysis pertaining to J_2 perturbations on this type of formation is needed and atmospheric drag perturbations are studied in the next subsection.

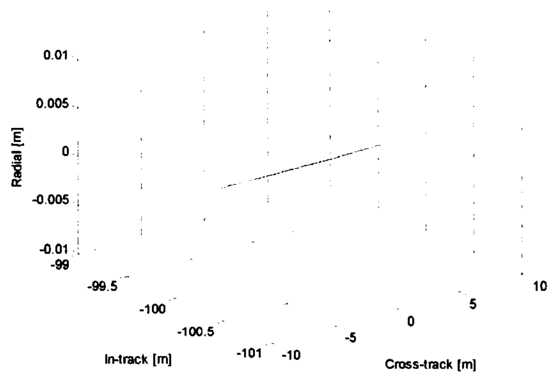

Figure 5.40: TECSAS-TECSAS In-track Formation - Unperturbed.

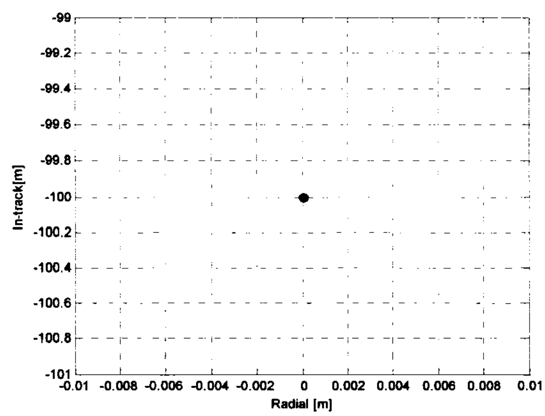

Figure 5.41: TECSAS-TECSAS In-track Formation - Unperturbed - xy Plane Projection.

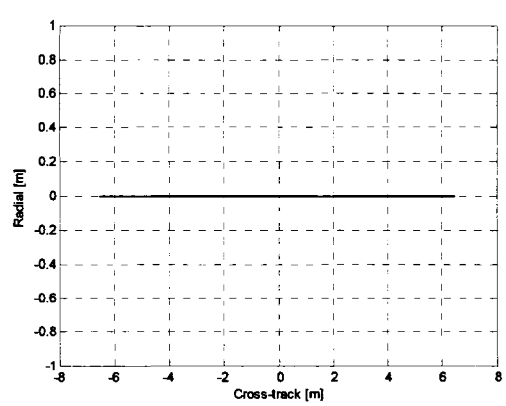

Figure 5.42: TECSAS-TECSAS In-track Formation - Unperturbed - zx Plane Projection.

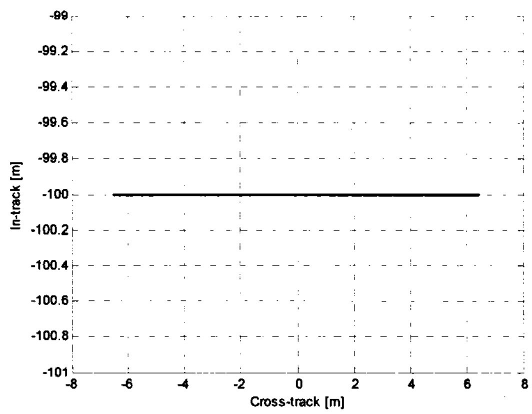

Figure 5.43: TECSAS-TECSAS In-track Formation - Unperturbed - zy Plane Projection.

5.3.2 TECSAS-TECSAS In-track Formation - J_2 and Atmospheric Drag Perturbations

In this subsection, differential atmospheric drag perturbations are studied in order to identify their effects on the TECSAS-TECSAS in-track formation.

By comparing Figures 5.44 to 5.47 with Figures 5.40 to 5.43, it can be seen that there are no significant formation deviations caused by differential atmospheric drag perturbations acting on the deputy with respect to the chief spacecraft after 1 day of simulation. The oscillating motion in the radial direction as seen in Figures 5.44, 5.45, and 5.46 is due to the Earth's oblateness and it is not present in the unperturbed case. However, this radial oscillating motion is at the centimetre level, such that it can be neglected when compared to the cross-track motion.

1-Day Simulation

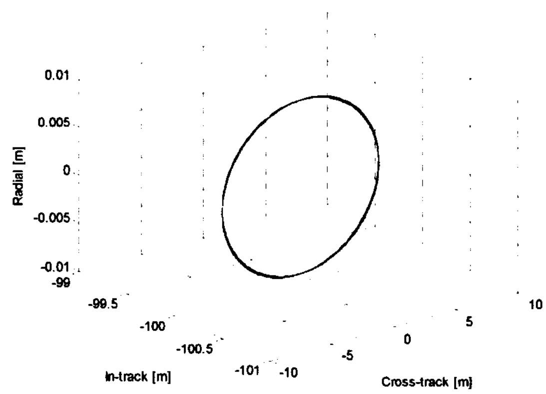

Figure 5.44: TECSAS-TECSAS In-track Formation - J_2 and Atmospheric Drag Perturbations - 1 Day Simulation.

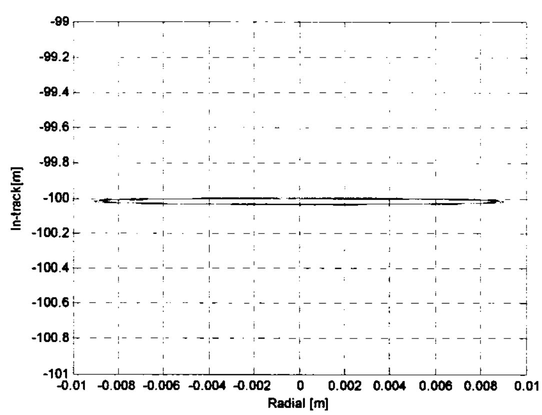

Figure 5.45: TECSAS-TECSAS In-track Formation - J_2 and Atmospheric Drag Perturbations - 1 Day Simulation - xy Plane Projection.

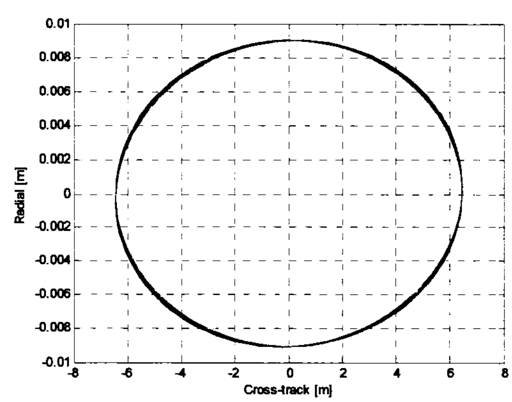

Figure 5.46: TECSAS-TECSAS In-track Formation - J_2 and Atmospheric Drag Perturbations - 1 Day Simulation - zx Plane Projection.

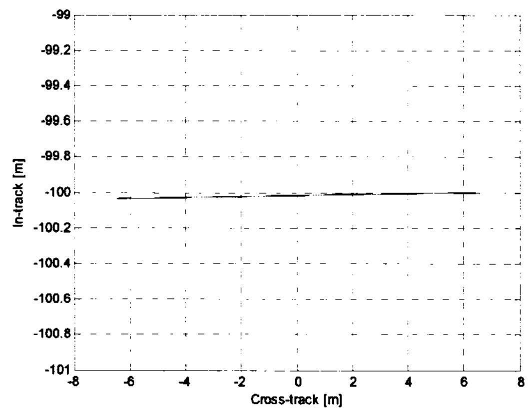

Figure 5.47: TECSAS-TECSAS In-track Formation - J_2 and Drag Atmospheric Perturbations - 1 Day Simulation - zy Plane Projection.

4 Weeks Simulation

After a time span of 4 weeks, differential atmospheric drag perturbations cause an in-track drift of approximately 145 m for the TECSAS-TECSAS in-track formation as can be seen in Figures 5.49 and 5.51. The in-track drift is caused because the two spacecraft occupy slightly different orbital planes. Because of this, the deputy spacecraft "sees" a different atmosphere than the chief spacecraft and in-track drift occurs between both spacecraft. Furthermore, atmospheric perturbations also cause a small radial drift to occur between the two spacecraft as seen in Figure 5.49 and 5.50.

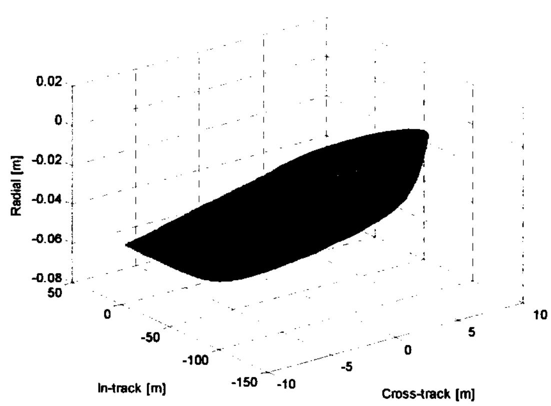

Figure 5.48: TECSAS-TECSAS In-track Formation - J_2 and Atmospheric Drag Perturbations - 4 Weeks Simulation.

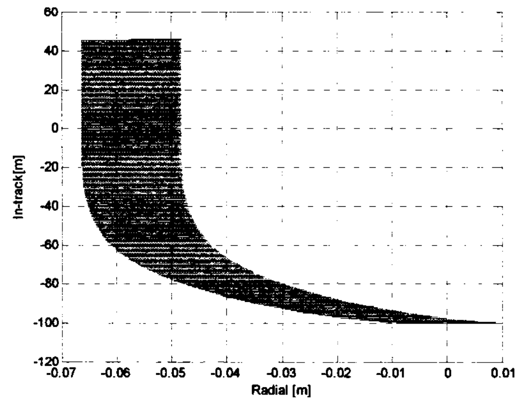

Figure 5.49: TECSAS-TECSAS In-track Formation - J_2 and Atmospheric Drag Perturbations - 4 Weeks Simulation - xy Plane Projection.

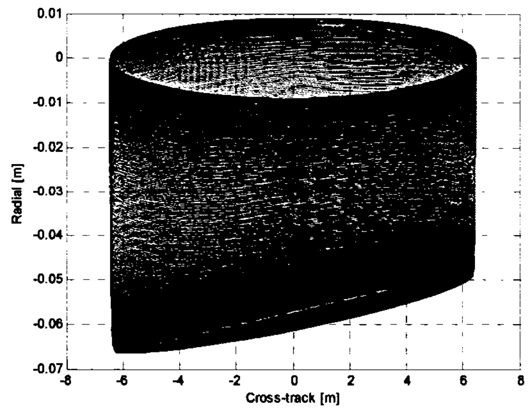

Figure 5.50: TECSAS-TECSAS In-track Formation - J_2 and Atmospheric Drag Perturbations - 4 Weeks Simulation - zx Plane Projection.

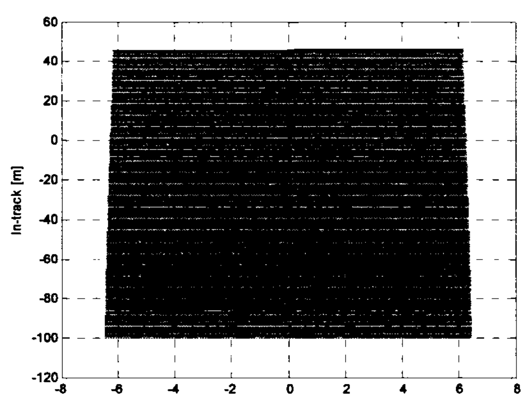

Figure 5.51: TECSAS-TECSAS In-track Formation - J_2 and Atmospheric Drag Perturbations - 4 Weeks Simulation - zy Plane Projection.

Thus, because of differential atmospheric drag perturbations, the TECSAS-TECSAS formation geometry is disrupted and a control system is needed to counteract these orbital perturbations. Results from the implementation of such a control system are presented in the following subsection.

5.3.3 TECSAS-TECSAS In-track Formation - J_2 and Atmospheric Drag Perturbations and Control Inputs

As was done for the projected circular formation, a linear quadratic regulator (LQR) controller is added in order to maintain formation geometry by counteracting the J_2 and atmospheric drag orbital perturbations acting on the TECSAS-TECSAS in-track formation. As was the case for the projected circular formation, the control gain matrix, **K**, is specified as shown by equation (4.62) with the associated control weight being w = 1000. Simulation results for this case are shown in this subsection.

1-Day Simulation

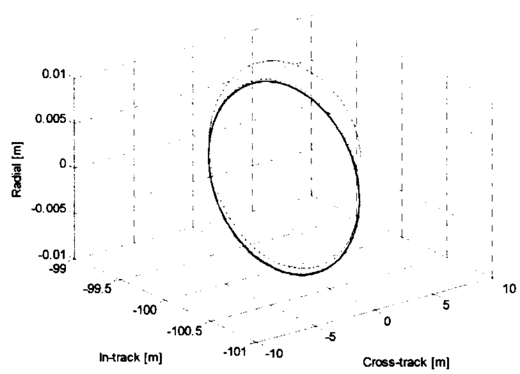

Figure 5.52: TECSAS-TECSAS In-track Formation - J_2 and Atmospheric Drag Perturbations and Control Forces - 1 Day Simulation.

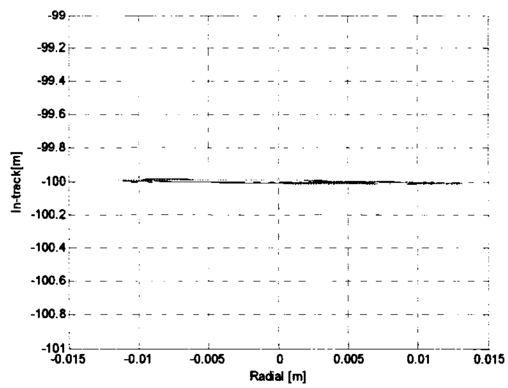

Figure 5.53: TECSAS-TECSAS In-track Formation - J_2 and Atmospheric Drag Perturbations and Control Forces - 1 Day Simulation - xy Plane Projection.

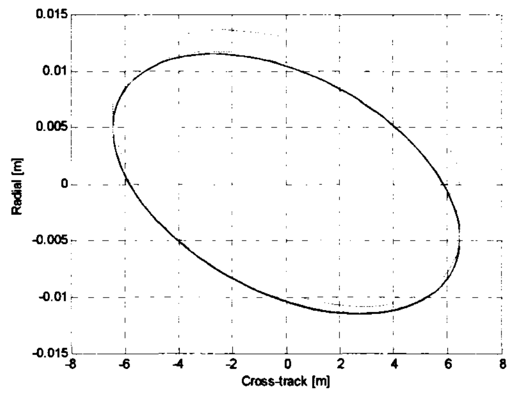

Figure 5.54: TECSAS-TECSAS In-track Formation - J_2 and Atmospheric Drag Perturbations and Control Forces - 1 Day Simulation - zx Plane Projection.

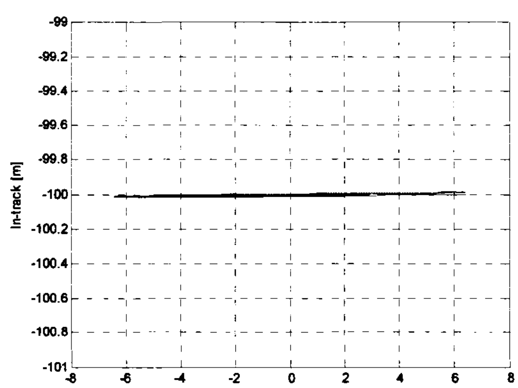

Figure 5.55: TECSAS-TECSAS In-track Formation - J_2 and Atmospheric Drag Perturbations and Control Forces - 1 Day Simulation - zy Plane Projection.

From Figures 5.52 to 5.55 it can be seen that the linear quadratic regulator (LQR) controller successfully maintains the TECSAS-TECSAS in-track formation geometry over a short time span because the resulting relative motion resembles the unperturbed case. However, because of the specified initial conditions, there is an initial radial offset as can be seen in Figures 5.52 and 5.54. Furthermore, comparing Figure 5.54 to Figure 5.46 shows that the motion in the radial/cross-track plane is not the same. With the control system, the motion in the radial/cross-track plane becomes a titled ellipse instead of a circle, as was the case in Figure 5.46. The errors involved are small because they are of centimeter levels and thus, they are not significant to the formation's geometry. Finally, for longer time spans, the linear quadratic regulator controller is able to maintain formation geometry and the results are not shown here for repetitiveness.

The following figures show the variations in the control forces over a number of orbits for both time spans of 1 day and 4 weeks.

1-Day Simulation

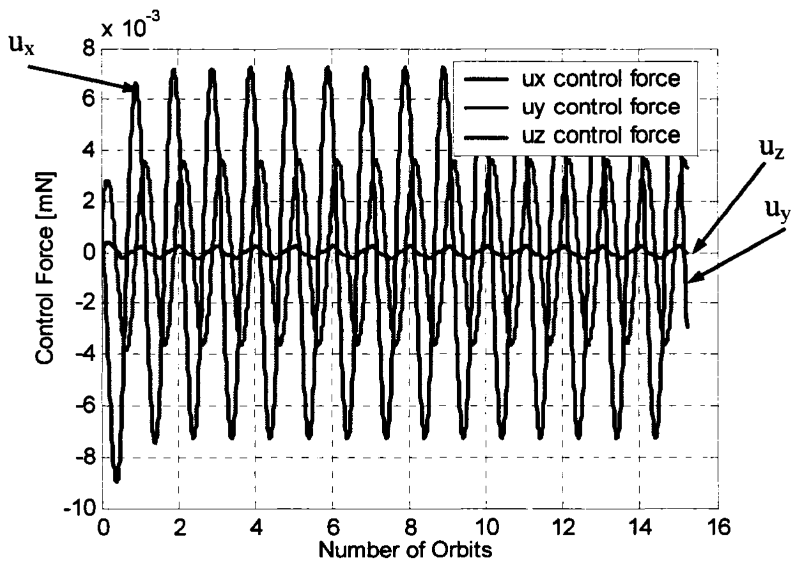

Figure 5.56: TECSAS-TECSAS In-track Formation - J_2 and Atmospheric Drag Perturbations and Control Forces - 1 Day Simulation - Control Forces.

From Figure 5.56, it can be seen that the radial control force (u_x), which oscillates between ±0.007mN, is greater than the other two components. The in-track control force

(u_y) oscillates between ±3.7x10^{-3} mN, while the cross-track control force (u_z) is the least important component, and it oscillates between approximately ±5x10^{-4} mN. After a time span of 4 weeks, all control forces components continue to behave as described above as can be seen in Figure 5.57.

4 Weeks Simulation

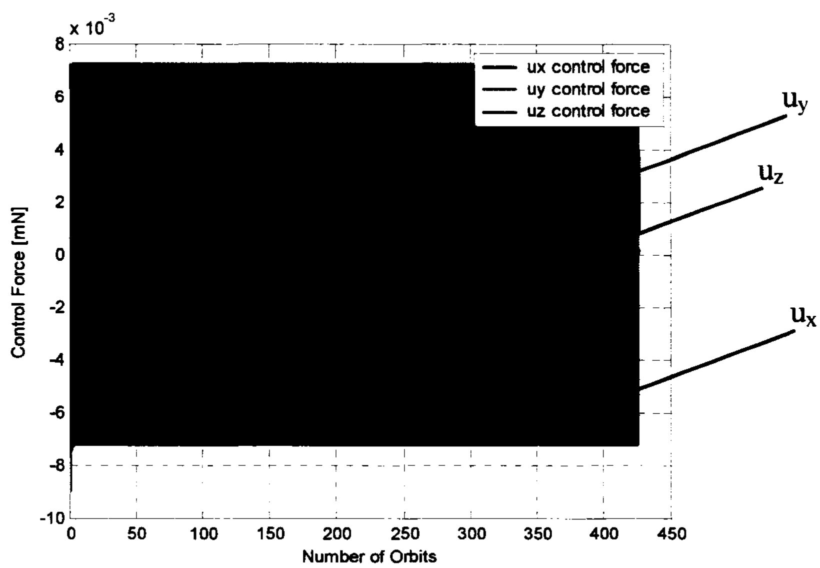

Figure 5.57: TECSAS-TECSAS In-track Formation - J_2 and Atmospheric Drag Perturbations and Control Forces - 4 Weeks Simulation - Control Forces.

The total control impulse requirements for 1 day and 4 weeks and for each individual component are given in Table 5.7. As can be seen from Table 5.7, the total control impulse requirement for a 1-day time span is 0.608 Ns, while the total impulse requirement for the 4-week time span is approximately 17.040 Ns. The relationship between the control impulse requirement and the simulation duration is linear as can be seen from these results.

Furthermore, from Table 5.7, comparing the radial and in-track force components shows that for a time span of 1 day, the radial impulse requirement is 0.398 Ns, while the in-track control requires approximately half of that value at 0.199 Ns. The cross-track control requirement is negligible compared to the other two components.

Table 5.7: LQR Controller Impulse Requirements for 1 Day and 4 Weeks Time Spans for TECSAS-TECSAS In-track Formation Flying Scenario

	1 day	4 weeks
Radial control impulse	0.398 Ns	11.164 Ns
In-track control impulse	0.199 Ns	5.583 Ns
Cross-track control impulse	0.011 Ns	0.293 Ns
Total control impulse	**0.608 Ns**	**17.040 Ns**

In conclusion, the TECSAS-TECSAS in-track formation's geometry becomes unstable when the atmospheric drag perturbations are taken into account and simulation results show that small control forces are required to maintain formation geometry over long time spans. In the next section, simulation results are presented for the Quicksat-TECSAS in-track formation scenario.

5.4 QUICKSAT-TECSAS IN-TRACK FORMATION

In this section, simulation results are given for the Quicksat-TECSAS in-track formation scenario. As was the case for the Quicksat-TECSAS projected circular formation in section 5.2, the chief spacecraft is assumed to be the Canadian Space Agency's (CSA) Quicksat spacecraft and its has the characteristics as given in Table 5.4.

The atmospheric drag perturbations acting on the Quicksat-TECSAS in-track formation are studied in the following subsection, after which, simulation results are presented in the subsequent subsections for the same formation in which a linear quadratic regulator (LQR) controller is added to maintain the formation's geometry.

5.4.1 Quicksat-TECSAS In-track Formation - J_2 and Atmospheric Drag Perturbations

In this subsection, the Quicksat-TECSAS in-track formation is subjected to both J_2 and atmospheric drag perturbations. The goal is to study the differential atmospheric drag perturbations effects on the formation. As was the case for the Quicksat-TECSAS projected circular formation in section 5.3.1, simulations are only carried out for a 1-day time span because significant in-track drift occurs, which breaks up the formation.

1-Day Simulation

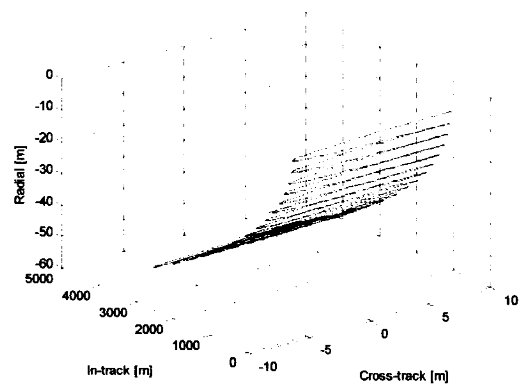

Figure 5.58: Quicksat-TECSAS In-track Formation - J_2 and Atmospheric Drag Perturbations - 1 Day Simulation.

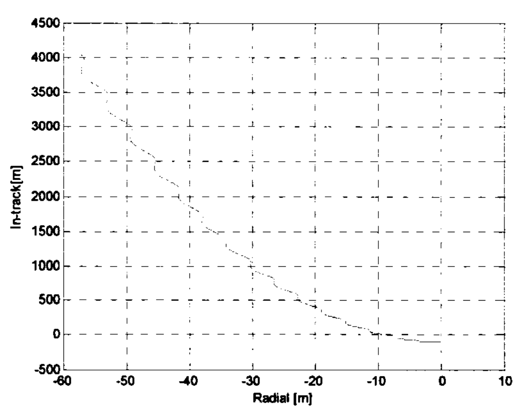

Figure 5.59: Quicksat-TECSAS In-track Formation - J_2 and Atmospheric Drag Perturbations – 1 Day Simulation - xy Plane Projection.

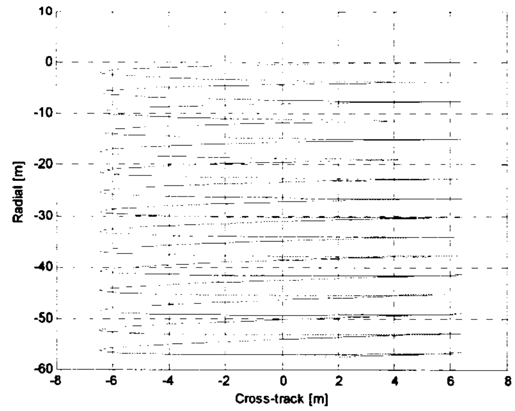

Figure 5.60: Quicksat-TECSAS In-track Formation - J_2 and Atmospheric Drag Perturbations - 1 Day Simulation - zx Plane Projection.

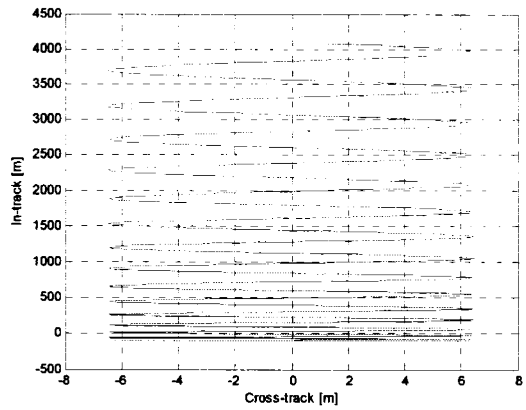

Figure 5.61: Quicksat-TECSAS In-track Formation - J_2 and Atmospheric Drag Perturbations - 1 Day Simulation - zy Plane Projection.

From Figures 5.58 to 5.61, it can be seen that there is significant drift in the in-track and radial directions that results from the differential atmospheric drag perturbations acting on the deputy (TECSAS) with respect to the chief (Quicksat) spacecraft. The in-track drift is approximately 4.1 km, while the radial drift is approximately 55 m. Since the deputy's ballistic coefficient is smaller than the chief's, the atmospheric drag perturbations acting on it are smaller than those acting on the chief. Thus, the deputy's orbit deteriorates at a faster rate than the chief's orbit and as a result of this, radial and in-track separation between both spacecraft occur. In the next subsection, simulation results with regards to the implementation of a linear quadratic regulator (LQR) controller are presented.

5.4.2 Quicksat-TECSAS In-track Formation - J_2 and Atmospheric Drag Perturbations and Control Inputs

As was presented in the previous subsection, orbital drift causes the Quicksat-TECSAS in-track formation geometry to break up, even after a short time span. In order to counteract the differential atmospheric drag perturbations acting on the deputy spacecraft a linear quadratic regulator (LQR) controller is used in order to generate formation keeping control forces. As was the case in section 5.3.3, the control gain matrix, **K**, is specified as shown by equation (4.62) with the associated control weight being $w = 1000$. Simulation results are shown in this subsection.

1-Day Simulation

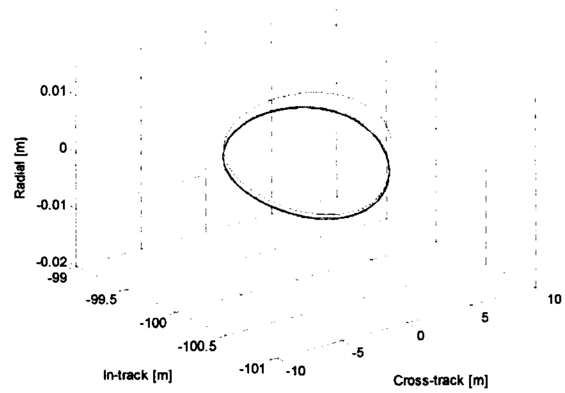

Figure 5.62: Quicksat-TECSAS In-track Formation - J_2 and Atmospheric Drag Perturbations and Control Forces - 1 Day Simulation.

Figure 5.62 shows a three dimensional view of the Quicksat-TECSAS in-track formation after a time span of 1 day. It is clear from it that the formation keeping forces are successful in maintaining the formation geometry. Other figures pertaining both to plane projections of the relative motion and for longer simulation time spans are not presented for repetitiveness.

The following figures represent the formation keeping control forces versus orbit count for a 1-day and 4-week simulation time span.

1-Day Simulation

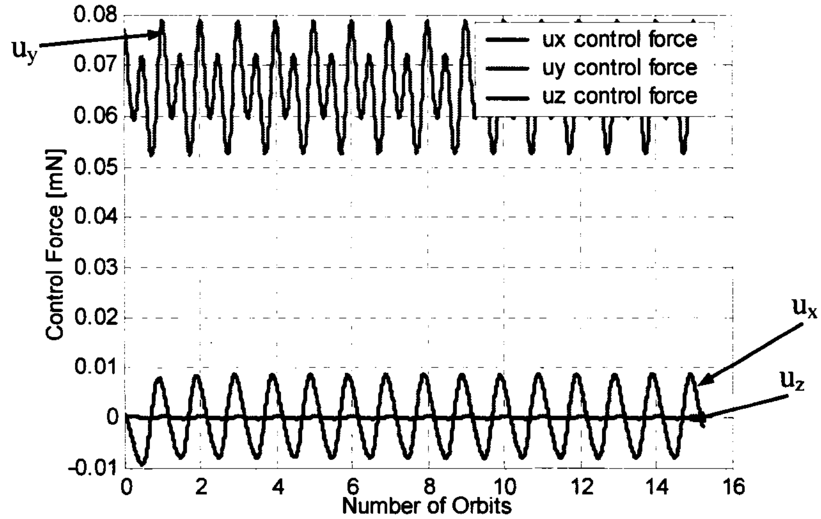

Figure 5.63: Quicksat-TECSAS In-track Formation - J_2 and Atmospheric Drag Perturbations and Control Forces - 1 Day Simulation - Control Forces.

From Figure 5.63, it can be seen that the in-track control force (u_y) oscillates over a mean non-zero fixed value of approximately 0.066 mN. Furthermore, as was the case for the Quicksat-TECSAS projected circular formation, there are two components in the in-track control force oscillations. The radial control force (u_x) oscillates between ±0.008 mN, and its period is a quarter of an orbit later than the in-track component. Finally, the cross-track control force (u_z), the least significant of the three force components, oscillates between $\pm 2.5 \times 10^{-4}$ mN. The next figure shows the behavior of the formation keeping control forces over a period of 4 weeks.

4 Weeks Simulation

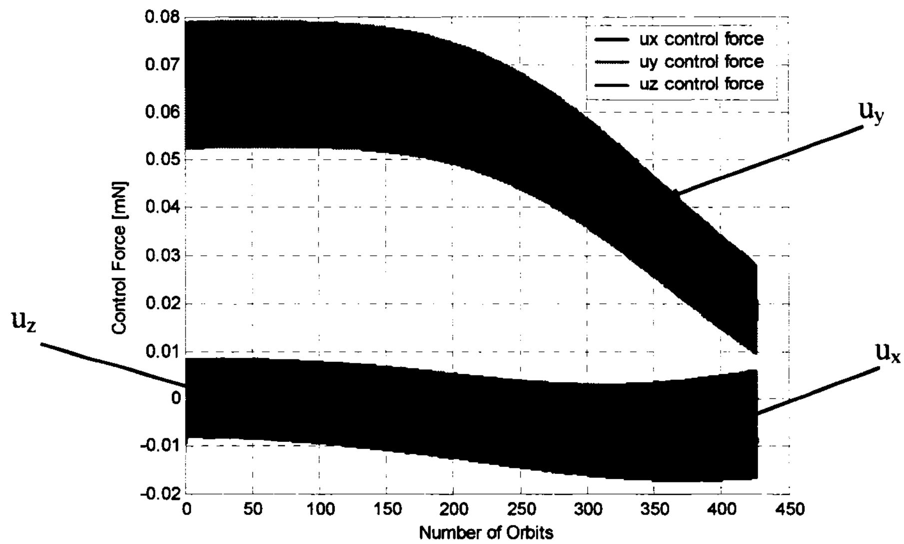

Figure 5.64: Quicksat-TECSAS In-track Formation - J_2 and Atmospheric Drag Perturbations and Control Forces - 4 Weeks Simulation - Control Forces.

From Figure 5.64, it can be seen that both the radial and cross-track control forces, (u_x) and (u_z), continue to behave as described previously. However, the in-track control force (u_y) decreases as time progresses as was the case in the Quicksat-TECSAS projected circular formation. The next figure, Figure 5.65, shows that the decrease in in-track control force stops when it begins oscillating around the zero value after around the 700th orbit.

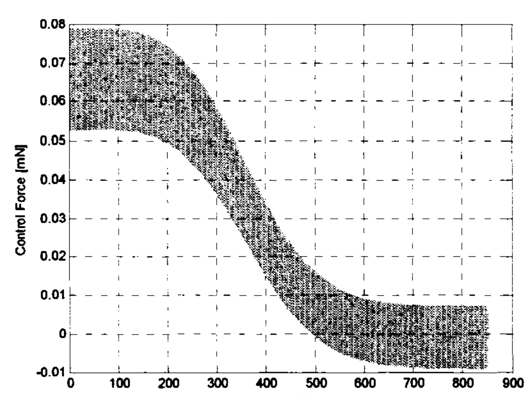

Figure 5.65: Quicksat-TECSAS In-track Formation - J_2 and Atmospheric Drag Perturbations and Control Forces - 4 Weeks Simulation - In-track Control Forces.

The following table, Table 5.8, gives the linear quadratic regulator control impulse requirements for both time spans of 1 day and 4 weeks.

Table 5.8: LQR Controller Impulse Requirements for 1 Day and 4 Weeks Time Spans for TECSAS-TECSAS In-track Formation Flying Scenario

	1 day	4 weeks
Radial control impulse	0.446 Ns	16.592 Ns
In-track control impulse	5.657 Ns	128.683 Ns
Cross-track control impulse	0.011 Ns	0.294 Ns
Total control impulse	**6.114 Ns**	**145.569 Ns**

From Table 5.8, it can be seen that the total control impulse requirement for 1-day is 6.114 Ns, while the total control impulse requirement for 4 weeks is 145.569 Ns. Comparing these values with those from the TECSAS-TECSAS in-track formation scenario (from Table 5.7) shows that the Quicksat-TECSAS scenario requires approximately 10 times more control impulse. In addition, in comparison with the TECSAS-TECSAS scenario, the increase in control impulse comes from the in-track component because the other two control input components share similar values for the 1-day case, and only the radial control input component shows a significant increase in the 4 weeks case.

Like the other Quicksat-TECSAS formation flying scenario, the in-track direction requires more control impulse because of differential atmospheric drag perturbations acting on the deputy (TECSAS) with respect to the chief (Quicksat). For the Quicksat-TECSAS in-track formation, in-track corrections require 5.657 Ns of control impulse over 1-day, and they require 128.683 Ns over 4 weeks. Over a time span of 1 day, radial corrections require 0.446 Ns of control impulse and they require 16.592 Ns over 4 weeks. The cross-track control impulse requirements are negligible compared to the other two. Finally, as was shown in this subsection, the linear quadratic regulator (LQR) controller is able to maintain formation geometry for the Quicksat-TECSAS in-track formation for short and possibly long time spans.

CHAPTER 6 - CONCLUSION

6.1 SUMMARY OF THE THESIS

In this thesis, spacecraft rendezvous and spacecraft formation flying were examined in context of the TECSAS mission. In the first chapter, a literature review regarding the dynamics associated with spacecraft rendezvous and formation flying was presented along with details related to the TECSAS mission.

The equations of motion used for spacecraft rendezvous analyses were presented in the second chapter. The equations of motion used were the general form of C-W equations, which are valid for eccentric orbits; thus the eccentricity of the TECSAS orbit was taken into account in this study. Also, in comparison with past work, the addition of J_2 and atmospheric drag perturbations to the C-W equations of motion and the use of a perturbed elliptical orbit instead of an unperturbed circular reference orbit represent new work in this field, which permits more precise simulations to be made. The last section of the second chapter dealt with rendezvous manoeuvres where a perturbation method was used in creating the MATLAB/SIMULINK-based autonomous spacecraft simulator. This method is a new approach that lends itself to using simple orbital manoeuvres designed to be used when orbital perturbations are not taken into account to the case where these perturbations are included in the simulations.

Simulation results for three terminal rendezvous trajectories were studied in chapter three. Results showed that the lidar-based V-bar approach trajectory with a 90 m straight-line approach distance is the optimal scenario given the TECSAS mission guidelines. The lidar-based V-bar approach trajectory is less complex than the R-bar approach trajectory with V-bar station keeping and it requires 35 % less ΔV than the latter. Even though the lidar-based V-bar approach trajectory requires 20% more time of flight (TOF) than the R-bar approach trajectory with V-bar station keeping, the savings in time of flight (TOF) are not substantial as an operational constraint compared to the savings in fuel usage. Finally, the other terminal rendezvous trajectory examined in this thesis, the drift orbit and R-bar approach trajectory, is the least desirable choice among the three types of trajectories, because of its excessive overall fuel usage compared to the other two trajectories.

In chapter four, the equations of motion for use in describing spacecraft formation flying were presented. The equations used in this thesis were based on those developed by Schweighart and Sedwick (2002) and they take into account the J_2 perturbations acting on the spacecraft in the formation. Atmospheric drag perturbations were added to these equations of motion in order to better determine the relative motion between the two spacecraft involved. The addition of atmospheric drag perturbations to the specific dynamic model is new when considering the specific models used in this study. In the last section of chapter four, a linear quadratic regulator (LQR) controller, modified from the one described by Vaddi and Vadali (2003), was implemented in order to maintain the spacecraft formation flying geometry. The addition of this particular LQR controller that takes into account the differential atmospheric drag perturbations represents new work in this field.

In chapter five, simulation results for several formation flying scenarios were presented. Four formation flying scenarios were examined: the TECSAS-TECSAS projected circular formation, the Quicksat-TECSAS projected circular formation, the TECSAS-TECSAS in-track formation and the Quicksat-TECSAS in-track formation. The effects of the J_2 and atmospheric drag perturbations on these formations were studied for several time spans. Also, simulation results in which a linear quadratic regulator controller was used in order to maintain formation geometry were presented.

Simulation results from chapter five showed that over the course of a day, the J_2 perturbations cause the projected circular formation geometry to disperse, such that mission constraints are no longer valid. In the case of the in-track formation, simulation results show that this formation is stable under the J_2 perturbations even over the course of a month. Furthermore, results for the projected circular and in-track formations showed that atmospheric drag perturbations are negligible over a short time span when both spacecraft are identical. However, significant relative drift can occur in the in-track and radial directions after one day if both spacecraft are not identical. In the case of the Quicksat-TECSAS formations, the in-track drifts were of approximately 4 km for both the projected circular and in-track formations, while the radial drifts were approximately 50 m for these same formations. Regarding the performance of the linear quadratic regulator (LQR) controller, simulation results showed that it was successful in maintaining formation geometry for all four scenarios for both short time spans and longer ones. Finally, as was shown in the formation flying analyses, using similar sized spacecraft has advantages when considering formation flying because the control force requirements are much higher for both the projected circular and in-track formation when the two spacecraft are not identical than when they are of similar sized.

6.2 RECOMMENDATIONS FOR FUTURE WORK

As an extension of the work done in this thesis, more terminal rendezvous trajectories including out-of-plane trajectories, should be studied in order to determine a truly optimal scenario in terms of mission constraints. In addition, the other rendezvous phases of the TECSAS mission, both orbit phasing and far range operations, should be simulated and optimized in terms of ΔV fuel usage or other mission-related constraints.

In the area of formation flying, more precise simulations are needed to effectively evaluate the relative motion between the two spacecraft. Solar radiation pressure and third body perturbations need to be taken into account in the formation flying model. Also, mission constraints for each formation studied should be chosen with respect to a particular application instead of choosing them arbitrarily.

Finally, the linear quadratic regulator (LQR) controller used in the formation flying analyses needs to be improved for the mission scenarios studied here, because it was only slightly modified from previous work without optimizing it; this should be done.

APPENDIX A - EXPONENTIAL ATMOSPHERIC MODEL

In this appendix, table A-1 shows parameter values associated with the exponential atmospheric model described in section 2.1.1. Table A-1 is taken from Vallado (2002).

Table A-1: Exponential Atmospheric Model [Vallado, 2002]

Altitude h_{ellp} (km)	Base Altitude h_0 (km)	Nominal Density ρ_0 (kg/m^3)	Scale Height H (km)	Altitude h_{ellp} (km)	Base Altitude h_0 (km)	Nominal Density ρ_0 (kg/m^3)	Scale Height H (km)
0-25	0	1.225	7.249	150-180	150	2.070×10^{-9}	22.523
25-30	25	3.899×10^{-2}	6.349	180-200	180	5.464×10^{-10}	29.740
30-40	30	1.774×10^{-2}	6.682	200-250	200	2.789×10^{-10}	37.105
40-50	40	3.972×10^{-3}	7.554	250-300	250	7.248×10^{-11}	45.546
50-60	50	1.057×10^{3}	8.382	300-350	300	2.418×10^{-11}	53.628
60-70	60	3.206×10^{-4}	7.714	350-400	350	9.158×10^{-12}	53.298
70-80	70	8.770×10^{-5}	6.549	400-450	400	3.725×10^{-12}	58.515
80-90	80	1.905×10^{-5}	5.799	450-500	450	1.585×10^{-12}	60.828
90-100	90	3.396×10^{-6}	5.382	500-600	500	6.967×10^{-13}	63.822
100-110	100	5.297×10^{-7}	5.877	600-700	600	1.454×10^{-13}	71.835
110-120	110	9.661×10^{-8}	7.263	700-800	700	3.614×10^{-14}	88.667
120-130	120	2.438×10^{-8}	9.473	800-900	800	1.170×10^{-14}	124.64
130-140	130	8.484×10^{-9}	12.636	900-1000	900	5.245×10^{-15}	181.05
140-150	140	3.845×10^{-9}	16.149	1000+	1000	3.019×10^{-15}	268.00

APPENDIX B - HEIGHT ABOVE ELLIPSOID

In order to accurately model the atmospheric drag perturbations acting on a spacecraft, an ellipsoid model is used instead of a sphere to represent the Earth. In this appendix, an algorithm to determine the spacecraft's height above the ellipsoid is presented, which is used in conjunction with the exponential atmospheric model described in section 2.1.1. The algorithm is taken from Vallado (2002). Finally, it is noted that in the following equations all the variables are normalized with respect to the Earth radius.

The following figure shows a schematic representation of the height above ellipsoid.

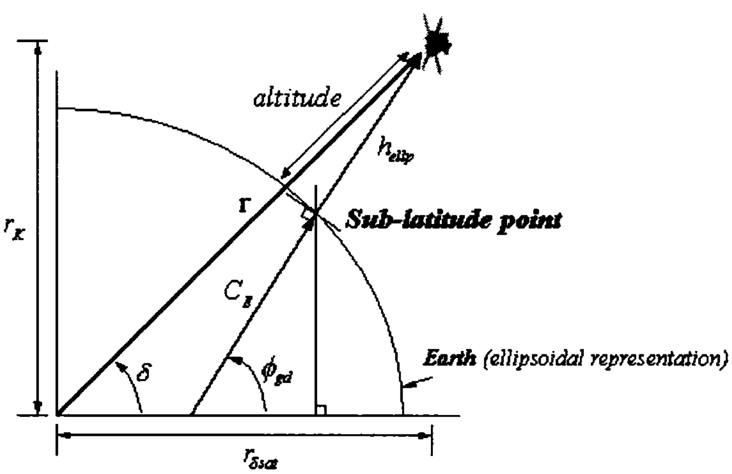

Figure B.1: Determining a Spacecraft's Height Above the Ellipsoid.

First the equatorial projection of the spacecraft's position vector is defined by

$$r_{\delta sat} = \sqrt{r_I^2 + r_J^2} \tag{B.1}$$

where r_I, r_J, and r_K are the coordinates of the spacecraft given in the Earth-Centered Inertial (ECI) reference frame.

Let the geodetic latitude, ϕ_{gd}, be

$$\phi_{gd} = \delta \tag{B.2}$$

Then, it can be determined from the following equation:

$$\tan(\delta) = \frac{r_K}{r_{\delta sat}} \tag{B.3}$$

The height above ellipsoid is determined by

$$h_{ellp} = \frac{r_{\delta sat}}{\cos(\phi_{gd})} - C_E \tag{B.4}$$

where C_E is the distance of the surface of the Earth from its centre at that geodetic latitude.

C_E and ϕ_{gd} can be calculated by iterating the next two equations

$$C_E = \frac{R_E}{\sqrt{1 - e_E^2 \sin^2(\phi_{gd})}} \tag{B.5}$$

$$\tan(\phi_{gd}) = \frac{r_K + C_E e_E^2 \sin(\phi_{gd})}{r_{\delta sat}} \tag{B.6}$$

where e_E is the eccentricity of the Earth.

The iterations are continued until

$$\phi_{gd_{new}} - \phi_{gd_{old}} < Tolerance \tag{B.7}$$

Since the equations of motion used for both the rendezvous and formation flying analyses determine the spacecraft's position in Hill frame coordinates, its position in the Earth-Centered Inertial (ECI) reference frame, $\mathbf{r}_{spacecraft}$, must be calculated in order to use the equations in this algorithm.

The spacecraft's ECI position is thus defined by

$$\mathbf{r}_{spacecraft} = \mathbf{r}_{ref} + \mathbf{R}_t \mathbf{r}_{rel} \tag{B.8}$$

where $\mathbf{r}_{ref}$ and $\mathbf{r}_{rel}$ are the position of the reference orbit in the Earth-Centered Inertial (ECI) reference frame and the position of the spacecraft in the Hill frame respectively. These are given by equations (2.1) and (2.2) respectively for the rendezvous formulation and by equations (4.21) and (4.1) respectively for the formation flying formulation.

$\mathbf{R}_t$ is the rotation matrix given by

$$\mathbf{R}_t = \begin{bmatrix} \cos\Omega\cos\omega - \sin\Omega\sin\omega\cos i & -\cos\Omega\sin\omega - \sin\Omega\cos\omega\cos i & \sin\Omega\sin i \\ \sin\Omega\cos\omega + \cos\Omega\sin\omega\cos i & -\sin\Omega\sin\omega + \cos\Omega\cos\omega\cos i & -\cos\Omega\sin i \\ \sin\omega\sin i & \cos\omega\sin i & \cos i \end{bmatrix} \tag{B.9}$$

The rotation matrix uses the reference orbit's inclination, i, its argument of perigee, ω, (in the case of the formation flying formulation, the argument of latitude, θ, is used instead of the argument of perigee) and longitude of the ascending node, Ω, in order to transform the spacecraft's Hill coordinates into Earth-Centered Inertial (ECI) coordinates. These orbital elements were further discussed in section 2.1.2 for the rendezvous formulation and in section 4.1.2 for the formation flying formulation.

REFERENCES

Alfriend, K. T., Schaub, H., and, Gim, D.-W., "Gravitational Perturbations, Nonlinearity and Circular Orbit Assumption Effects on Formation Flying Control Strategies," AAS Paper 00-012, 23rd *Annual AAS Rocky Mountain Conference*, Breckenridge, CO, February 2-6, 2000.

Alfriend, K. T., Vaddi, S. S., and Lovell, T. A., "Formation Maintenance for Low Earth Near-Circular Orbits," AAS Paper 03-652, *AAS/AIAA Astrodynamics Specialist Conference*, Big Sky, Montana, August 3-7, 2003.

Balaji, S. K., and Tatnall, A., "Precise Modeling of Spacecraft Relative Motion For Formation Flying," Paper IAC-03-A.P.15, *54th International Astronautical Congress*, Bremen, Germany, September 29 - October 3, 2003.

Broucke, R. A., "Solution of the Elliptic Rendezvous Problem with Time as Independent Variable," *Journal of Guidance, Control, and Dynamics*, Vol. 26, No. 4, July-August 2003, pp. 615-621.

Caramagno, A., Benavente, D., Bastante, J. C., Fernàndez, V., Peñin, L. F., and Rodriguez-Canabal, J., "G&C Design Process For Future Formation Flying and Automated Rendezvous Missions," Paper IAC-03-A.2.04, *54th International Astronautical Congress*, Bremen, Germany, September 29 - October 3, 2003.

Carter, T. E., "State Transition Matrices for Terminal Rendezvous Studies: Brief Survey and New Example," *Journal of Guidance, Control, and Dynamics*, Vol. 21, No. 1, 1998, pp.148-155.

Chobotov, V. A., "*Orbital Mechanics, Third Edition,*" AIAA Education Series, Reston, Virginia, 2002, 460 p.

Cislaghi, M., Fehse, W., Paris, D., and Ankersen, F., "The ATV Rendez-vous Predevelopment Programme (ARP)," AAS Paper 99-024, 22nd *Annual AAS Rocky Mountain Conference*, Breckenridge, CO, February 3-7, 1999.

Clohessy, W. H., and Wiltshire, R. S., "Terminal Guidance System for Satellite Rendezvous, " *Journal of the Aerospace Sciences*, Vol. 27, No. 9, 1960, pp. 653-674.

D'Amario, L. A., Bollman, W. E., Lee, W. J., Roncoli, R. B., Smith, J. C., Bhat, R. S., and Frauenholtz, R. B., "Mars Orbit Rendezvous Strategy for the Mars 2003/2005 Sample Return Mission," AAS Paper 99-306, *AAS/AIAA Astrodynamics Conference*, Girdwood, Alaska, August 16-19, 1999.

D'Souza, C., Bogner, A., Brand, T., Tsukui, J., Koyama, H., and Nakamura, T., "An Evaluation of the GPS Relative Navigation System for the ETS-VII and HTV," AAS Paper 99-023, 22nd *Annual AAS Rocky Mountain Conference*, Breckenridge, CO, February 3-7, 1999.

Duan, X., and Bainum, P. M., "Design of Spacecraft Formation Flying Orbits," AAS Paper 03-588, *AAS/AIAA Astrodynamics Specialist Conference*, Big Sky, Montana, August 3-7, 2003.

Duan, X., and Bainum, P.M., "Low-Thrust Autonomous Control for Maintaining Formation and Constellation Orbits," AIAA Paper 2004-4978, *AIAA/AAS Astrodynamics Specialist Conference*, Providence, Rhode Island, August 16-19, 2004.

Dupuis, E., Doyon, M., Martin, E., L'Archevêque, R., Allard, P., Piedboeuf, J.-C., and Ma, O., "Autonomous Operations for Space Robots," Paper IAC-04-IAA.U.5.03, *55th International Astronautical Congress*, Vancouver, Canada, October 4-8, 2004.

Endemaño, G. B., Zotes, F. A., Graziano, M., and Ortega, G., "LAREDO (SIMTOOL): Launching, Rendezvous and DOcking (Simulation Tool)," *Proceedings of the 4th*

International Workshop on Satellite Constellations and Formation Flying, São José dos Campos, Brazil, February 14-16, 2005, pp. 158-171.

ESA Science & Technology: DARWIN Website, http://sci.esa.int/science-e/www/area/index.cfm?fareaid=28 (Current April 2005).

Fehse, W., "*Automated Rendezvous and Docking of Spacecraft*," Cambridge University Press, Cambridge, 2003.

Fourcade, J., "Use of Differential Drag as Stationkeeping Strategy for Formation Flying," *Proceedings of the 4th International Workshop on Satellite Constellations and Formation Flying*, São José dos Campos, Brazil, February 14-16, 2005, pp. 206-213.

Garcìa, L., and Masdemont, J. J., "Optimal Reconfiguration of Spacecraft Formations Using Variation Numerical Methods," *Proceedings of the 4th International Workshop on Satellite Constellations and Formation Flying*, São José dos Campos, Brazil, February 14-16, 2005, pp. 52-61.

Gill, E., and Runge, H., "A Tight Formation for Along-track SAR Interferometry," *2nd International Symposium on Formation Flying Missions & Technologies*, Crystal City, VA, September 14-16, 2004.

Gim, D.-W., and Alfriend, K. T., "State Transition Matrix of Relative Motion for the Perturbed Noncircular Reference Orbit," *Journal of Guidance, Control, and Dynamics*, Vol. 26, No. 6, 2003, pp. 956-971.

Guibout, V. M., and Scheeres, D. J., "Spacecraft Formation Dynamics and Design," AIAA Paper 2004-4736, *AIAA/AAS Astrodynamics Specialist Conference*, Providence, Rhode Island, August 16-19, 2004.

Hadaegh, F. Y., Ahmed, A., and Shields, J., "Precision Guidance and Control for Formation Flying Spacecraft," *International Symposium Formation Flying Missions & Technologies*, Toulouse, France, October 29-31, 2002.

Hill, G. W., "Researches in the Lunar Theory, " *American Journal of Mathematics*, Vol. 1, No. 1, 1878, pp.5-26.

Kachmar, P. S., D' Souza, C. N., and Brand, T. J., "Terminal Rendezvous Analysis and Design for the Mars 2003/2005 Sample Return Mission," AAS Paper 99-307, *AAS/AIAA Astrodynamics Conference*, Girdwood, Alaska, August 16-19, 1999.

Kechichian, J. A., "Motion in General Elliptic Orbit with Respect to a Dragging and Precessing Coordinate Frame," *The Journal of the Astronautical Sciences*, Vol. 46, No. 1, 1998, pp. 25-45.

Kechichian, J. A., "The Algorithm of the Two-Impulse Time-Fixed Noncoplanar Rendezvous with Drag and Oblateness Effects," *The Journal of the Astronautical Sciences*, Vol. 46, No. 1, 1998, pp. 47-64.

Koon, W. S., Marsden, J. E., and Murray, R. M., and Masdemont, J., "J_2 Dynamics and Formation Flight," AIAA Paper 2001-4090, *AIAA Guidance, Navigation, and Control Conference and Exhibit*, Montréal, Canada, August 6-9, 2001.

Lee, W. J., D'Amario, L. A., Roncoli, R. B., and Smith, J. C., "Mission Design Overview for the Mars 2003/2005 Sample Return Mission," AAS Paper 99-305, *AAS/AIAA Astrodynamics Conference*, Girdwood, Alaska, August 16-19, 1999.

Lovell, T. A., and Tragesser, S. G., "Guidance for Relative Motion of Low Earth Orbit Spacecraft Based on Relative Orbit Element," AIAA Paper 2004-4988, *AIAA/AAS Astrodynamics Specialist Conference*, Providence, Rhode Island, August 16-19, 2004.

Lovell, T. A., Horneman, K. R., Tragesser, S. G., and Tollefson, M. V., "A Guidance Algorithm For Reconfiguration and Maintenance Based on the Perturbed Clohessy-Wiltshire Equations," AAS Paper 03-649, *AAS/AIAA Astrodynamics Specialist Conference*, Big Sky, Montana, August 3-7, 2003.

Melton, R. G., "Time-Explicit Representation of Relative Motion Between Elliptical Orbits," *Journal of Guidance, Control, and Dynamics*, Vol. 23, No. 4, July-August 2000, p. 604-610.

Meyssignac, B., and Fourcade, J., "Analytical Expression of the Relative Orbit Geometry Through Differential Orbit Elements," *Proceedings of the 4th International Workshop on Satellite Constellations and Formation Flying*, São José dos Campos, Brazil, February 14-16, 2005, pp. 3-10.

Mishne, D. "Formation Control of LEO Satellites Subject to Drag Variations and J_2 Perturbations," AIAA Paper 2002-4430, *AIAA/AAS Astrodynamics Specialist Conference and Exhibit*, Monterey, California, August 5-8, 2002.

Mokuno, M., Kawano, I., and Kasai, T., "Experimental Results of Autonomous Rendezvous Docking on Japanese ETS-VII Satellite," Paper AAS 99-022, 22nd *Annual AAS Rocky Mountain Conference*, Breckenridge, CO, February 3-7, 1999.

NASA – DART Mission: Demonstration of Autonomous Rendezvous Technology Website, http://www.nasa.gov/mission_pages/dart/main/index.html (Current April 2005).

On-Orbit Servicing Website, http://www.on-orbit-servicing.com (Current April 2005).

Pelletier, F. J., Golla, D. F., Allen, A. C. M., "Lidar-based Rendezvous Navigation for MSR," AIAA Paper 2004-4987, *AIAA/AAS Astrodynamics Specialist Conference*, Providence, Rhode Island, August 16-19, 2004.

Roe, F. D., and Howard, R. T., "The Successful Development of an Automated Rendezvous and Capture (AR&C) System for the National Aeronautics and Space Administration," *Proceedings of Space Technology and Applications International Forum – STAIF 2003*, Albuquerque, NM, February 2-5, 2003, p.313-319.

Sabatini, M., Bevilacqua, R., Pantaleoni, M., and Izzo, D., "A Search for Invariant Relative Satellite Motion," *Proccedings of the 4th International Workshop on Satellite Constellations and Formation Flying*, São José dos Campos, Brazil, February 14-16, 2005, pp. 222-229.

Sabol, C., Burns, R., and McLaughlin, C., "Satellite Formation Flying Design and Evolution," *Journal of Spacecraft and Rockets*, Vol. 38, No. 2, 2001, pp. 270-278.

Scharf, D. P., Hadaegh, F. Y., and Kang, B. H., "A Survey of Spacecraft Formation Flying Guidance," *International Symposium Formation Flying Missions & Technologies*, Toulouse, France, 29-31 October, 2002.

Schaub, H. "Spacecraft Relative Orbit Geometry Description Through Orbit Element Differences," *14th U.S. National Congress of Theoretical and Applied Mechanics*, Blacksburg, VA, June 23-28, 2002.

Schaub, H., "Incorporating Secular Drifts Into the Orbit Element Difference Description of Relative Orbits," AAS Paper 03-115, *AAS/AIAA Space Flight Mechanics Meeting*, Ponce, Puerto Rico, February 9-13, 2003.

Schaub, H., and Alfriend, K. T., "Hybrid Cartesian and Orbital Element Feedback Law for Formation Flying Spacecraft," *Journal of Guidance, Control, and Dynamics*, Vol. 25, No. 2, March-April 2002, pp. 387-393.

Schaub, H., and Alfriend, K. T., "J_2 Invariant Reference Orbits for Spacecraft Formations," *Celestial Mechanics and Dynamical Astronomy*, Vol. 79, 2001, pp. 77-95.

Schaub, H. and Junkins, J. L., "*Analytical Mechanics of Space Systems*," AIAA Education Series, Reston, Virginia, 2003, 716 p.

Schaub, H., Vadali, S. R., Junkins, J. L., and Alfriend, K. T., "Spacecraft Formation Control using Mean Orbits Elements," *Journal of the Astronautical Sciences*, Vol. 48, No. 1, January-March 2000, pp. 69-87.

Schweighart, S. A., and Sedwick, R. J., "High-Fidelity Linearized J2 Model for Satellite Formation Flying," *Journal of Guidance, Control, and Dynamics*, Vol. 25, No. 6, 2002, pp. 1073-1080.

Sedwick, R. J., Miller, D. W., and Kong, E. M. C., "Mitigation of Differential Perturbations in Clusters of Formation Flying Satellites," AAS Paper 99-124, *AAS/AIAA Space Flight Mechanics Meeting*, Breckenridge, Colorado, February 7-10, 1999.

Settelmeyer, E., Lehrl, E., Oesterlin, W., Hartmann, R., and Landzettel, K., "The Experimental Servicing Satellite-ESS," Paper 98-c-14, *21st International Symposium on Space Technology and Science*, Omiva, Japan, May 24-31, 1998.

Sparks, A., "Linear Control of Satellite Formation Flying," AIAA Paper 2000-4438, *AIAA Guidance, Navigation, and Control Conference*, Denver, Colorado, August 14-17, 2000.

Starin, S. R., Yedavalli, R. K., and Sparks, A. G., "Spacecraft Formation Flying Maneuvers Using Linear-Quadratic Regulation With No Radial Axis Input," AIAA Paper 2001-4029, *AIAA Guidance, Navigation, and Control Conference and Exhibit*, Montreal, Canada, August 6-9, 2001.

Tillerson, M., and How, J. P., "Formation Flying Control in Eccentric Orbit," AIAA Paper 2001-4092, *AIAA Guidance, Navigation, and Control Conference*, Montréal, Canada, August 6-9, 2001.

Ulybyshev, Y., "Long-Term Formation Keeping of Satellite Constellation Using Linear-Quadratic Controller," *Journal of Guidance, Control, and Dynamics*, Vol. 21, No. 1, January-February 1998, pp. 109-115.

Vadali, S. R., Alfriend, K. T., and Vaddi, S., "Hill's Equations, Mean Orbital Elements, and Formation Flying of Satellites," AAS Paper 00-258, R*ichard H. Battin Astrodynamics Symposium*, March 2000.

Vadali, S. R., Schaub, H., and Alfriend, K. T., "Initial Conditions and Fuel-Optimal Control For Formation Flying of Satellites," AIAA Paper 99-4265, *AIAA Modeling and Simulation Technologies Conference*, Portland, Oregon, August 9-11, 1999.

Vaddi, S. S., and Vadali, S. R., "Linear and Nonlinear Control Laws for Formation Flying," AAS Paper 03-109, *Advances in the Astronautical Sciences,* Vol. 114, no. Part I: Spaceflight Mechanics 2003, pp. 171-187.

Vaddi, S. S., Vadali, S. R., and Alfriend, K. T., "Formation Flying: Accommodating Nonlinearity and Eccentricity Perturbations," *Journal of Guidance, Control, and Dynamics*, Vol. 26, No. 2, March-April 2003, p. 214-223.

Vallado, D. A., "*Fundamentals of Astrodynamics and Applications, Second Edition*," Space Technology Library, Kluwer Academic Publishers, Boston, 2001, 958 p.

Wiesel, W. E., "Relative Satellite Motion About An Oblate Planet," *Journal of Guidance, Control, and Dynamics*, Vol. 25, No. 4, July-August 2002, pp. 776-785.

Yamanka, K., and Ankersen, F., "New State Transition Matrix for Relative Motion on a Arbitrary Elliptical Orbit," *Journal of Guidance, Control, and Dynamics*, Vol. 25, No. 1, 2002, pp.60-66.